Magnetic properties of iron oxide and iron oxide in graphitic matrix

Thesis submitted to

Cochin University of Science and Technology

in partial fulfilment of the requirements

for the award of the degree of

Doctor of Philosophy

In

Physics

By

Satheesh M.

Nano Functional Materilas Lab
Department of Physics
Cochin University of Science and Technology
Kochi- 682 022, Kerala, India

August 2018

Magnetic properties of iron oxide and iron oxide in graphitic matrix

Ph.D. thesis in the field of Physics

Author:

Satheesh M.
Nano Functional Materials Laboratory
Department of Physics
Cochin University of Science and Technology
Cochin - 682 022, Kerala, India.
Email: satheeshmaani@gmail.com

Supervisor:

Prof. M. Junaid Bushiri
Nano Functional Materials Laboratory
Department of Physics
Cochin University of Science and Technology
Cochin - 682 022, Kerala, India.
Email: junaidbushiri@gmail.com

Front cover:

August 2018

Department of Physics
Cochin University of Science and Technology
Cochin- 682 022, Kerala, India

Dr. M. Junaid Bushiri
Professor
Department of Physics
Cochin University of Science and Technology
Cochin- 682 022, Kerala, India.

Certificate

*Certified that the work presented in this thesis entitled "**Magnetic properties of iron oxide and iron oxide in graphitic matrix**" submitted by Mr. Satheesh M. in partial fulfilment of the requirements for the degree of Doctor of Philosophy in Physics to Cochin University of Science and Technology, is an authentic and bonafide record of the original research work carried out by him under my supervision at the Department of Physics. Further, the results embodied in this thesis, in full or in part, have not been submitted previously for the award of any degree. All the relevant corrections and modifications suggested by the audience during the pre-synopsis seminar and recommended by the Doctoral committee have been incorporated in the thesis.*

Cochin -22
Date: 21-08-2018

Prof. M. Junaid Bushiri
(Supervising Guide)

Phone: +91-4842577404 Fax: 91 4842577595, Email: junaidbushiri@cusat.ac.in

Declaration

*Certified that the work presented in this thesis entitled "**Magnetic properties of iron oxide and iron oxide in graphitic matrix**" is based on the original research work done by me under the supervision and guidance of Prof. M. Junaid Bushiri, Department of Physics, Cochin University of Science and Technology, Cochin-682 022 and has not been included in any other thesis submitted previously for the award of any degree.*

Cochin - 22 **Satheesh M.**
Dated:13/08/2018

Acknowledgements

A number of peoples directly and indirectly helped me during my Ph.D. years and completion of this thesis. When I look back; I understand that this thesis wouldn't be complete without their help and motivation. I use this occasion to express my thanks to all my teachers and friends from my nursery days onwards.

First and foremost I would like to thank Prof. M. Junaid Bushiri my supervising guide and Head, Department of Physics for his valuable guidance and support throughout my research period. He is always ready to help and discuss me with new research ideas.

I express my sincere gratitude to all the former Heads of the Department Prof. S. Jayalakshmi, Prof. B. Pradeep and Prof. M. R. Anantharaman for permitting me to use the research facilities in the Department. I would like to thank my doctoral committee member Prof. M. K. Jayaraj and all the other teachers in Department of Physics.

I express my thanks to Prof. S. Jayalakshmi and Dr. Anil Kumar of Department of Physics, CUSAT for allowing and me to done *dc* conductivity analysis of samples in their laboratory. I express my gratitude to Prof. M. K. Jayaraj and his laboratory members for XRD and Raman analysis.

It is my pleasure and proud to thank my physics teacher Miss. Vanajakumari, Head Mistress, C.F.D.V.H.S.S, Mathoor for her care and encouragement. I would like to thank V. Vijayakumar sir, D. Divya mam, Ambily mam, Sunitha mam and O. K. Ramesh sir from Govt. Victoria College, Palakkad for their support and encouragement during college days.

I thank Dr. Shibu Eappen, Mr. Adarsh, Mr. Melvin Baby, SAIF STIC, CUSAT for SEM and ICP-AES analysis. I am expressing my thanks to

Dr. Anuradha Ashok and Mr. Vijayaraghavan, PSG Institute of advanced studies, Peelamaedu, Tamilnadu for TEM analysis.

I am obliged to Dr. Senoy Thomas, Material Science and Technology Division, NIIST, Thiruvananthapuram for SQUID measurement. I am very happy to express my sincere gratitude to Prof. K. G. Suresh, Head, Department of Physics, IIT Bombay for magnetic measurement and his valuable suggestions. I feel proud for collaborating with his during my Ph.D. years.

I am expressing my thanks to Mr. Sivaramakrishnan, SAIF, IIT Madras for VSM analysis. I am thankful to all non teaching and library staff of the Department of Physics, CUSAT for all the help and cooperation. I acknowledge University Grants Commission, Government of India for providing Rajiv Gandhi National Fellowship during the research period.

Nano functional Materials Laboratory is a good place to work. I am deeply thankful to its past and present members for their support and help to Dr. Sajan P, Dr. Vinod V, Miss. Shajira, Mr. Ganesh Chanraprabhu, Miss Bini B nair, Mr. Abdul Rasheed Paloly, Mr. Krishna Sagar C K, Miss. Beenamol, Mr.Johncy Thomas, Miss Divya N G, Dr. Girish and Miss Haseena.

I thank all my school, B.Sc., M.Sc. classmates, seniors, juniors, friends from other laboratory of this department and my hostel roommates (Mr. Anurrop A and Mr.Kurias K Markose) for making a joyful life.

I have no words to express my gratitude and feeling towards my mother, father (Late) and sisters for their caring and support throughout my life. I thank all my relatives for their help and support.

Last but not least, I thank all my well-wishers and friends who have supported me in this venture. Above all, I thank God Almighty.

Satheesh M.

Dedicated to my

Parents and Teachers .....

Contents

List of Figures

Preface

Scientific world has undergone a massive development in the last several years, contributed to magnetic materials and devices based on it, which helped to improve the quality of standard of living of human beings. Recently, nanoparticles of magnetic materials are focus of attention of researchers because of its potential applications for magnetic storage, magnetic resonance imaging as a contrasting agent, hyperthermia treatment, targeted drug delivery and adsorption removal of heavy metal ions from contaminated water etc. Iron oxide has unique place among the magnetic nanomaterials which can be used for medical treatment and water purification since it is an earth abundant and ecofriedly material. Interestingly, iron oxide exists in three stable phases, viz. hematite (α-Fe_2O_3), maghemite (γ-Fe_2O_3) and magnetite (Fe_3O_4). Among these, α-Fe_2O_3 posses hexagonal crystal structure which exhibit weak ferromagnetic property above its Morin transition temperature at 263 K. Room temperature ferromagnetic phase of iron oxide (γ-Fe_2O_3) crystallises in cubic system. Magnetic and physical properties of iron oxide can be improved by making a combination of iron oxide along with either crystalline carbon or amorphous carbon. These new materials are good for medical applications and water treatment. The present study focussed on the synthesis and magnetic studies of α-Fe_2O_3, α-Fe_2O_3/graphene oxide, α/γ-Fe_2O_3 and α/γ-Fe_2O_3/graphite nanomaterials. This thesis also deals with the Ni(II) adsorption removal studies of combustion synthesised α/γ-Fe_2O_3 and α/γ-Fe_2O_3/graphite. The thesis contains seven chapters which includes the characterisation technique used for the analysis of materials and scientific importance of iron oxide.

Chapter 1 deals with the basics of magnetism, classification of magnetic materials and its applications. This chapter also includes fundamental properties and applications of α-Fe_2O_3 (hematite) and γ-Fe_2O_3 (maghemite). The basics of adsorption, adsorption removal of heavy metal ion are also discussed in this chapter. Review of literature related to the topic of research and motivation behind

this work is also included in this chapter. **Chapter 2** contains details about solvothermal and combustion synthesis process of materials. This chapter also deals with the basic principles and operational procedures of various characterisation tools used in the present study.

Chapter 3 describes the effect of solvents on the formation of spheroid and pseudo cubic hematite microstructures. These samples are characterised using XRD, FTIR, SEM, EDAX, DRS. This chapter also deals with the *dc* conductivity studies, optical band gap and magnetic properties of hematite microstructures. Growth of hematite crystals using methanol (H-M), methanol-water 1:1 (H-MW), propanol (H-P) and propanol-water 1:1 (H-PW) as solvent of precursor salts by solvothermal method reveals that crystalline size, shape and crystalline defects in crystals can be modified with different solvent combination of precursor solution. Variation in optical, *dc* conductivity and magnetic properties of solvothermaly grown spheroid shaped hematite crystals are attributed to its size, shape and population of oxygen vacancies. Relatively higher order room temperature coercivity are observed from spheroid (5.23 kOe) and micro pseudocubic crystals (6.16 kOe) grown with methanol and propanol-water combinations respectively. The enhanced room temperature magnetic coercivity observed in spheroid and pseudocubic micro crystals is contributed to shape anisotropy and defect related spin pinning effects. Spheroid sample grown with methanol shows high intensity UV absorption peaks and displays two Morin transition temperatures which may be related to inhomogeneous particle distribution. Shifting of Morin transition temperature of the spheroid and pseudocubic hematite samples compared to its bulk counterpart is attributed to variation in number of oxygen vacancies. The morphology dependent optical and magnetic properties presented in this study provide information about the optimisation of synthesis condition of new hematite micro structures for future technological applications.

Chapter 4 describes the synthesis of spherical shaped α-Fe_2O_3 and α-Fe_2O_3/GO nanocomposites in acetonitrile medium by solvothermal method at 200 ^{0}C. Synthesized α-Fe_2O_3 and α-Fe_2O_3/GO nanocomposites are characterized with XRD, FTIR, Raman, FESEM, TEM, SAED, EDAX and DRS. This chapter also discusses the optical band gap, *dc* conductivity and magnetic properties of α-Fe_2O_3/GO nanocomposite. Graphene oxide in spherical shaped α-Fe_2O_3/GO nanocomposites synthesized with GO and precursor salts of α-Fe_2O_3 in acetonitrile medium is disordered than GO as understood from Raman studies. The electronic structure of GO is not disturbing the band structure of α-Fe_2O_3, room temperature electrical conductivity and optical band gap of α-Fe_2O_3/GO are comparable to semiconductors.. Magnetic coercivity of α-Fe_2O_3 is increasing on lowering the temperature of the sample to 5 K due to frozen canted spin. The slight increase in magnetic coercivity of α-Fe_2O_3/GO with respect to α-Fe_2O_3 at room temperature and enhancement at 5 K is synergetic effect attributed to RKKY interactions between 'd' electrons of α-Fe_2O_3 and the conducting electrons of GO. The remanence and saturation magnetisation of α-Fe_2O_3/GO is higher than α-Fe_2O_3 may be related to the presence of super-paramagnetic graphene oxide. The thermal hysteresis at Morin transition temperature of the order of 11 K, is observed in α-Fe_2O_3/GO nanocomposites.

The **chapter 5** includes the synthesis of α/γ-Fe_2O_3 by cost effective combustion method. Characterisation of these materials is done with XRD, FTIR, TEM, SAED, DRS, and BET etc. The optical band gap and room temperature magnetic coercivity is found to be almost equal for both α and γ enriched α/γ-Fe_2O_3 nanoparticles. Interestingly, γ enriched α/γ-Fe_2O_3 are more ferromagnetic than α enriched sample which is due to the presence of higher quantity of ferromagnetic γ-Fe_2O_3 in the sample. The Brunauer–Emmett–Teller (BET) surface area of γ enriched α/γ-Fe_2O_3 is found to be 75 m^2/g. The higher surface area and ferromagnetic properties make it a suitable candidate for the adsorption removal of heavy metal ions from contaminated water. 20 mg/L of this sample

shows 90 % Ni(II) ion removal efficiency in 0.1 M nickel acetate solution at a pH of 8 within 8 minutes.

Chapter 6 comprises of the combustion synthesis of mixed phase of α and γ Fe_2O_3 nanoparticle in graphitic matrix (0.3, 0.6, 0.9 g) with the precursor salt of iron oxide and graphite. The samples are characterized with XRD, FTIR, Raman, TEM, EDAX, SAED, DRS, and BET etc. The *dc* conductivity, optical band gap and magnetic properties of these materials are also investigated. These samples shows band gap similar to that of mixed phase α and γ Fe_2O_3. The magnetic remanence and saturation of samples are found to decreases with increasing quantity of graphite added to the precursor salt before the synthesis. Enhanced Ni(II) adsorption property of 0.3 g graphite added α/γ-Fe_2O_3 is related to increase in surface area of the material as understood from BET measurement. **Chapter 7** comprises of overall summary of the present work and its future scope.

List of publications

Journal papers

1) **M. Satheesh,** M. Junaid Bushiri, Abdul Rasheed Paloly, K. G. Suresh**,** J. Phys. Chem. Solids, **98**, 247 (2016) "Influence of solvothermal growth condition on morphological formation of hematite spheroid and pseudocubic micro structures and its magnetic coercivity" (Included in this thesis).
2) **M. Satheesh,** M. Junaid Bushiri, Abdul Rasheed Paloly, C. K. Krishna Sagar, K. G. Suresh, Phys. Status Solidi A , **215**, 1700705 (2018) "Improved coercivity of solvothermally grown hematite (α-Fe_2O_3) and hematite/graphe oxide nanocomposites (α-Fe_2O_3/GO) at low temperature" (Included in this thesis).
3) **M. Satheesh,** M. Junaid Bushiri, Abdul Rasheed Paloly, International journal of nanoscience (Under review) **"**Magnetic properties of iron oxide nanocomposites enriched with α-Fe_2O_3 and γ-Fe_2O_3" (Included in this thesis).
4) Abdul Rasheed Paloly, **M. Satheesh,** Sreekumar Rajappan Achary, Vicente Munoz-Sanjose**,** M Junaid Bushiri "Growth of tin oxide thin films composed of nanoparticles on hydrophilic and hydrophobic glass substrates by spray pyrolysis technique" Appl. Surf. Scie. **357**, 915, (2015).

Conference papers

1) "Magnetic properties of combustion derived maghemite (γ-Fe_2O_3) nanoparticles National conference on nanophotonics", (Oral Presentation), **M. Satheesh**, M. Junaid Bushiri, National Conference-NCNP- March 6-7, 2014, School of Physics, Bharatidasan University, Tiruchirappalli, Tamilnadu.
2) "Pb(II) adsorption study by combustion derived maghemite nanoparticles" **M. Satheesh**, M. Junaid Bushiri, International Conference on Energy Harvesting Storage and Conversion-IC-EEE-February 5-7, 2015, Department of physics, CUSAT, Cochin, Kerala.
3) "Optical Properties of hematite (α-Fe_2O_3) hexagonal microplates synthesized by solvothermal method". **M. Satheesh**, M. Junaid Bushiri, Abdul Rasheed Paloly, Fourth Iinternational Conference on Frontiers in Nanoscience and Technlogy, Cochin nano- February 20-23, 2016, Department of physics, CUSAT, Kerala.
4) "Effect of molarity of precursor solution and the substrate temperature on band gap of spray pyrolytcally grown SnO_2 thin films" Abdul Rasheed Paloly, **M. Satheesh**, M. Junaid Bushiri, National Seminar on Advanced Materials Science-september-29-30, 2014, Department of Physics, Manonmaniam Sundar University, Tirunelveli, Tamil Nadu.
5) "Optical properties of Al doped tin oxide thin films grown over amorphous substrate by spray pyrolysis" Abdul Rasheed Paloly, **M. Satheesh**, Shyama George K, Zeenath K, M Junaid Bushiri, Fourth International Conference on Frontiers in Nanoscience and Technology, Cochin nano- February 20-23 2016, Department of physics, CUSAT, Kerala.

Chapter 1

Fundamental aspects of magnetism and adsorption

Contents

1.1. Introduction

Synthetic and natural materials play crucial role for improving the standard of living and quality of life of the modern society. Among these materials, semiconducting and magnetic materials attracted the attention of the scientific world to a great extent. The development of conducting and semiconducting materials has changed human life drastically. The semiconducting materials lead to the beginning of electronics and are having wide range of applications in electronic devices. The miniaturization of electronic chips reduced the size of electronic equipment's and helped in making more compact electronic devices. The development of technology made it possible to make highly promising, smaller and smaller devices, even a super computer of the size of a pen [Ohn K *et al; 2008*]. Micro and nanomaterials got greater attention in technological development, since the size of materials reduced to nano level, surface area to volume ratio

increases and such materials show superior properties than its bulk counterpart, consequently interesting electrical, optical and physical properties. The electrical, mechanical, thermal, optical, catalytical and magnetic properties of nanaomaterials are different from that of its bulk materials.

The mechanical strength of nanomaterials are very high, compared to their bulk structures. Recently invented materials like graphene, show different properties with respect to the number of the layers in it. 2D graphene layers are highly conducting than 3D graphites [Yakimchak E, *et al; 2017*]. The good conducting property of graphene oxide is suitable for the making of electronic display, battery, sensors etc. Magnetic materials are very important materials for a variety of applications such as magnetic storage, spin walve, MRI contrasting, hyperthermia etc [Nag S, *et al; 2016*]. Transition metals like iron, cobalt, nickel and rare earth metal like neodymium, gadolinium etc. are good magnetic materials. Alloys of these materials also exhibit magnetic properties. Different types of magnetism observed in materials are mostly based on the spins of the atoms present in the materials. On reducing the size of the materials to nano level, materials behave entirely different from its bulk counterpart, some of the ferromagnetic material become superpararmagnetic material. Now a days, the research industry focuses on single material which can have multi-functional properties like magnetism, electrical conductivity etc. Some of these materials are likely to exhibit surface plasmon resonance and photocatalytic properties. Heavy metal ions also can be removed from contaminated water by using multifunctional materials.

1.2. Magnetic materials

Magnetism is an interesting physical property, exhibited by materials mostly in transition and rare-earth metals based compounds. Magnetic property of a material is related to spin and orbital motion of unpaired electrons present in the atoms and the way in which unpaired electrons are aligned. All materials in nature exhibit magnetism in the presence of applied magnetic field (H) and magnetization is likely to be induced inside the material (M). The induced magnetization inside the material is directly proportional to the applied field strength (H) [Culity B D *et al*; 2009].

$$M \alpha H$$

$$M = \chi H$$

Where χ is the magnetic susceptibility of the given material. Magnetic susceptibility can be written as $\chi = \frac{M}{H}$, it gives information about how much a material is magnetized. On the basis of magnetic susceptibility, materials are classified as ferromagnetic, antiferromagnetic, paramagnetic and diamagnetic ones.

1.2.1. Ferromagnetism

Ferromagnetic materials possess relatively large positive values of magnetic susceptibility. These materials are highly magnetized in the presence of applied field and magnetization may exist in the materials even after the removal of the applied field. The alignment of magnetic moments in the atomic lattices are seen in ferromagnetic materials even in the absence of applied field [Culity B D *et al*; 2009]. Magnetic moments in ferromagnetic materials align along the magnetic easy direction, which depends on crystal structure, size, shape etc. of the materials [Moskowitz B

M *et al*; 1991]. Interestingly, in a ferromagnetic material each atom possess magnetic moments and these magnetic moments are randomly aligned in such a way that net magnetization of the bulk material is zero, in the absence of applied field. In a particular region of the material most of the magnetic moments are in the same direction this is called magnetic domain. Magnetic domains are in random direction in the absence of magnetic field. However, a short range interaction occurs between neighboring magnetic moments in the presence of applied field, which leads to the positive alignment towards the applied field. When the applied field is strong, magnetic moments in all domains are aligned and materials are fully magnetized in the direction of the applied field. This maximum magnetization achieved by the material in the presence of a strong applied field is known as saturation magnetization [Culity B D *et al*; 2009, Kannan M K *et al*; 2016]. Magnetisation does not retain its original path when the applied field is reversed, the lagging of magnetization with applied field is termed as hysteresis loop. The reverse field required to remove magnetization inside the materials after magnetic saturation is known as coercivity or coercive field. A very weak field of the order of 10^{-2}gauss is enough to produce magnetization inside ferromagnetic material of about 10^{3}gauss [Dekker A J; 1981]. The magnetization produced in a ferromagnetic material by applying external field (H) can be written as $M=N\mu_B^2H/KT$, where N is number of magnetic moments, μ_B is permeability of the material, H is applied field strength, K is Boltzmann constant and T is temperature of the system [Dekker A J; 1981].

Magnetic hysteresis behavior remains up to Curie temperature (θ_f). Ferromagnetic material becomes paramagnetic when the temperature of the

material is above Curie temperature. The susceptibility of materials obey Curie-Weiss law above Curie temperature.

$$\chi = \frac{C}{T-\theta}$$

where C is Curie constant, θ is paramagnetic Curie temperature (which is always higher than θ_f) and T is temperature of the system [Dekker A J; 1981].

1.2.2. Antiferromagnetism

In certain materials there exists two sublattices, the magnetic moments of these lattices are in opposite direction. Net magnetization is zero in the absence of applied field. However, magnetization will grow with the application of the applied magnetic field. These types of materials are generally called antiferromagnetic materials. The physics of these materials are interesting one for scientific investigation. Its atoms are having permanent dipole moments, but the negative interaction among them causes the neighboring moments to align in the antiparallel way. If the antiferromagnetic material consists of only single magnetic species, it will choose antiparallel sub lattice of crystal in such a way that there is no spontaneous magnetization [Kannan M K *et al*; 2016].

The antiferromagnetic behavior of materials exist up to a particular temperature is known as Neel's temperature, above which materials become paramagnetic. Antiferromagnetic material has no net moment below Neel's temperature since the spins are antiparallelly aligned. If the antiferromagnet consist of two different magnetic species, which can be assumed as a peculiar case, in which both sub lattice A and B have same saturation magnetization $C_A=C_B$ [Kittel C; 1996]. Neel's temperature of such

antiferromagnetic materials can be represented as $T_N = \mu C$, where C refers to a single sublattice. Susceptibility of antiferromagnet above Neel's temperature obeys the relation [Kittel C; 1996].

$$\chi = 2C/T+T_N$$

Where T_N is Neel's temperature of antiferromagnet and T is the temperature of system.

1.2.3. Ferrimagnetism

In some materials there exists two sub-lattices similar to antiferromagnetic one, but the strength of magnetic moments in the opposite sub-lattices are not equal. But it shows spontaneous magnetization like ferromagnet. Net magnetization is zero in the absence of applied field. However, magnetization will grow with the application of the applied magnetic field. These types of materials are generally called ferrimagnetic materials. Ferrimagnetic material becomes paramagnetic one, above Curie temperature. Double oxides of iron and other metals usually exhibit ferromagnetic property [Culity B D *et al*; 2009]. Most of the ferromagnetic materials exist either in cubic or hexagonal crystal system. Cubic ferrimagnet (ferrite) have general formula $MO.Fe_2O_3$, where M is metal ions like Fe, Ni, Mg, Mn, Co etc. $CoO.Fe_2O_3$ is an example for this type of materials. Hexagonal ferrites are mostly compounds of barium and strontium. $SrO.6Fe_2O_3$ and $BaO.6Fe_2O_3$ are included in this group. These materials never obey Curie-Weiss law [Culity B D *et al*; 2009].

1.2.4. Diamagnetism

Presence of paired electrons in atoms of certain materials exhibit diamagnetic properties contributed to orbital motion of electrons [Semat H *et al*; 1958]. These orbital motion of electrons in atoms causes the formation of small inherent field in a material which, in opposite direction to the applied field. These materials are usually weakly repelled by magnetic field.

Majority of naturally occurring materials and organic compounds are diamagnetic ones. Noble gases like He, Ne etc. possessing closed electronic configuration also show diamagnetic behavior. Ionic crystals like NaCl are showing diamagnetic behavior due to the presence of ionic bonds between Na^+ and Cl^- [Culity B D *et al*; 2009].

1.3. Size dependent magnetism

The particle size also has an important effect on magnetic properties of a material. When the particle size of ferro or ferrimagnetic material reduces to a few nanometer (below 10 nm), the particle behaves as single domain and become superparamagnetic [Guivar J A R *et al*; 2014]. These properties are related to quantum confinement effect and gives interesting magnetic properties like Superparamagnetism.

1.3.1. Superparamagnetism

Like paramagnet, superparamagnetic materials also show almost zero coercivity and remanence in the presence of an applied field. The saturation magnetization of superparamagnetic material is very high compared to paramagnet in the presence of the applied field. The magnetic

susceptibility of single domain superparamagnetic material is also higher compared to multidomain paramagnetic materials. In superparamagnetic materials, each single particle will be aligned in the direction of applied field through an easy axis. The absence of multidomain structure, interaction of spin inside the domain etc. make it as superior saturating one compared to other magnetic materials.

Usually volume of superparamagnetic materials can be represented as

$$V_{sp}=\frac{25k_BT}{k}$$

Where, k_B is Boltzmann constant, T is temperature of material, k is anisotropy constant of the material.

From the expression for particle size, blocking temperature of superparamagnetic material can be determined [Guivar J A R *et al*; 2014].

$$T_B=\frac{Kv_{sp}}{25k_B}$$

Blocking temperature of superparamagnetic material is the temperature above which its superparamagnetism is lost. Most of the nanomagnetic materials exhibit superparamagnetic behavior. These materials are having tremendous applications in modern technology. Graphite coated superparamagnetic Fe nanoparticles can be used for drug delivery applications, hyperthermia treatment, magnetic ink etc.

1.4. Temperature dependent magnetism and magnetic phase transitions.

Temperature has an important role in magnetism and magnetic phase transitions of materials. When a ferromagnetic materials is continuously

heated its magnetic property will lose at a particular temperature, this temperature is known as Curie temperature [Culity B D *et al*; 2009]. Other important magnetic transition temperatures are Neel's and Morin transition temperature. Neel's temperate is a temperature at which antiferromagnetic material become paramagnet [Coey J M D; 2010].

Hematite shows antiferromagnetic behavior below Morin transition temperature (263 K), above which it exhibits weak ferromagnetic property [Tadic M *et al*; 2011]. The weak ferromagnetic behavior of hematite exists up to 950 K, after which it shows paramagnetic property [Coey J M D; 2010].

1.5. Magnetic anisotropy

Magnetic materials are likely to show anisotropic behavior which may be attributed to non-uniform shape, size, presence of impurity atoms and spin-orbital interaction quantized state of electrons etc. Magnetic parameters like magnetic saturation, coercivity, remanence etc. may vary in a material due to magnetic anisotropy. This anisotropy can be divided into intrinsic and induced magnetic anisotropys. The induced anisotropy includes, anisotropy generated due to magneto crystalline effect, shape of the material etc.

1.5.1. Magneto crystalline anisotropy

Alignment of spins along specific crystallographic direction produces magneto crystalline anisotropy. So this is dependent on the orientation of crystal planes of metal ions. In the case of body centered Fe, the preferred direction is (100) [Kannan M K *et al*; 2016]. The final

spontaneous magnetization of the material is independent of the direction of applied field. Spin orbital interaction is the major contributing factor for the magneto crystalline anisotropy of the material.

1.5.2. Shape anisotropy

Magnetic properties of the materials are mostly shape dependent. The alignment of magnetic spins in a materials with particular shape are solely depends on length, breadth and height of the individual structures. The spins are preferred to align in longer axis and are known as magnetic easy axis. The demagnetization field is very high along this longer axis, which makes spins to choose these directions.

The demagnetization energy can be written as $E_{ms} = \frac{1}{2}\mu_0 N_d M_s^2$ [Kannan M K *et al*; 2016], where M_s is saturation magnetization, N_d is demagnetisation factor and μ_0 is permeability of free space.

1.5.3. Induced magnetic anisotropy

Magnetic anisotropy can be induced in a material by adopting different material processing methods like annealing, rolling and irradiation [Culity B D *et al*; 2009]. Magnitude of anisotropy and magnetic easy axis also changes during the processing of materials. As a result of processing of materials with above mentioned techniques, lattice parameters of the materials may change its dimension. In some cases crystalline phases may change as in the case of γ-Fe_2O_3 which convertes in to α-Fe_2O_3 after heat treatment or annealing.

1.6. Adsorption process

Adsorption is an adhesive process between adsorbate and adsorbent, adsorbate is adsorbed on the surface of adsorbent. Adsorbate is a substance contained in the liquid, which undergo adsorption on the surface of adsorbent. Adsorbent may exist in solid, liquid or gaseous phases on to which adsorbate are deposited. On the basis of interaction process and forces, adsorption can be divided into physisorption (physical adsorption) and chemisorption (chemical adsorption) [Thomas M *et al;* 2015].

Physical adsorption (physisorption) involves weak forces between the adsorbed molecules. In this process, adsorbed molecules are not fixed in to the adsorbent and are free to move over the surface [Sawyer N C *et al;* 1994]. Here physical interaction between molecules depends on dipole-dipole interactions, dispersion interactions and hydrogen bondings. Chemical adsorption is linked to strong electrostatic forces between adsorbate and adsorbent [Sawyer N C *et al;* 1994]. But in the case of chemisorptions, the interaction between adsorbate and adsorbent occur through covalent or electrostatic chemical bond and hence there exist possibilities for the formation of new compounds. In this case, desorption and reuse of adsorbent is not possible to a certain extent. Physisorption is a multilayer adsorption while chemisorption is a monolayer adsorption. Interestingly in the case of physisorption, desorption process is possible, and hence the material can be reused. In physisorption process, the thermodynamic equilibrium is reached very easily, whereas the system does not reach equilibrium in chemisorption.

1.6.1. Heavy metal ion adsorption

Heavy metal ions such as Cd(II), Pb(II), Ni(II), Hg(II), Co(II), As(III) etc. are present in water, the aforesaid elemental composition may depends upon the source and place of the water [Lagashetty L *et al*; 2010]. Even some industries also leaving out water contaminated with heavy metals in to water bodies. These metal ions are harmful, which can be removed from the contaminated water with suitable adsorbent materials. In this case, heavy metal ions can be considered as adsorbate, which are adsorbed on adsorbent materials. The material showing physisorption of heavy metals are usually taken as efficient absorbent, since it can be reused.

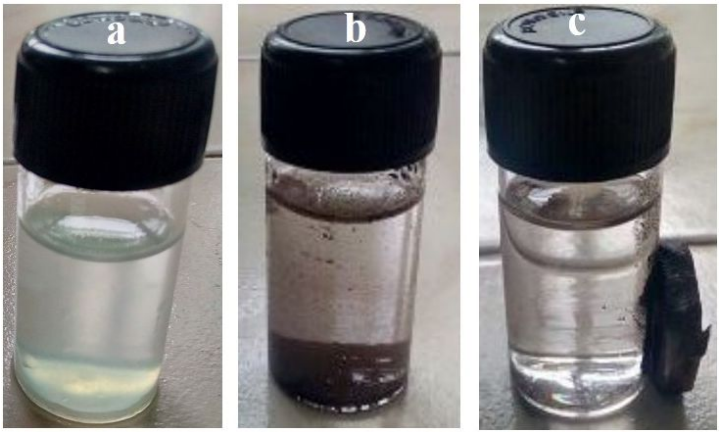

Figure 1.1. *(a) 0.1 M Nickel acetate solution (b) 0.1 M Nickel acetate solution treated with 20 mg/L iron oxide (c) Ni(II) adsorbed iron oxide separated using magnet.(Photograph of Nickel ion adsorption experiment from the present study)*

1.7. Introduction to iron Oxide

Iron oxide is an important material which is being used for various technological applications. Iron oxides exist in nearly eight different phases (α-Fe_2O_3, β-Fe_2O_3, γ-Fe_2O_3, ε-Fe_2O_3, Fe_3O_4, Fe_4O_5, Fe_5O_6 and Fe_5O_7). These materials crystallizes in cubic (β-Fe_2O_3, γ-Fe_2O_3, Fe_3O_4), orthorhombic

(ε-Fe_2O_3, Fe_4O_5, Fe_5O_6 and Fe_5O_7) and hexagonal (α-Fe_2O_3) crystal system. Among these phases, α-Fe_2O_3, γ-Fe_2O_3 and Fe_3O_4 are relatively stable than the other ones. Iron oxide is particularly used as a magnetic storage materials, catalyst, adsorption materials, gas sensing, anode materials and medical applications. Among the stable phases of iron oxide α-Fe_2O_3, γ-Fe_2O_3 are naturally occurring minerals, β-Fe_2O_3 and ε-Fe_2O_3, mostly synthesized ones. The polymorphs of iron oxide like α-Fe_2O_3, β-Fe_2O_3, γ-Fe_2O_3, ε-Fe_2O_3 show different magnetic nature at room temperature. At room temperature, α-Fe_2O_3, β-Fe_2O_3, γ-Fe_2O_3 and ε-Fe_2O_3 are weak ferromagnetic, paramagnetic, ferromagnetic and canted antiferromagnetic respectively [Wilde R E *et al*; 1970, Weiser H B *et al;* 1942]. Fe_3O_4 is another important stable phase of iron oxide which shows ferrimagnetic nature at room temperature. When the size of γ-Fe_2O_3 and Fe_3O_4 reduces to a critical size below a few nanometer, each atoms behave as single domain and materials became suerparamagnetic [Pavel K *et al*; 2013]. Super-parmagnetic materials have nearly zero coericivity and remanence. These superparmagnetic materials can be used for drug delivery, MRI contrast and hyperthermia treatment etc. [Margarthe H A *et al*; 2009].

1.7.1. Hematite (α-Fe_2O_3)

Hematite is the most stable phase of iron oxide which exists as a mineral in nature. The crystal structure of hematite is a rhombohedraly centered hexagonal, in which Fe^{3+} ions occupy the octahedral and tetrahedral sites of hexagonally close packed O lattice. Its crystal structure belongs to R$\bar{3}$c space group with lattice parameter a = 5.036 Å and c = 13.749 Å [Cornell R M *et al*; 2008]. Hematite shows n-type

semiconducting property and its optical band gap is around 2.2 eV [Mitra S *et al*; 2007]. Magnetic properties of hematite are temperature dependent, it shows two magnetic transition temperatures, they are Morin and Neel's temperature. The Morin and Neel's transition temperature of bulk hematite are ~ 260 and 950 K respectively [Wilde R E *et al*; 1970, Cornell R M *et al*; 2008]. Hematite shows weak ferromagnetic property above the Morin transition temperature, below that it exhibits antiferromagnetic property. Morin transition temperatures of the materials depends on particle size and rapidly decreases when the size is reduced to below 100 nm [Vandenberg R E *et al*; 2001]. Morin transition temperature is usually not observed in hyperfine particles of hematite.

1.7.2. Maghemite (γ-Fe_2O_3)

The crystal structure of magnetite is cubic inverse spinel structure (γ-Fe_2O_3), in which Fe^{3+} ions occupy the octahedral and tetrahedral sites of O lattice. Maghemite crystal belongs to either one of the space group, cubic $Fd\bar{3}m$ or (a = 8.339 Å), cubic $P4_332$ (a = 8.351 Å) [Zboril R *et al;* 2002, Machala L *et al;* 2011]. Maghemite is a semiconducting material with band gap of around 2 eV [Martinez A I *et al;* 2009].

Maghemite shows ferro or ferrimagnetic behavior at room temperature, its magnetic property will lose at Curie temperature [Ortega D *et al;* 2012]. If some of the spins of maghemite may canted due to crystalline defects, these materials will show ferri magnetism. The reported Curie temperature of maghemite is in the range of 790-980 K which also depends on particle size, shape and crystallinity of the material [Tucek J *et al*; 2006]. Ferromagnetic maghemite is transferred to paramagnetic phase at

Curie temperature. Similar to other ferromagnetic materials, maghemite become single domain materials and it shows superparmagnetic property when the particle size is reduced to below critical size.

1.8 Review of literature

Iron oxide is one of the most important transition metal oxides which has wide technological applications for magnetic data storage, catalysts, pigments, gas sensors etc. Micro and nano structures of iron oxide can be synthesized by various synthesis processes including chemical precipitation, sol gel, auto combustion, hydrothermal, emulsion, precipitation, electro deposition, solvothermal methods etc. Among these synthesis processes, hydrothermal method is quite unique due to several advantages such as for getting highly pure sample, uniform size distribution, controlled morphology etc.

Several authors had reported the synthesis of hematite nanoparticles with different morphologies through hydrothermal process. The hydrothermal synthesis of micro and nanosized Fe_2O_3 having sub-micron flower morphologies were reported [Nuli Y *et al;* 2008]. Single crystalline α-Fe_2O_3 nanostructures having micro-pine and snowflakes like morphologies were obtained by hydrothermal process using NP-9 surfactant [He K *et al;* 2008]. Ma J *et al* reported the synthesis of various hierarchical structures of hematite such as amorphous spheres, single crystalline nanoflakes, microlayered structures etc. [Ma J *et al;* 2013]. These structures were developed to investigate its storage efficiencies for lithium ion battery applications [Ma J *et al;* 2013]. Spherical, diamond and plate like hematite

structures were also synthesized by varying the pH of the precursor solutions, by hydrothermal technique [Dong Q *et al;* 2009].

Nano needle like morphology was obtained for ferromagnetic Fe_2O_3 grown by hydrothermal process from iron silica complex and ethyl acetate with ethanol solvent [Lee J B *et al;* 2014]. In 2015, Ayachi A A *et al* reported the synthesis of uniform sized α-Fe_2O_3 nanoplatelets, using ferric aqueous solution with urea as surfactant [Ayachi A A *et al; 2015*]. Zhang Q *et al* reported the hydrothermal synthesis of mesoporous flowers of α-Fe_2O_3 in the absence of surfactant [Zhang Q *et al;* 2013]. α-Fe_2O_3 and γ-Fe_2O_3 mixed phases with various morphologies were obtained by varying the content of iron precursor salts [Syed F N *et al;* 2015].

Synthesis temperature can also influence the morphologies and particle size of the samples along with its physical properties. Porous α-Fe_2O_3 nanospheres with excellent gas sensing properties was prepared by glycine assisted hydrothermal methods [Chen H *et al;* 2009]. α-Fe_2O_3 having different shapes such as micro double-spheres, tetrakaidecahedron and nanoparticle aggregated ellipsoid were synthesized by varying the concentration of octadecylamine by hydrothermal process [Liu Z *et al;* 2012]. Template free hydrothermal method was explored for the controlled synthesis of α-Fe_2O_3 nanostructures in HEPES solution [Li H *et al;* 2011].

Wang *et al* reported the synthesis of hematite hierarchical structures such as stalactite-like, cluster-like and coral-like etc., by hydrothermal processes, with the aid of dual surfactants [Wang L *et al;* 2011]. Single crystalline nanostructures of α-Fe_2O_3 with dendrites and snowflakes like morphologies were synthesized hydrothermally using CTAB and PEG as

surfactants and the morphology dependent magnetic properties of these samples were investigated [Bharathi S *et al;* 2009].

1.8.1. Hematite nanoparticles

Hydrothermal synthesis of hematite nanoparticles has got great attraction due to the fact that it is possible to control the particle size and these materials are suitable for various technological applications. Hematite nanoparticles and nanocubes were synthesized by hydrothermal methods and these crystals showed shape dependent optical properties [Wang T *et al;* 2014]. Uniform sized α-Fe_2O_3 nanoparticles were synthesized by surfactant mediated hydrothermal technique [Xu C *et al;* 2011]. Wang L *et al* reported that the oriental attachments of the hematite nanoparticles lead to the formation of flower like morphologies during hydrothermal synthesis process [Wang L *et al*; 2008]. In 2016, Xu C *et al* reported that the aggregation of nanoparticles during the hydrothermal synthesis was limited by the use of poly vinyl alcohol (PVA) as a surfactant [Xu C *et al;* 2016]. Iron oxide nanoparticles dispersions were synthesized by hydrothermal root at 673 K and at pressure of 30 MPa [Tercero M D *et al;* 2014]. Alkali metal ions such as lithium, sodium and potassium induces the growth of mesoporous cube shaped α-Fe_2O_3 with improved magnetic properties as well as good degradation efficiency of methylene blue [Roy M *et al;* 2016]. Sajjadi S H *et al* reported the photodegradation of ionic dyes such as RB5, MB and RhB by using monodispersed hematite cubes synthesized by hydrothermal process [Sajjadi S H *et al;* 2017]. Thin film of hematite nanocubes synthesized by hydrothermal process on FTO substrate was reported as an efficient photoanode for water splitting [Liu K *et al;* 2015].

Carbon matrix incorporated with hematite nanoparticles was synthesized by hydrothermal process which was found to have superior physical properties compared to hematite. Hydrothermal process also resulted in the formation of hematite nanoparticle within the cavities of carbon nanotubes [Matsui K *et al;* 2017]. Hydrothermally synthesized 3D flower like α-Fe_2O_3/RGO hybrid composite was reported to be used as an efficient photoanode for dye-sensitized solar cells [Shang X *et al;* 2016].

Hematite nanorods have great importance for the scientific community. Nanorods with larger easy axis of magnetisation compared to other morphologies are favorable for good electrical and magnetic properties. The direct hydrothermal synthesis of single crystalline uniform nanorods of hematite with high aspect ratio was synthesized in the presence of 1,2-propanediamine by Li Z *et al* [Li Z *et al;* 2009]. Single crystalline α-Fe_2O_3 nanorods with polyhedral configuration were hydrothermally synthesized with the aid of CTAB surfactant [Jia B *et al;* 2007]. Hematite nanorods with various sizes were synthesized by changing the growth temperatures with a novel valve assisted pressure autoclave [Almeida T P *et al;* 2010]. Magnetic properties of hydrothermally synthesized hematite nanorods with length around 67 nm were studied [Mathew J *et al;* 2015].

Hematite with cube like morphologies was also attractive due to its shape dependent physical properties. Synthesis and growth mechanisms of hematite nanocubes obtained by template free hydrothermal process were reported [Su C *et al;* 2011]. Controlled synthesis of hematite nanocubes with average size around 250 nm was achieved with the presence of CTAB surfactant in the growth medium [Pu Z *et al;* 2006].

Solvothermal synthesis is also an efficient method, which can be successfully used for the synthesis of materials with controlled particle sizes, morphologies etc. In this synthesis processes, various solvents are used for the synthesis of nanoparticles instead of water, which is commonly used for the hydrothermal synthesis.

Hematite homogenous core shell structured spheres were synthesized by surfactant free solvothermal method in which ethanol was used as a solvent for the precursor salts [Lian S *et al;* 2012]. Rehman *et al* reported good catalytic properties for solvothermally grown hematite hexagonal nanoparticles [Rehman S *et al;* 2015]. Hematite nanoplates were developed by solvothermal method using isopropanol solvent [Yang P *et al;* 2015]. Different morphologies similar to grapes, cubes, dumbbells and microspheres were synthesized by dissolving same precursor salts in different solvents [Yu J S *et al;* 2014].

1.8.2. Combustion synthesized iron oxide

Combustion synthesis is an efficient and cost effective method for the preparation of nanoparticles. Several authors reported the synthesis of α-Fe_2O_3, γ-Fe_2O_3 and α-Fe_2O_3 and γ-Fe_2O_3 composites by combustion methods [Wang X *et al;* 2009, Ganachari S V *et al*; 2012, Deraz N M *et al;* 2012]. Depending on the oxidisers and fuels used for the combustion synthesis of iron oxide, the phases of the Fe_2O_3 (α-Fe_2O_3, γ-Fe_2O_3 or α/γ-Fe_2O_3) changes [Deraz N M *et al;* 2012]. Preparation of single phase of α-Fe_2O_3 nanoparticles using $FeCl_3$ oxidizer was reported by Wang X *et al* [Wang X *et al;* 2009]. α-Fe_2O_3 nanoflakes were synthesized by using iron nitrate (oxidizer) and glycine (fuel) [Pooja D *et al;* 2012]. Highly

mesoporous hematite nanoparticles showing visible light induced photocatalytic dye degradation properties were synthesized by changing the oxidizer to fuel ratio [Cao Z *et al;* 2015]. Dumb bell shaped α-Fe_2O_3 naoparticle was obtained using oxalyldihydrazide fuel by low temperature combustion synthesis process [Jahagirdar A A *et al;* 2013]. Combustion synthesis of γ-Fe_2O_3 nanoparticles using iron pentacarbonyl was reported [Jasinski J *et al;* 2005].

A new combustion root for the synthesis of γ-Fe_2O_3 from purified α-Fe_2O_3 as a precursor salt was reported by Venkataraman A *et al* [Venkataraman A *et al;* 2001]. Large scale synthesis of γ-Fe_2O_3 was achieved using ferric oxide (oxidizer) and poly ethylene glycol (PEG) [Ganachari V G *et al;* 2012]. Barinova T V *et al* reported the synthesis of mixed phase of α and γ Fe_2O_3 by combustion method [Barinova T V *et al;* 2012]. By changing the oxidizer to fuel ratio (iron nitrate:glycine), synthesis of mixed phases of α and γ Fe_2O_3 having different surface area were reported [Deshpande K *et al;* 2004]. In 2012, Deraz N M *et al* synthesized and analyzed the magnetic properties of α/γ-Fe_2O_3 nanoparticles [Deraz N M *et al;* 2012]. Combustion synthesized, mixed phases of α and γ Fe_2O_3 for adsorption removal of P-chlorophenol from contaminated water was reported [Mihoc G *et al;* 2013]. Reduced graphene oxide incorporated porous iron oxide, synthesized by combustion method was reported as an efficient anode material for Li-ion batteries [Bhuvaneswari S *et al;* 2014].

Iron oxide and carbonaceous materials incorporated iron oxide nanoparticles show good electrical properties. Few reports are available

about the electrical properties of these materials. Mesoporous α-Fe_2O_3 thick films showed stable electrical properties which were suitable for the gas sensing applications [Mirzaei A *et al;* 2016]. Zn doped hematite showed increased electrical conductivities and dielectric constants with respect to Zn content [Nikolic M V *et al;* 2012]. Activated carbon incorporated metal oxide composites showed lowering of electrical conductivity than pure metal oxide [Bogeat A B *et al;* 2014]. In 2015, the temperature dependence of electrical properties of metal oxide/activated carbon composites were also studied by the same group [Bogeat A B *et al*; 2015]. Thermal conductivity of ferromagnetic iron oxide was found to be increasing with graphene and graphite fillers [Ramirez S *et al;* 2017].

1.9 Motivation of the thesis and statement of research problem

Eco friendly non-toxic ferromagnetic iron oxide is useful for magnetic recording, medical fields and also for water treatments. Studies on shape and size controlled iron oxide nanoparticles got great attention due its technological applications. Ferromagnetic iron oxide with different morphology can be synthesized by solvothermal and hydrothermal synthesis methods. The motivation behind the present research work is focussed on the synthesis of iron oxide with large coercivity. And also the synthesis of hematite (α-Fe_2O_3) nano and microstructures by modifying the solvothermal reaction conditions. Apart from that, ferromagnetic α/γ-Fe_2O_3 nanoparticles show good heavy metal ion adsorption removal capacity from contaminated water. Adsorption is one of the efficient, simplest and cost effective methods to remove the heavy metal ions from contaminated water. Different types of adsorbents are used for this purpose, but iron oxide is a

non-toxic and efficient adsorbent, which shows ferromagnetic property. The magnetic property of the iron oxide ensures the easy separation of metal ion adsorbed iron oxide after treatment. The synthesis of ferromagnetic of α/γ-Fe_2O_3 can be achieved by optimising the growth parameter of combustion method, which is a cost effective method. The study on heavy metal ions (Ni(II)) removal with ferromagnetic of α/γ-Fe_2O_3 from contaminated water is highly motivated. The incorporation of non-toxic carbon is reported to be improving the adsorption property of the iron oxide. So the synthesis of iron oxide in graphitic matrix and its conducting and adsorption studies are also scientifically relevant.

1.10. Objectives of the thesis

The brief objectives of the present work are given below:-

- To optimize the reaction condition for the synthesis of hematite (α-Fe_2O_3) spheroid, pseudo cubic microstructures by solvothermal reaction.
- To synthesize relatively oxygen free hematite (α-Fe_2O_3) nanoparticles using acetonitrile as precursor solvent in solvothermal method.
- To synthesis α/γ-Fe_2O_3 nanoparticles using solution combustion method by varying oxidizer to fuel ratio.
- To investigate the structural, optical band gap, *dc* conductivity and magnetic properties of α-Fe_2O_3 and α/γ-Fe_2O_3.
- To study the Ni(II) ion adsorption removal properties of ferromagnetic α/γ-Fe_2O_3.
- To synthesis hematite/graphene oxide nanocomposite by solvothermal method and study its magnetic properties.
- To improve the magnetic and adsorption properties of iron oxide by incorporating iron oxide in graphitic matrix.

Chapter 2

Synthesis methods and characterization tools

Contents

2.1. Introduction

Nanomaterials exhibit shape and size dependent physical properties and these parameters of the materials can be tuned by adopting suitable synthesis strategies. Several methods such as chemical precipitation, sol-gel synthesis, solvo/hydrothermal synthesis, combustion synthesis, ball milling etc. are employed for the synthesis of nanoparticles. Solvo/hydrothermal is an efficient method for the controlled synthesis of nanoparticles with different shape and size. Solution combustion method is a cost effective technique for the synthesis of nanoparticles in large scale. This chapter discusses the details about solvo/hydrothermal and combustion synthesis of nano and microstructured particles. This chapter also describes the fundamentals of various characterisation techniques included in the present thesis. The analytical techniques used for the present investigation are mainly, X-Ray Diffraction (XRD), Fourier Transform Infra Red (FTIR) spectroscopy, Raman spectroscopy, Scanning Electron Microscopy (SEM),

Transmission Electron Microscopy (TEM), Energy Dispersive Analysis of X-Ray (EDAX), Selected Area Electron Diffraction (SAED), UV-Visible spectrophotometry, *dc* conductivity analyser, Brunauer-Emmett-Teller (BET) surface area analyser, Vibrating Sample Magnetometer (VSM) and Superconducting Quantum Interference Device (SQUID) magnetometer.

2.2. Hydrothermal Synthesis

Hydrothermal synthesis is an important method for the synthesis of nano, micro structures and hybrid nano composites. Hydrothermal reaction is bottom-up solution growth process, in which heterogeneous reaction take place between reactants, in the presence of water under autogenous pressure and temperature [Byrappa K *et al*; 2007]. Hydrothermal synthesis gives different nano and microstructures with high purity. In hydrothermal synthesis, solute is dissolved at high temperature and pressure; even though it is insoluble in room temperature and pressure. This method enables the synthesis of various metal oxides, metal sulphides, silicates etc. In hydrothermal synthesis method, crystal growth depends on reaction temperature, pressure, molarity of solution, pH of the solution and reaction time. Usually hydrothermal syntheses is carried out at relatively low temperature below 300 ^{0}C. For the hydrothermal synthesis a vessel made of stainless steel, which can withstand high pressure and temperature is required. Usually an autoclave with Teflon lined beaker is commonly used for the hydrothermal synthesis.

Since Teflon is a non-reactive material to chemicals, which can withstand temperature mostly below 400 ^{0}C only, and therefore pressure is generated inside the system. Another material used instead of Teflon beaker

is quartz, which can withstand higher temperature and pressure than Teflon. In hydrothermal synthesis, reaction rate is 1000 times more than normal condition [Hayashi H *et al*; 2010]. Hydrothermal growth provides maximum yield of the product from the initial reactants. High purity, homogeneity, crystal symmetry and naro particles size distributions etc are the major attractions of the hydrothermal techniques.

2.2.1. Solvothermal synthesis

Solvothemal synthesis is identical to hydrothermal synthesis, in this case, different types of solvents are used instead of water in the reaction medium. Nature of the solvent influences reaction condition, it will also contribute to determine the morphology of the as grown crystals. In addition to the chemical nature of the solvent, reaction time, pressure, molarity of solution, temperature viscosity, pH and density of solvent etc. also play important role in the crystal growth process. By varying the solvent used for the preparation of precursors, the particle size and shape of synthesized material can be varied. The reaction rate, oriental attachment and aggregation of the crystallites etc. depend on pH and viscosity of solvents used. Solvent with high pH and viscosity provide more oriental attachment and aggregation of smaller particles and consequently the growth of large crystals occurs.

2.3. Hydro/Solvothermal apparatus

Hydrotehrmal apparatus consists of oven, Teflon lined beaker, autoclave etc. Hydro/Solvothermal oven is a normal oven, which supplies temperature for the heating process in the hydrothermal reaction (Figure 2.1). The heating of the oven is carried out with the help of

electrical heater. The heating coil produces heat, when current is passing through the coil. The temperature of the oven can be controlled with PID (proportional integral derivative) control system by setting desired reaction temperature. By setting different temperature in PID control, the reaction temperature and temperature related pressure can be varied.

Figure 2.1.*Oven used for the solvothermal synthesis of samples under study.*

2.3.1. Autoclave

The vessel used for hydrothermal synthesis is an autoclave and the preferred material is corrosion resistant one (Figure 2.2a). An ideal auto clave should be inert to acids, bases, oxidizing agents, chemicals, solvents etc. even in high temperature and pressure. Auto clave must withstand high temperature and pressure, because reactions take place at high temperature and pressure. Auto clave should have enough volume to carry the reactants. The autoclaves are properly sealed with nuts and bolts, since it can be assembled and reassembled easily. The materials used for the synthesis of autoclave are stainless steel, nickel, iron, super alloy etc.

Figure 2.2. *(a) Auto clave (B) Teflon lined beaker used for the solvothermal synthesis of samples under study.*

2.3.2. Teflon lined beakers

In hydro/solvothermal synthesis, initial reactants can be taken in Teflon lined beakers or quarts beaker or in a glass beaker, since a chemically resistant material is needed to carry out the reaction, in most cases Teflon lined beakers are used for the conduction of reaction (Figure 2.2b). Teflon is inert to reactants, expands on heating and contract on cooling which make it suitable for hydro/solvothermal reactions. Teflon can withstand temperature up to 300 ^{0}C, so it is used in hydro/solvothermal reaction with reaction temperature up to 300 ^{0}C. In the case of high temperature synthesis of nanomaterials above 300 ^{0}C, quarts vessels are used.

2.4. Combustion synthesis

Combustion synthesis is an important technique used for the synthesis of a wide variety of nano materials. Combustion synthesis is a heterogeneous reaction between different oxidizer and fuels. Metal nitrates are commonly used as oxidizer in majority of the cases. Citric acid, glycine, etc. are used as fuel in this type of synthesis. Usually solutions of reactants

are taken inside a beaker, in order to carry out the combustions. The temperature for the combustion process is provided by heater, which is heated by means of a heating coil (Figure 2.3). The combustion reactions are usually done inside a fume hood in order to remove the outgas during reaction. On the basis of ignition, combustion synthesis process can be divided in to self propagating high temperature synthesis (SHS) and volumetric combustion synthesis [Varma A *e*t *al*; 2016].

In SHS the reactants are ignited at one end which will propagate to all ends. Once it is initiated, the reaction is self-sustainable until the completion of the reaction. In volumetric combustion process, the whole end is heated uniformly to the ignition temperature for simultaneous uniform reaction.

The nature of oxidizer, fuel, oxidizer to fuel ratio, decomposition temperature of oxidizer and fuel, pH of precursor solution etc. are the factors which affect the synthesis process. Usually the best combustion reaction occurring at a particular temperature is known as the combustion temperature. This temperature can be theoretically calculated and predicted by analyzing enthalpy of formation and heat capacity data.

In the present study α/γ-Fe_2O_3 and α/γ-Fe_2O_3/graphite nano composites were synthesized by self-sustainable high temperature combustion reaction (SHS) method.

Figure 2.3.*Heater used for the combustion synthesis of samples under study.*

2.5. Characterization Tools

2.5.1. X-Ray Diffraction

X-ray diffraction is one of the most important techniques used for the structure determination of crystalline materials. When an X-ray beam passes through a material, there is a possibility to occur the diffraction phenomenon, when the interplanar spacing of the crystalline material is comparable with the wavelength of X-ray. Under this condition, the diffracted waves obeys Braggs law, which is $n\lambda = 2d\sin\theta$. Where d is inter planar spacing, λ is the wavelength of X-ray and θ is the Braggs angle [Kittel C *et al*; 1996].

Lattice parameter of a crystal can be calculated from (hkl) values and interplanar distance [Pramanick A *et al*; 2004].

For cubic system $\frac{1}{d^2} = \frac{h^2+k^2+l^2}{a^2}$

Hexagonal system $\frac{1}{d^2} = \frac{4}{3}\left[\frac{h^2+hk+k^2}{a^2}\right] + \frac{l^2}{c^2}$

Where ‘a’ and ‘c’ are the lattice parameters. Each crystalline material has unique diffraction pattern, which is solely related to the crystalline arrangements of the material. Single crystalline X-ray diffraction can be used to determine the structure of materials in single crystalline form. The crystalline structure can be explored by using software. Powder diffraction technique is used in the case of powdered materials. The diffraction pattern obtained from the X-ray diffractometer will be compared with that of the standard data. This standard data is maintained by Joint Committee for Powder Diffraction (JCPDS).

A typical X-ray diffractometer consists of X-ray source, in most cases Cu is used as target material for the production of X-ray beam. Highly energetic electron beams falling on the surface of the target material produce X-rays. These spectra will consist of different wavelengths, with the characteristics of target materials. Monochromatic radiations from the X-ray source is separated by using suitable filters. Cuk_{α} radiation with wavelength of 1.540 Å is the commonly used X-ray wavelength in XRD studies. The wavelength of X-ray is based on the properties of target materials. Molybdenum and copper are used as other important target materials.

For the present study Rigaku D-Max and PANALYTICAL diffractometer with Cuk_{α} (λ= 1.540 Å) were used (Figure 2.4).

Figure 2.4. *Rigaku Geigerflex D Max diffractometer with CuKα radiation (λ=1.5414 Å) used for the analysis of some of the samples under study.*

2.5.2 Fourier Transform Infra Red (FTIR) spectroscopy

Fourier Transform Infra-Red (FTIR) spectroscopy is used to analyze the functional groups present in the sample. When a beam of IR radiation interacts with that of inherent molecular vibration of the sample, the molecule gives IR spectra. Basically, there exist three region exist in the electro-magnetic spectrum corresponds to molecular vibrations. From 50-400 cm $^{-1}$ is far IR region; there is a feeble chance for the occurrence of vibration motion of the molecules in this region. 400-4000 cm^{-1} region is termed as mid IR region; majority of the organic and inorganic molecules will show the spectrum in this region. 4000-15000 cm^{-1} gives near IR region, this region is basically rich with overtones and combination bands [Banwell C N *et al*; 1994, Ingle J D *et al*; 1998].

KBr pellet technique is mainly used for obtaining IR spectrum in the mid IR region. Poly ethylene method is sued to recover the IR spectra in the

far IR region. Now a day's ATR (Attenuated Total Reflection) method is also used for recording IR spectra in mid IR range.

Figure 2.5. *Shimadzu IR Affinity-1 FTIR spectrophotometer used to analyze the samples under study.*

Fourier transform technique is used in modern IR spectrometers. In FTIR spectrometer all the data will be collected simultaneously, these data will be analyzed with the aid of computer. Typical IR spectrometer has following components, IR source (ceramic light source), sample compartment and detector (high sensitivity DLATGS detector). In the present study IR affinity 1-84005 spectrometer was used (Figure 2.5).

2.5.3. Raman spectroscopy

Raman spectroscopy is basically a non-destructive vibrational spectroscopy technique. Raman spectroscopy is working on the basis of Raman effect discovered by sir C.V Raman in 1928 [Raman C V *et al*; 1928]. When a beam of electromagnetic radiation interacts with sample, it causes inelastic scattering. The scattered radiations also consist of higher and lower energy with respect to that of the incident radiation. These higher energy beams are named as anti stoke Raman line and lower energy beams are known as stoke Raman lines [Laserna J; 2001]. Raman spectroscopy is a versatile technique. A molecule will give Raman spectrum only if its

polarisability change as a result of interaction with that of radiation. It is a complimentary technique to IR spectroscopy. Raman spectroscopy is particularly useful for the analysis of amorphous materials, since other techniques are not satisfactory. Especially this is a good technique for the analysis of sample containing carbonaceous materials.

Raman spectrometer is a simple experimental technique, in which beam of monochromatic radiation is allowed to fall on the sample. This electromagnetic radiation is focused by means of lens system. Scattered radiation will be collected and detected. FT Raman spectrometer is also available, in which data is extracted by using Fourier transform techniques. Raman spectrometer is used to analyze all types of samples such as solid, liquids and gaseous samples. Raman spectroscopy technique is very useful for the identification of different phases present in the material. Usually Raman spectra of the sample are recorded in the region of 50-4000 cm^{-1}. Laser source is used for the excitation of samples. Nd: YAG (1064 nm) laser is used for the recording of Raman spectra of highly fluorescent samples [Willard H H; 1987].

Figure 2.6.*Horiba Jobin Yvon Lab RAM HR system used to record the Raman spectra of samples under study.*

In the present study Horiba JobinYvon Lab RAM HR system with excitation laser of wavelength 632.8 nm was used (Figure 2.6).

2.5.4. Scanning electron microscopy (SEM)

Scanning electron microscopy (SEM) is used to analyze the morphology of samples. When an electron beam interacts with the sample surface, secondary and back scattered electrons will produce secondary electrons which will give the information about the morphology of the sample [Watt M; 1997].

Figure 2.7.*Carl Zeiss Sigma FE-SEM used to record SEM images of some of the sample under study.*

A scanning electron microscope consists of a sample chamber which is maintained at ultra-high vacuum condition. Electron beams produced from the electron gun attached with the equipment is focused and accelerated by means of electromagnetic lenses. There is a scanning coil which scans through the sample. Secondary and back scattered electrons coming from the sample is collected and analyzed. Back scattered electron from the sample gives the composition of samples, secondary electron give images similar to photon gives photograph. In order to measure SEM of a

sample, the sample should be conductive. A non-conductive sample is made to conducting by pasting carbon tape on the sample. Coating of sample with gold palladium also helps to make sample conductive.

Now a days, field emission scanning electron microscope (FE-SEM) is widely used for imaging technique (Figure 2.7). In FE-SEM, for the production of electron beam field emitting system are used. So the image obtained with this type of instrument is having more resolution than that of ordinary SEM.

2.5.5. Energy dispersive analysis of X-ray (EDAX)

Energy dispersive analysis of X-ray (EDAX) is a method used to identify the elemental composition in a sample. In EDAX when high energy electrons bombarded on an element of sample, inner electrons get knocked out. These vacancies are then occupied by electron transferred from outer shell. The process will cause the generation of the characteristics X-ray. These X-ray beams are identified and analyzed. This gives the information about the elemental composition of materials.

EDAX can be used to analyze almost all the elements in the periodic tables except that of light elements like Hydrogen and Helium. The material quantification can also be done with EDAX micro analysis. Usually EDAX gives information about the local area on which electron beam impinge joining the surface of the sample rather than the total percentage in the sample. EDAX is usually attached with scanning electron microscope [Flewitt PE J *et al*; 2003, Schroder D K; 1998].

2.5.6. Transmission electron microscopy (TEM)

Transmission electron microscopy (TEM) is a technique used to identify the 3-D images of a sample. It is widely used for the exact size determination of nanoparticles. In transmission electron microscopy, electron beam is used for imaging of the samples. When a beam of electron interact with the matter, a portion of the beam is likely to pass through the sample specimen which will help to get the images of the sample. The working principle of transmission electron microscopy is almost identical to that of scanning electron microscopy. An electron gun is one of the important components of transmission electron microscopy, which produces electron beam. This beam can be focused and accelerated with the aid of electromagnetic lenses attached with the system. The transmitted beam will give the image of the sample and can be viewed through the detector attached with the system [Watt M; 1997].

There are two mode of transmission, one is bright field and the other is dark field. Beams directly passing through the sample usually give a bright field image. A portion of electron beam undergoes diffraction process which gives the dark field image. Bright field and dark field images can be selected from the machine by using suitable apertures. Some of the TEM machines are also attached with electron diffraction system [Hew G P, 2011]. In the present study JEOL/JEM 2100 transmission electron microscope was used.

2.5.7. UV-Visible-NIR spectrophotometry

UV- Visible-NIR spectrophotometer is an important technique used to measure the band gap of semiconducting materials [Torrent I *et al*;

2008]. In this technique, a given wavelength is allowed to pass through the sample. When the incident radiation interacts with the sample, some of the radiation get absorbed, and the remaining is transmitted or reflected. In UV-visible spectrometer transmitted light is mainly analyzed. The relative transmission of different wavelength photons which interact with samples were monitored. The photons with energies greater than band gap energy gets absorbed, photon with energy less than band gap are transmitted. Based on this, band gap of a material can be measured.

The absorption coefficient can be determined from absorption or transmission spectrum using Beer-Lambert law.

$$I = I_0 e^{(-\alpha)t}$$

'I" is the transmitted intensity, I_0 is the incident intensity, t is the thickness of the sample. α is absorption coefficient. From the plot of hν Vs $(\alpha h\nu)^2$, band gap energy of sample can be calculated.

2.5.8. Diffused reflectance spectroscopy (DRS)

Diffused reflectance spectroscopy (DRS) usually measure reflection from powder samples. There are two types of reflectance one is specular reflectance and other is diffused reflectance. Specular reflection is generated from the surface of the sample. Diffused reflectance is generated as a result of multiple reflection and scattering of penetrated radiation. The absorption coefficient is obtained by using Kubelka-Munk function [Kubelka P *et al*; 1931]. This model tells that the intensity of the reflected beam depends on the coefficient (k) and scattering coefficient (s).

Figure 2.8. *JASCO V 570 spectrophotometer used for the analysis of samples under study*

The KubelkaMunk function is $\log\left[\frac{(1-r)^2}{2r}\right]$= log k- log s

Where $r = \frac{R\ (sample)}{R\ (standard)}$

$BaSO_4$ is usually used as the standard material for the base line setting in this measurement, which has almost cent percentage reflection. KubelkaMunk can be simplified.

$$\frac{(1-R)^2}{2R} = \frac{k}{s}$$

A graph is drawn between $\left(\left(\frac{k}{s}\right)h\nu\right)^2$ Vs. hν. The band gap is obtained by extra polating straight line portion of the graph to a point at which $(\alpha h\nu)^2$ is zero. For the present study JASCO V 570 spectrophotometer was used (Figure 2.8).

2.5.9. Brunauer-Emmett-Teller (BET) analysis.

Brunauer-Emmett-Teller (BET) analysis is used for the measurement of surface area and pore size of the samples. BET equation is a basic

mathematical expression, which connects the volume adsorbed (V_a) and relative pressure (P/P_0).

$$\frac{P/P_0}{V_a\,(1-\frac{P}{P_0})} = \frac{1}{VC} + \left(\frac{P}{P_0}\right)\frac{(C-1)}{V_m C}$$

In which V_m is the monolayer volume, c is the BET constant. A graph which represents relative pressure (P/P_0) with volume adsorbed (V_a) gives slopeC_1/V_mC and y intercept which is $1/V_mC$. The surface area of 1 gm of solid can be represented with the following expression, when the volume of gas is reduced to S.T.P [Walker P L *et al*; 1968].

$$A = V_m/(22414x\ a_m N_{AV} \times 10^{-20})\ c^2/g$$

a_m is the average area occupied by the molecule ($Å^2$/molecular unit). Usually the volume of the adsorbed molecule on the surface of the particle is measured at the boiling point of nitrogen (-196^0C). Since nitrogen is used as adsorbate gas. Quatachrome instrument version 3 was used for the present study.

2.5.10. Inductive coupled plasma-atomic emission spectroscopy (ICP-AES)

Inductive coupled plasma-atomic emission spectroscopy (ICP-AES) is a technique used to identify the elemental content and trace of metals in a material. In ICP-AES, usually aqueous solution is converted in to aerosol by using plasma torch. A commonly used plasma source is inductively coupled plasma (ICP) invented by Fassal and co-workers in 1976 [Fassel V A *et al*; 1976]. This detects the emission spectra of ions in aerosol. The emission of each element is unique, so as to enable us to identify the

particular element which is present in the sample. The intensity of emission gives the information about the quantity of element present in the sample.

Basically ICP-AES consist of three quarters tubes, which are surrounded by inductive coil attached to a radio frequency generator. The high voltage of about 1.3 KW is applied, which produces magnetic field around the coil. A Tesla torch is used to convert the aqueous solution to aerosol. During this process, heating (temperature 8000-10,000 ^{0}C) will happen. So the system is cooled by argon gas pumped into it. The emission produced by different ions is separated by using grating system. These ions are detected by a photo multiplier tube.

Inductive coupled plasma mass spectrometer (ICP-MS) is similar to the inductive coupled plasma atomic emission spectrometer (ICP-AES), in which ICP torch is used to convert the aqueous solution in to ions. These ions are separated and detected on the basis of its mass.

2.5.11. *dc* Conductivity

The *dc* conductivity measurements of pelletized samples can be done by using Keithely source meter. Here the sample is considered as a resistor. A constant voltage of 200 V is applied and corresponding current is measured. The resistance of the sample is identified using Ohm's law [Kocijanic S *et al*; 2004]. The resistivity of the sample can be estimated using equation.

$$R = \rho\frac{l}{a}$$

Where ρ is the resistivity of the sample, 'l' is length of pellet; 'a' is area of cross section of pellet.

Since the conductivity (σ) is the reciprocal of resistivity (ρ), it can be identified from the conductivity measurement. The conductivity (σ) of the sample with various temperatures from 300 to 400 K was measured using keithely source meter. From the conductivity obtained for different temperatures, Arrhenius plot is drawn. The conducting nature of the sample can be studied. For semiconducting material, its activation energy can be calculated by using slope obtained from Arrhenius plot [Laidler K; 1959].The equation used for the calculation of activation energy of sample (Ea) is given by Ea= -8.325 x slope (from Arrhenius plot).

2.5.12. Vibrating sample magnetometer (VSM)

Vibrating sample magnetometer (VSM) is a sophisticated analysis instrument which is being used for the measurement of magnetic properties of materials. This technique was originally invented by Foner S of MIT, Lincoln laboratory in the year 1955 [Foner S; 1959]. VSM works on the principles of Faraday's law of induction. The VSM apparatus basically consists of stray magnetic field, the sample compartment is in between the poles of the magnet. Magnetic domains in a magnetic material will align themselves with directions of the applied magnetic field. As a result of this, there may be the possibility to develop stray magnetic field in the sample. A magnetized sample with stray field is allowed to vibrate sinusoidal by the help of piezoelectric system. The vibration of magnetic material in a magnetic field likes to produce electric signal, which is being proportional to the magnetic strength (magnetic moment). This current is not at all related to the strength of the applied magnetic field. It is basically related to the magnetic properties of the sample under investigation. The electrical

signal, which induced a voltage is amplified by using a lock in amplifier. Resulted signal can be collected by using a computer.

In a typical VSM, applied magnetic field can be varied, it enable us to measure the magnetic moment of a material with respect to the change in the external field. In the present study Lakeshore VSM 7410 was used for the magnetic measurement.

2.5.13. Superconducting quantum ineterference device (SQUID) magneto meter

The basic principle of SQUID magnetometer is also based on Faradays law of electromagnetic induction [Gramm K *et al*; 2008]. SQUID magnetometer is mostly used for the study of materials with very week magnetic properties, especially nonmagnetic materials. In this system the changes in magnetization of the sample in a stray magnetic field produces electric signals. These signals will be detected by a highly sensitive super conducting material.

SQUID magnetometer can be operated at different temperature from 4.2 K to higher temperature. The low temperature of the system is maintained with liquid Helium. The strength of the externally applied magnetic field is in the order of Tesla. For the present study PPMS magnetometer (Quantum design) was used.

Chapter 3

Solvothermal growth of spheroid and pseudocubic hematite micro structures and its magnetic, *dc* electric properties

Contents

3.1. Introduction

Hematite (α-Fe_2O_3) is a corrosion resistive, thermodynamically stable n-type semiconducting magnetic material which is suitable for gas sensing [Gou X *et al*; 2008], water splitting [Cesar I *et al*; 2006], magnetic recording [Suzuki M *et al;* 1978] and drug delivery [Lian J *et al;* 2009] applications. Magnetic properties of hematite is size and shape dependant [Tadic M *et al;* 2011, Bercoff B P *et al;* 2010, Liu Z *et al;* 2012]. Magnetic coercivity of the order of 156 and 92 Oe are reported in star like and urchin like hematite structures respectively [Song F *et al;* 2009, Zhu L P *et al;* 2006]. Relatively higher order magnetic coercivity is reported in mesoporous hollow micro spheroid, elliptic, pomegranate, prismatic shaped one which are 2239, 4539, 4350, 5027 Oe respectively [Lian J *et al;* 2009, An Z *et al;* 2009, Tadic M *et al;* 2012, Vallina B *et al;* 2014]. Interestingly, the physical properties of these materials can be modified with the usage of templates during crystal growth process which introduces heterogeneous impurities [Zhu L P *et al;* 2006]. Solvothermal/hydrothermal growth

technique is a low cost template free method for the synthesis of hematite crystallites with different size and shape by changing growth parameters. Different solvent combination has been used by the researchers for the growth of hematite crystallites with varying morphology [An Z *et al;* 2009]. Water-ethanol solvent combination promoted the growth of high coercive spherical shaped hematite crystals [An Z *et al;* 2009]. But, snow flake shaped hematite crystals are obtained when the growth is carried out with water as solvent of precursor salts [Liang H F *et al;* 2010]. Morphology of the hematite crystals are changed with ethanol-water combination ratio [Mitra S *et al;* 2007]. Grape and dumbbell structures were prepared by using ethanol and propanol as solvent of precursor salts [Chaudhari N K *et al;* 2012]. These previous investigations indicate that the choice of solvent is an important factor for controlling size and shape of as grown crystals. Methanol is an organic solvent having relatively low viscosity but propanol is with higher viscosity. In the present chapter, we are presenting the template free solvo-hydrothermal growth of hematite crystallites, the optical and magnetic properties.

3.2. Experimental

Hematite crystals were grown by solvothermal method using methanol (H-M), methanol-water 1:1 (H-MW), propanol (H-P) and propanol-water 1:1 (H-PW) solvents or solvent combination in each experiment. $FeCl_3.6H_2O$ and NaOH salts were used as initial reactants in the molar ratio 1:3 [Chakrabarty S *et al;* 2013]. The reactants were dissolved in corresponding solvents and taken in a Teflon beaker for the reaction process. The Teflon beaker containing precursor solution (50 ml)

sealed inside an autoclave made of steel. The entire reaction set up was kept inside a furnace maintained at a temperature of 200 ^{0}C. After 8 hr of reaction at 200 ^{0}C, system is allowed to cool to room temperature naturally. The experimental reaction product was taken out from the reaction system and filtered, washed and dried in air atmosphere. The pH of the precursor solution was measured as 2.90, 2.32, 1.47 and 2.76 for H-M, H-MW, H-P and H-PW respectively.

Structural characterisation of the samples was done by X-ray diffractometer (XRD) (Rigaku D Max Diffractometer) with CuK_α radiation and Fourier transform infra-red spectrometer (FTIR) using IR Affinity-1-8400S by KBr pellet method. The morphology and elemental composition of the samples were examined using scanning electron microscope (SEM) (JEOL JSM - 6390LV) equipped with EDAX. Optical absorption and diffused reflectance of the samples were recorded using UV-Visible (Jasco V-570) spectrophotometer. For recording absorption spectra of the samples, these samples were dispersed in ethanol medium and ethanol was taken as reference. Optical band gap of the sample was determined by plotting Tauc plot ($[(k/s)h\nu]^2$ versus $h\nu$) is drawn by applying Kubelka– Munk relation in reflectance obtained from the sample (DRS). The *dc* conductivity of the pelletized samples (H-P, H-PW) were measured using Keithley model 2400 source meter automated with Lab-VIEW software. Magnetic properties of the samples were measured using a vibrating sample magnetometer (VSM) attached to a physical property measurement system (PPMS, Quantum Design).

3.3. Results and discussion

XRD patterns of samples grown with methanol, methanol-water, propanol and propanol-water match with JCPDS No. 33-0664 which corresponds to hexagonal hematite (Figure. 3.1). EDAX analysis show the presence of iron and oxygen in all the samples which is in agreement with XRD data. Lattice parameter 'a' of samples under investigation are slightly increased (Δa) and its 'c' value decreased (Δc) compared to bulk one (Table.3.1). The slight increase in dimensions of 'a' and slight reduction in dimension of 'c' is probably related to change in population of oxygen vacancies similar to that reported in SnO_2 thin films [Saji C *et al;* 2006].

Table: 3.1. *Lattice parameters of solvothermally grown hematite (α-Fe_2O_3) with Methanol, Methanol-water (1:1), Propanol and Propanol-Water (1:1).*

Sample	Lattice parameters calculated		Change in lattice Parameters	
	a (Å)	c (Å)	Δa (Å)	Δc (Å)
Bulk hematite JCPDS No. 33-0664	5.0356	13.7489	-	-
H-M	5.0486	13.7115	0.013	-0.037
H-MW	5.0445	13.7052	0.009	-0.044
H-P	5.0473	13.7440	0.012	-0.005
H-PW	5.0396	13.7451	0.004	-0.004

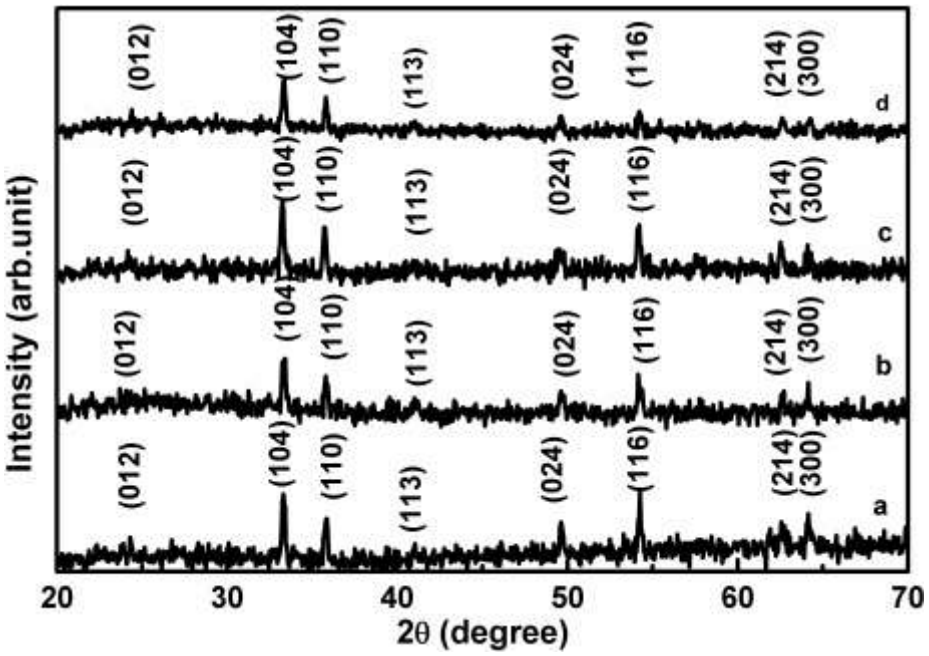

Figure. 3.1. *XRD pattern of solvothermally grown hematite (α-Fe_2O_3) with solvents (a) methanol (b) methanol-water 1:1(c) propanol and (d) propanol-water 1:1.*

Crystals grown with different solvents shows variation in crystalline size with respect to solvents used for the preparation (Figure. 3.2). Spheroid shaped crystals are obtained from precursor solution made of methanol (H-M), methanol-water (H-MW) and propanol (H-P). Average size of spheroid crystals grown with methanol (H-M) medium is 0.749 μm and that of methanol-water combination (H-MW) and propanol (H-P) are 0.285 and 0.65 μm respectively (inset of figure. 3.2). Pseudocubic crystallites with an average size of 1.281 μm are obtained when propanol-water (H-PW) combination is used for the growth process.

The pH and viscosity of the crystal growth medium has considerable effects on morphology and size of the crystals [Mitra S *et al;* 2007].

Hematite crystals grown with different solvents and solvent combination shows variations in morphology as described previously. Low pH of the mother solution for the growth of crystals generally encourages the growth of smaller crystallites [Mitra S *et al;* 2007] and higher viscous medium promote the growth of large sized particles. A combination of higher pH and viscosity of the mother solution is expected to fasten the aggregation process of smaller particles which leads to the growth of larger crystallites, along the crystalline plane (012). The pH of the crystal growth medium made of methanol is 2.9 and the aspect ratio (length/breadth) of crystals grown with this solution is about 1.21. But the addition of water in to methanol contributed to slight reduction of pH value to 2.3 and the aspect ratio of spheroid shaped sample obtained from this combination is 1.11.

The pH of the crystal growth medium made of propanol is 1.4. The aspect ratio of crystallites obtained from aforesaid solution is 1.18. But the pH of propanol-water combination is about 2.76 which is having comparatively high viscosity with respect to other solvents used in the present investigation as growth medium [Korson L *et al;* 1969, Dikio E D *et al;* 2012]. Crystals grown with this combination of growth medium posses relatively higher aspect ratio with respect to other samples under study used in the present work. This increased aspect ratio is probably originated due to the higher viscosity and relatively higher pH of the growth medium. These observations shows that, aspect ratio of the crystals grown with different solvents increases with increasing pH of the crystal growth mother solution [Liou S C *et al;* 2003]. The crystal structure (XRD pattern) of spheroid shaped samples grown with methanol, methanol-water and propanol solvents is identical to that of pseudocubic structured sample

obtained with propanol-water solvent. Diffraction peak intensity corresponds to (116) plane of P-W is found to be reduced with respect to other samples. This observation indicates that, initially formed spheroid shaped crystals undergo self-aggregation process in crystal growth medium (P-W) for minimising the morphology dependant thermodynamic energy. This self-aggregation process of spheroid crystals will lead to the formation of more stable pseudocubic crystals with less thermodynamic energy. The variation of pH and viscosity of the solvent will affect the oriented attachment or aggregation of the crystallites that may be the reason for observing spheroid and pseudocubic microstructures with different solvent combination [Chakrabarty S *et al;* 2013].

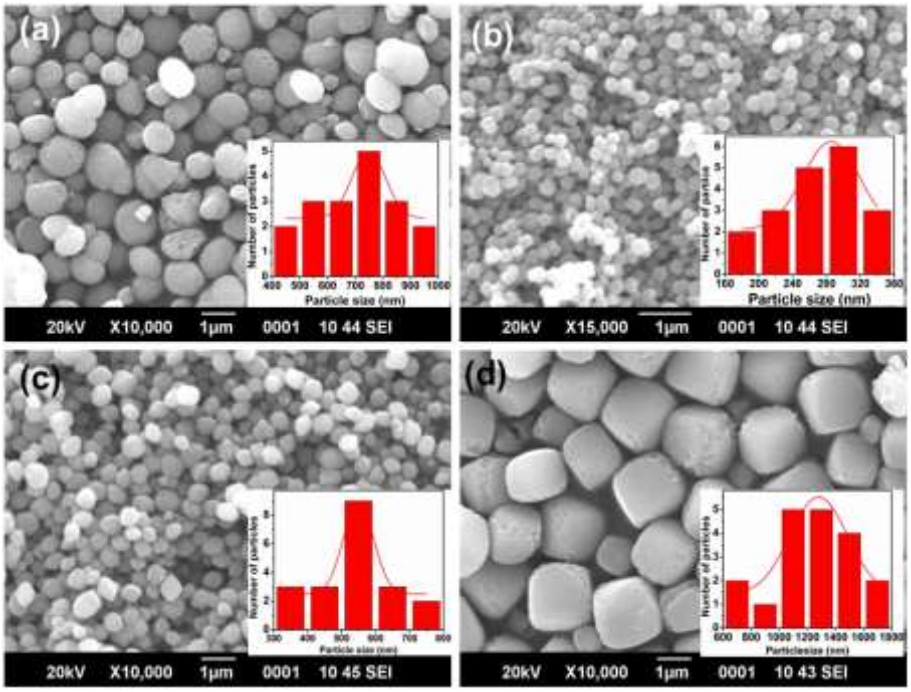

Figure. 3.2. *SEM imagages of solvothermally grown hematite (α-Fe_2O_3) with solvents (a) methanol (b) methanol-water 1:1 (c) propanol and (d) propanol-water 1:1.The inset shows particle size distribution histogram.*

The IR spectra of the samples in the range 400-2000 cm^{-1} are almost identical with a moderately intense band at 480 cm^{-1}. This observation is in agreement with our X-ray data which indicates that chemical bonding nature of all the samples are almost similar eventhough the morphogy is different. An intense IR band is seen around 565 cm^{-1} in H-MW and H-P, it is broadened in the range 533-603 (70 cm^{-1}) in H-PW and 537-599 cm^{-1} (62 cm^{-1}) in H-M (Figure. 3.3). Hematite crystal structure consists of hexagonally close packed array of O atom with Fe atoms in 2/3 of its octahedral sites. The Fe-O bond lengths are 1.945 Å to the unshared face and 2.116 Å to the shared face [Eggleston C M *et al;* 1992]. The observed IR bands are contributed to Fe-O vibration of α-Fe_2O_3 [Costa G M *et al;* 2002, Hou L *et al;* 2005], broadening of the band is probably due to the existence of Fe-O bond lengths with varying distance [Wachswan E D *et al;* 2000].

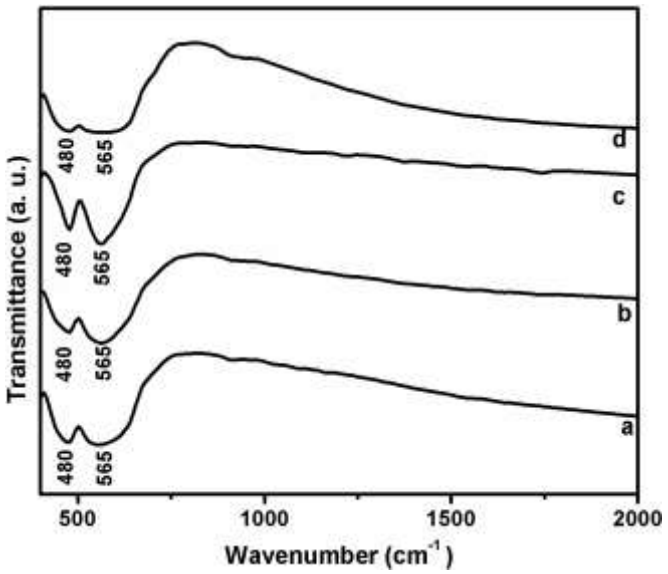

Figure. 3.3. *FTIR spectra of solvothermaly grown hematite (α-Fe_2O_3) with solvents (a) methanol (b) methanol-water 1:1(c) propanol and (d) propanol-water 1:1.*

Variation in spectral peak position and intensity are observed in the optical absorption spectra of hematite grown with different solvent combinations (Figure. 3.4). Strong absorption peaks are seen at 303 $^6A_1 \rightarrow {}^4T_1$ (^4P)) and 360 nm $^6A_1 \rightarrow {}^4E$ (^4D) and $^6A_1 \rightarrow {}^4T_2$ (^4D) from spheroid shaped sample (H-M) [Lian J *et al;* 2009, Chakrabarty S *et al;* 2013]. But the optical spectra of H-MW grown with methanol-water combination shows absorption peak at 224 nm and a broad band which extends from 350 to 700 nm with a peak centred at 568 nm, contributed to ($^6A_1$)$\rightarrow {}^4T_2$ (^4G) [Zhu L P *et al;* 2013]. The size of the sample grown with above solution combination is comparatively less, it may likely to show relatively weak light scattering, which in turn contribute to intense and broad peak at 568 nm in the absorption spectra [Lian J et. al; 2009]. Interestingly, optical absorption spectra in the UV-region is comparatively weak and are seen at 220, 257 and 285 nm from H-P prepared with propanol. However peaks are seen at 208, 250 and 273 nm from pseudocubic sample (H-PW) prepared with propanol-water combinations, related to ligand to metal charge transfer [He Y P *et al;* 2005]. Nanocrystalline hematite is a UV absorbing material, the observed variations in absorption nature of present samples are contributed to its size and shape [Lian J *et al;* 2009].

The optical absorption bands superimpose due to scattering effect of light as the size of the samples increases [Zhu L P *et al;* 2013]. Even though the size of H-M is large, the observed high intensity peak at lower wavelength region in the spheroid shaped sample grown with methanol is probably contributed to the inhomogeneous particle size of micro crystallites.

The optical band gap of H-M, H-PW is 1.87, 1.96 eV, but 2 eV in the case of both H-MW, H-P which lies within the reported values [Nguyen M T *et al;* 2014]. The change in the optical band gap of these samples may be related to variation of size and shape of the particles (Figure. 3.5).

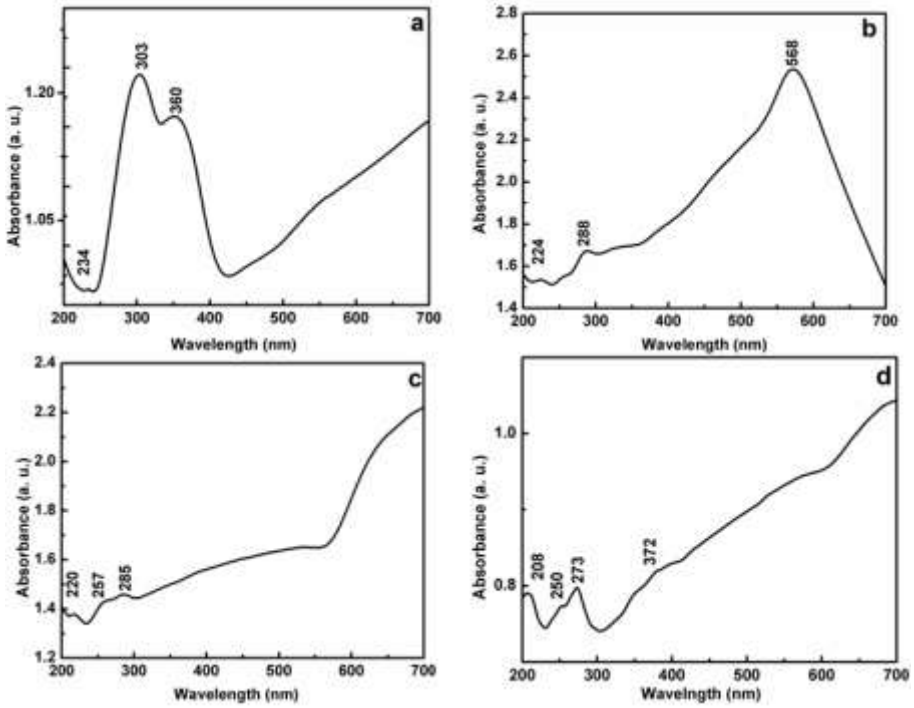

Figure. 3. 4. *Optical absorption spectra of solvothermally grown hematite (α-Fe_2O_3) with solvents (a) methanol (b) methanol-water 1:1(c) propanol and (d) propanol-water 1:1.*

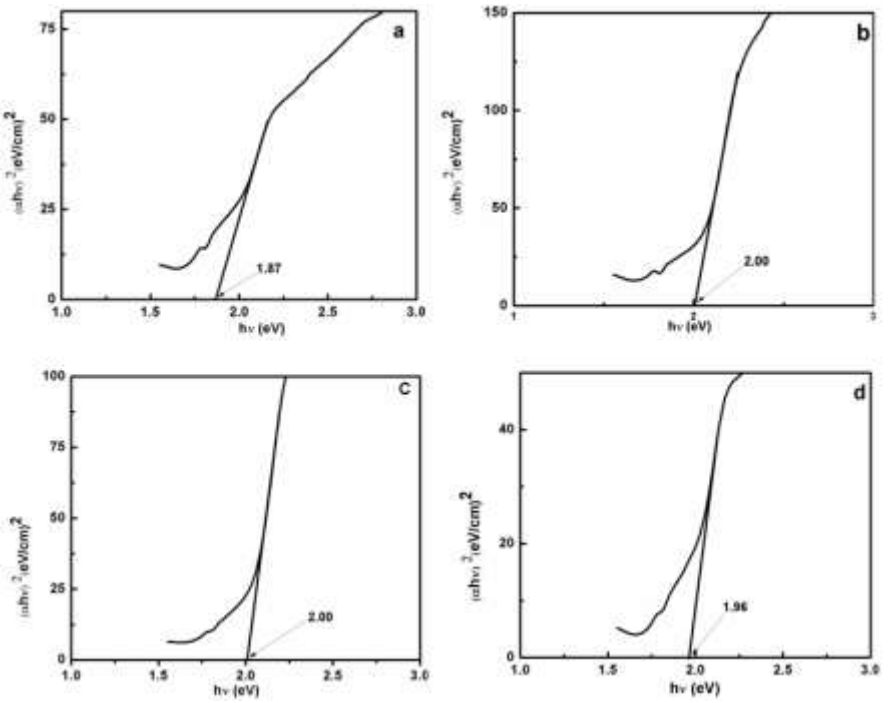

Figure. 3.5. *Tauc plots of solvothermally grown hematite (α-Fe_2O_3) with solvents (a) methanol (b) methanol-water 1:1(c) propanol and (d) propanol-water 1:1.*

The change in electrical conductivity with temperature range (300-400 K) was measured and Arrhenius plot (lnΩ Vs 1000/T) is drawn. Room temperature electrical conductivity (*dc*) of H-P and H-PW are about 3.05×10^{-7} and 5.02×10^{-8} S/cm respectively (Figure. 3.6). The *dc* electrical conductivity of samples is found to be increased with respect to temperature similar to semiconductors. The activation energy of H-P and H-PW are almost identical which shows values of 0.38 and 0.45 eV respectively and are not related to particle size and morphology.

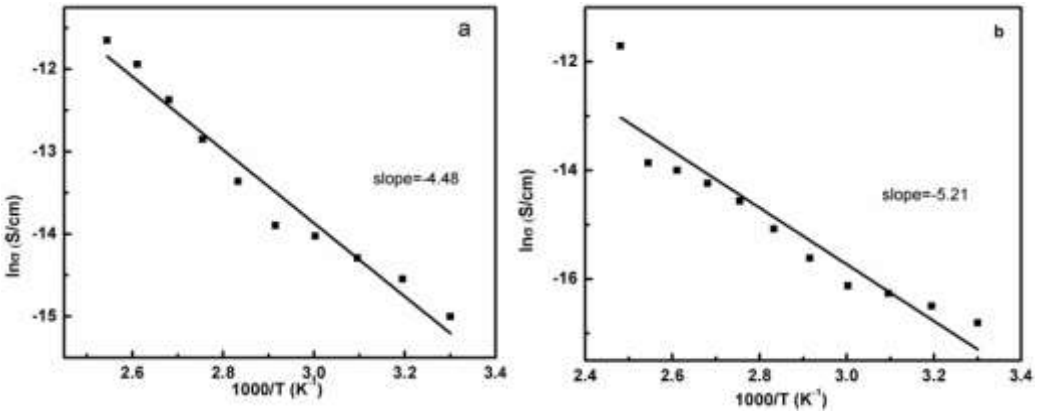

Figure. 3.6. *Arrhenius plots of solvothermally grown hematite (α-Fe_2O_3) with solvents (a) methanol and (b) propanol-water 1:1.*

The M-H curve at 300 K of sample grown using methanol shows ferromagnetic nature with coercivity of about 5.23 kOe and remanence value of 0.23 emu/g (Figure. 3.7a). For H-MW, coercivity value is 840 Oe at room temperature and has a remanence of 0.21 emu/g. The shape of magnetic hysteresis loop of sample grown with propanol and propanol-water combination is identical; however its coercivity values are 4.8 and 6.2 kOe respectively. The coercivity and remanence of all the samples at 5 K are less as compared to the room temperature (300 K) values. At 5 K, the coercivity is 58, 54, 178 and 82 Oe in H-M, H-MW, H-P and H-PW respectively and corresponding remanent value for H-M is 0.02 emu/g while it is zero in the cases of H-MW, H-P and H-PW (Table: 3.2). The appearance of hysteresis loop below Morin transition temperature at 5 K is attributed to the uncompensated spin at the surface of particles similar to one reported in plate like α-Fe_2O_3 [Tadic M *et al;* 2011]. Appearance of relatively weak loops at higher field strength side of the M-H curve probably due to the coupling between magnetic moments induced by the defects.

Usually, magnetic coercivity of the micro crystallites is expected to have comparatively low values because of its multi domain magnetic structure in which particle interaction is limited [Bercoff P G *et al*; 2010]. But in the present case, spheroid and pseudocubic micro crystallites show enhancement in coercivity, which is related to comparatively higher aspect ratio. As stated previously, the aspect ratio of spheroid like samples are estimated as 1.21 (H-M), 1.11 (H-MW), 1.18 (H-P) and that of micro pseudocubic one is 1.22. Magnetic coercivity of all samples at room temperature increases with increase of aspect ratio which is in agreement with reported previously [Lu A H *et al*; 2007]. The particle with higher aspect ratio has more shape anisotropy, which gives more coercivity. In spheroid and pseudocubic samples, there is a higher possibility of inter particle interaction and consequent alignment of particles. These inter particle interaction increases the effective anisotropy of the nanocrystals, consequently reversal of magnetisation is not easy and hence it possess high coercivity [Tadic M *et al;* 2012, Rath C *et al;* 1999, Can M M *et al*; 2011, Frandsen C *et al;* 2005]. Further solvothermally grown micro crystallites likely to have crystalline defects which is understood from the slight variation in its lattice parameters, these defects act as pinning centre that inhibit reversal of magnetisation within the core of each particle, resulting in high coercivity [Bercoff P G *et al;* 2010].

M-H curve of all samples (H-M, H-MW, H-P and H-PW) measured at 5 and 300 K (Figure. 3.8) are not saturated. The magnetic saturation (M_s) values of samples are estimated by plotting M Vs. 1/H graph [Tadic M *et al;* 2012] and are about 1.28 emu/g (300 K) and about 1.2 emu/g (5 K) for all samples. The observed non-saturation of M-H curves of the samples

measured at 300 as well as 5 K is due to the presence of residual antiferromagnetic components in the samples [Chakrabarty S *et al;* 2014].

The temperature dependant magnetisation measured with applied field of 300 Oe (FC) and zero field (ZFC) shows that the magnetisation slightly increases with temperature from 0 to ~243 K. It is interesting to note that the magnetisation of all the samples abruptly increases from a particular temperature that is Morin transition temperature (M_T). The maximum of first derivative of magnetisation with respect to temperature (dM/dT) gives Morin transition (M_T) temperature (Figure. 3.9 inset) [Chakrabarty S *et al;* 2014, Wu C *et al;* 2006, Gou X *et al;* 2013]. The M_T values of H-MW, H-P and H-PW are observed to be 232, 233 and 231 K respectively. Spheroid shaped sample (H-M) with size of 749 nm (H-M) shows two M_T values which are at 189 and 243 K. The observation of two Morin transition temperatures may be due to the inhomogeneous particle size of the sample, as understood from the optical absorption spectra which shows strong UV peak at 330 and 360 nm. The SEM images of H-M also show more variation in particle size with respect to other samples used in the present investigation (Figure. 3.2a).

ZFC and FC curves show a bifurcation above Morin transition temperature at 261, 239 and 244 K in H-M, H-MW and H-P respectively. This type of bifurcation above Morin transition temperature is not observed in micro pseudocubic samples. Hematite sample usually behaves as uniaxial antiferromagnet with spins aligned antiparallel below the Morin transition temperature, but above T_M the spins show slight canting, leading to weak ferromagnetism [Tadic M *et al;* 2012]. Spin flop Morin transition

temperature is reported at 263 K in hematite microcrystals [Morin F J*;* 1950]. The Morin transition temperature of all the samples used in the present study are observed below that of the bulk sample [Morin F J*;* 1950]. This observation indicates that sample grown with methanol, methanol-water, propanol and propanol-water combinations are micro crystallites. Shifting of Morin transition temperature compared to its bulk counterpart is attributed to variation in number of oxygen vacancies related to its crystalline lattice parameters as discussed previously [Goya G F *et al;* 2005].

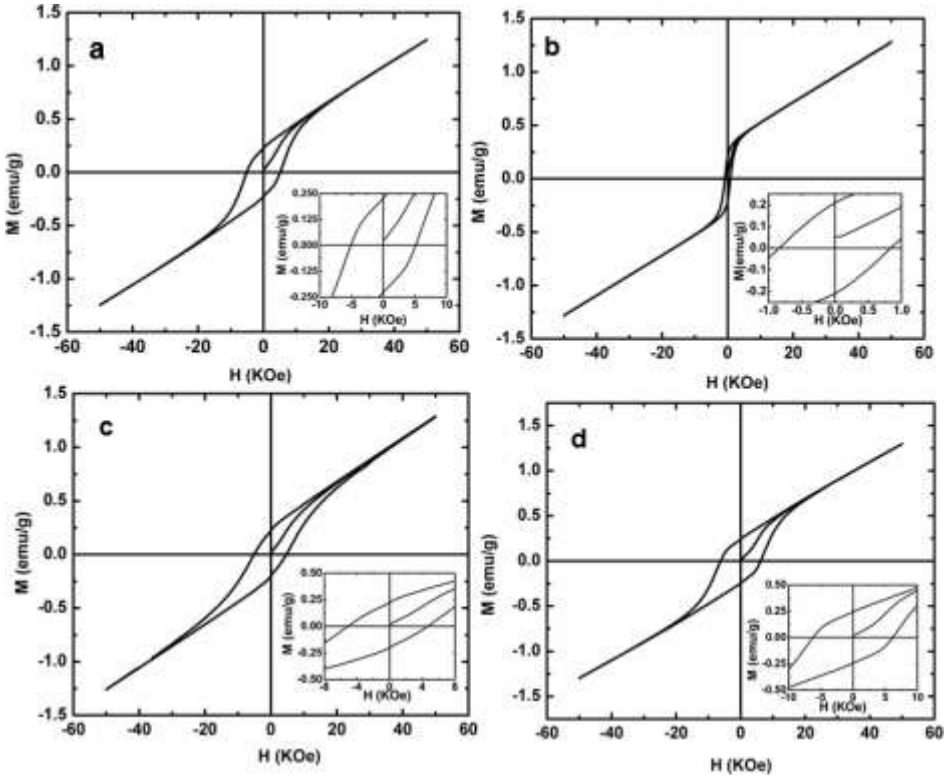

Figure. 3.7. *Magnetic hysteresis curve of solvothermally grown hematite (α- Fe_2O_3) with solvents (a) methanol (b) methanol-water 1:1(c) propanol and (d) propanol-water 1:1 at a measurement temperature of 300 K.*

In our study, we obtained coercivity value of 5.23 kOe from spheroid shaped sample which is higher than that of the reported one with similar structure [Dunlop D J *et al;* 1971, Bercoff P G *et al;* 2010]. We also obtained highest coercivity value of 6.2 kOe from micro pseudocubic structures compared with available literature data [Lian J *et al;* 2009].

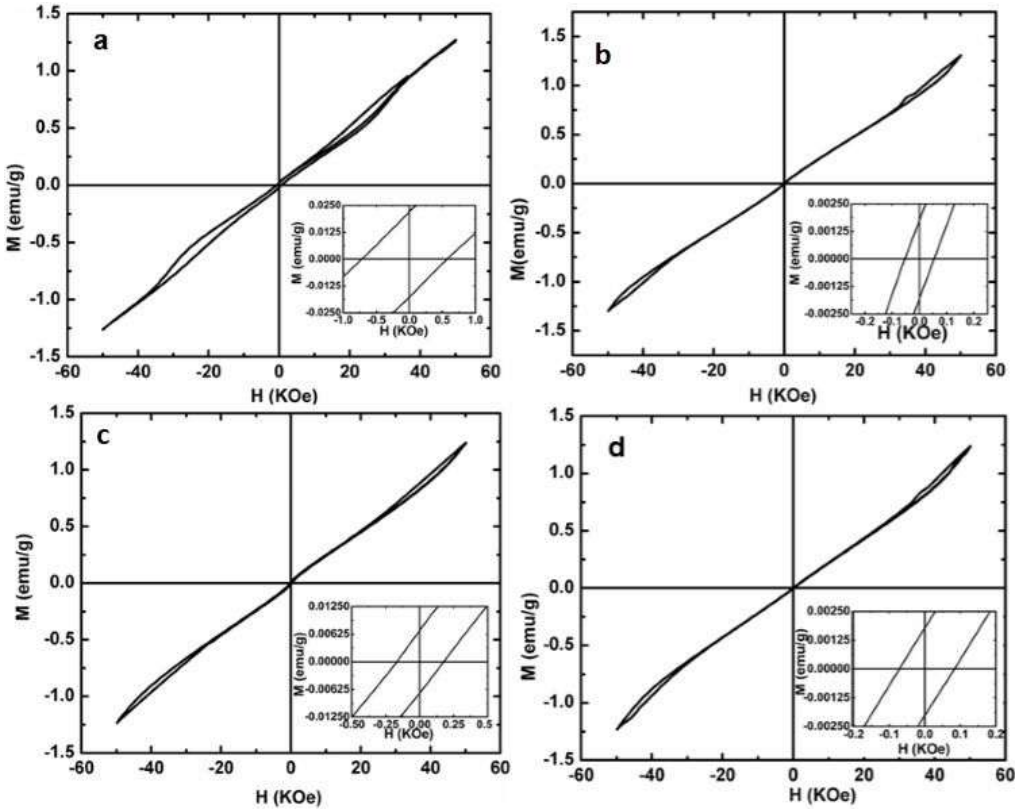

Figure. 3.8. *Magnetic hysteresis curve of solvothermally grown hematite (α-Fe_2O_3) with solvents (a) methanol (b) methanol-water 1:1(c) propanol and (d) propanol-water 1:1 at a measurement temperature of 5 K.*

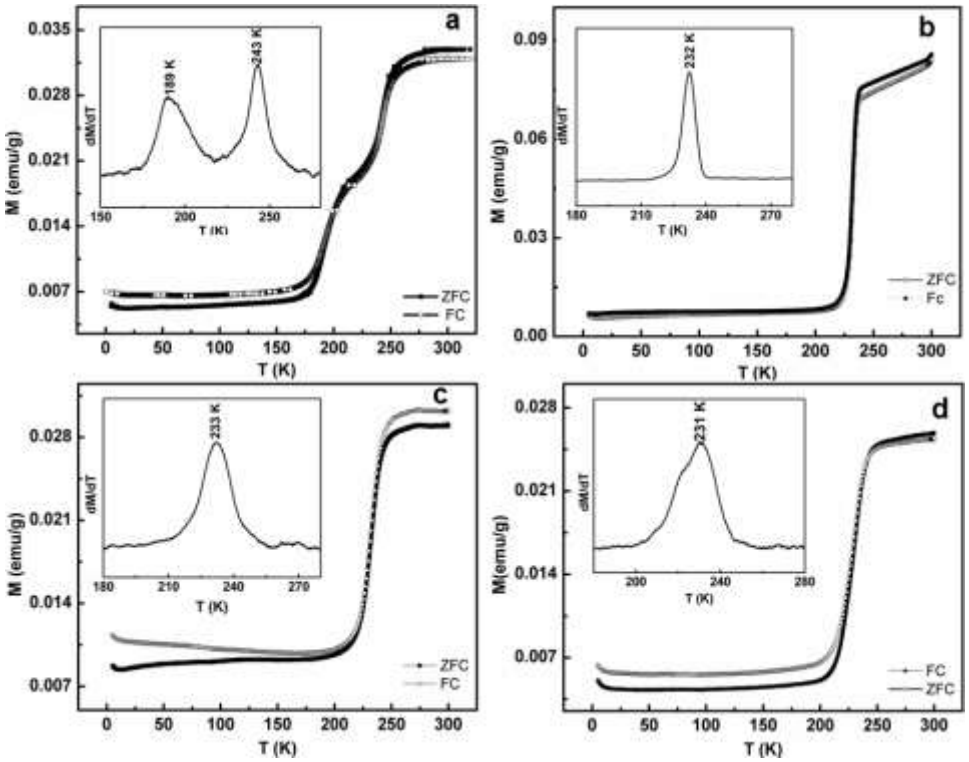

Figure. 3.9. *FC (300 Oe) and ZFC of solvothermally grown hematite (α-Fe_2O_3) with solvents (a) methanol (b) methanol-water 1:1(c) propanol and (d) propanol-water 1:1. The inset show differential curve.*

Table: 3.2. *Magnetic parameters of solvothermally grown hematite (α-Fe_2O_3) with different solvents*

Sample	**Shape**	**Average particle size form SEM (nm)**	**Aspect ratio (b/l)**	**Hc (kOe)**		**Mr (emu/g)**		**Ms (emu/g)**		**M_T (K)**
				300 K	5K	300 K	5 K	300K	5 K	
H-M	Spheriod like	l~749 b~909	1.21	5.23	0.058	0.2	0.0223	1.2	1.2	189, 243
H-MW	Spheriod like	l~256 b~285	1.11	0.84	0.054	0.2	0.0018	1.3	1.2	232
H-P	Spheriod like	l~650 b~549	1.18	4.80	0.178	0.2	0.0071	1.2	1.2	233
H-PW	Micro pseudocubes	l~1281 b~1562	1.22	6.16	0.082	0.2	0.0019	1.3	1.2	231
*l-length	*b-breadth									

3.4. Conclusions

Size, shape and crystalline defects in hematite crystals can be modified by using different solvent combination of precursor solution in solvothermal synthesis method. Variation in optical, *dc* conductivity and magnetic properties of solvothermally grown spheroid shaped hematite crystals are attributed to its size, shape and population of oxygen vacancies. Relatively higher room temperature coercivity are observed from spheroid (5.23 kOe) and micro pseudocubic crystals (6.16 kOe) grown with methanol and propanol-water combinations respectively. The enhanced room temperature magnetic coercivity observed in spheroid and pseudocubic micro crystals is contributed to shape anisotropy and defect related spin pinning effects. Spheroid sample grown with methanol shows high intensity UV absorption peaks and displays two Morin transition temperatures which may be related to inhomogeneous particle size distribution. Shifting of Morin transition temperature of the spheroid and pseudocubic hematite samples compared to its bulk counterpart is attributed to variation in number of oxygen vacancies. The morphology dependant optical and magnetic properties presented in this study provide information about the optimisation of synthesis condition of new hematite micro structures for future technological applications.

Chapter 4

Magnetic and physical properties of solvothermally prepared hematite (α-Fe_2O_3) and hematite/graphene oxide nanocomposites (α-Fe_2O_3/GO)

Contents

4.1 Introduction

Hematite (**α-Fe_2O_3**) is one of the important stable phases of iron oxide which is an n-type semiconductor [Lian J *et al*; 2009]. It shows canted antiferromagnetic behaviour (weak ferromagnetism) in the temperature range between Morin transition temperature and Neel's temperature [Lu H M *et al*; 2010]. Graphene based materials and its combination with hematite has been investigated for magnetic storage memory applications [Aigu L L *et al*; 2015], degradation of organic contaminants [Muthukrishnaraj A *et al*; 2015], for photo electro chemical capacitors [Yang S *et al*; 2015], as an anode material for lithium ion batteries [Bai S *et al*; 2012], and also for electromagnetic wave absorption [Zhang L *et al*; 2015]. It is reported that GO is exhibiting magnetic moment related to defects or the nature of binding of O- atoms with carbon etc. [Sarkar S K *et al*; 2014, Li W *et al*; 2009]. Interestingly, tunable room temperature ferromagnetic properties are exhibited by iron oxide/graphene oxide thin films prepared by spin coating

[Aigu L L *et al*; 2015]. α-Fe_2O_3/GO is also expected to give modified magnetic properties with respect to α-Fe_2O_3 and graphene oxide acts as a matrix, which can isolate the spins of α-Fe_2O_3 similar to magnetic nanoparticles embedded in amorphous carbon matrix reported previously [Host J J *et al*; 1998, Bonard J M *et al*; 2001, Nishi N *et al*; 2003, Nishi N *et al*; 2003]. Nag S *et al* reported the magnetic properties of sol-gel synthesized α-Fe_2O_3/rGO nanocomposite [Nag S *et al*; 2016]. As stated previously, magnetic properties of GO is contributed by defect induced magnetic moments and also depends on the preparation history [Prakash A *et al*; 2012]. Similarly, magnetic properties of α-Fe_2O_3 and α-Fe_2O_3/GO system might have been expected to be influenced by solvents used for the synthesis. Aigu L L *et al* reported the synthesis of α-Fe_2O_3/GO using deionised water as the solvent [Aigu L L *et al*; 2015]. Synthesis of α-Fe_2O_3 in non-aqueous oxygen free medium like acetonitrile is particularly important, since the growth process is expected to be different from crystals grown in aqueous medium [Prakash A *et al*; 2012]. Apart from that oxygen free solvents like acetonitrile may prevent the additional introduction of oxygen into the grown materials.

In the present chapter, we are reporting the synthesis and the magnetic properties of α-Fe_2O_3 and α-Fe_2O_3/GO system in oxygen free solvent acetonitrile, for the first time.

4.2. Experimental

Hematite (α-Fe_2O_3) and hematite/graphene oxide (α-Fe_2O_3/GO) composites were prepared by solvothermal method in acetonitrile solution. 0.813 mg (1 M) of iron (III) chloride (30 ml of acetonitrile) and 0.492 mg

(3 M) of sodium acetate (20 ml of acetonitrile) were used as precursor solutions. Both precursors were separately stirred for 15 minutes, after that these solutions were mixed together and allowed to stir for another 30 minutes. The resultant solution was transferred in to a 100 ml Teflon-lined stainless steel autoclave and kept over an oven at 200 ^{0}C for 6 hrs. After the completion of reaction, autoclave was allowed to cool to room temperature naturally. The obtained precipitate was cleaned several times using distilled water and filtered out. For the synthesis of hematite-graphene oxide (α-Fe_2O_3/GO) composite, 0.0813 mg of graphene oxide synthesized by Hummers method [Hummer B W S *et al*; 1958] was additionally added to the metal part of precursor (Iron (III) chloride) and the same procedure was repeated.

XRD pattern of the prepared sample was taken by using XPERT-PRO X-ray diffractometer (PANANALYTICAL) with CuK_α radiation (1.5405 Å). FTIR and Raman spectra of the samples were recorded using IR Affinity-1-8400S spectrometer (KBr pellet method) and Horiba Jobin Yvon Lab RAM HR system respectively. Morphological analyses were done with TEM (JEOL JEM 2100) and FESEM (Carl Zeiss Sigma) systems. Magnetic studies were carried out using a PPMS magnetometer (Quantum design). The details of analytical instruments like FTIR, TEM and UV-Vis NIR used for the present investigation were given in chapter 3.

4.3. Result and discussion

Iron oxide grown with acetonitrile medium showed hexagonal phase of α-Fe_2O_3 (33-0664) in its XRD pattern. Intense XRD peak observed at 2θ

value 33.10^0 corresponds to (104) plane of α-Fe_2O_3. Preferential orientation of α-Fe_2O_3/GO composite grown with acetonitrile medium was along (104) plane similar to α-Fe_2O_3. Diffraction peaks corresponds to GO were seen at 2θ value 11.2^0 (002) [Zhang B T *et al*; 2014] (Figure 4.1). Lattice parameter 'c' of α-Fe_2O_3 is estimated to be 13.8211 Å. Lattice parameter 'c' of α-Fe_2O_3 in α-Fe_2O_3/GO composite was slightly reduced to 13.5949 Å, contributed to the strain induced by the GO [Mokdad I *et al*; 2016].

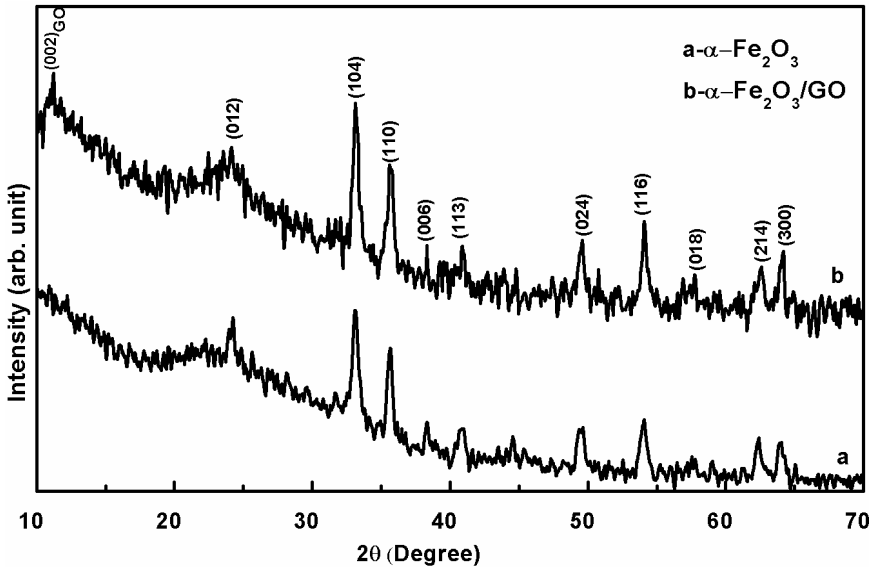

Figure. 4.1. *XRD pattern of solvothermally prepared (a) α-Fe_2O_3 (b) α-Fe_2O_3/GO composite.*

FTIR spectra of α-Fe_2O_3 showed bands at 465 and 557 cm^{-1} which corresponds to Fe-O vibrations (Figure 4.2) [Costa G M D *et al*; 2002, Huo L *et al*; 2005]. The band at 557 cm^{-1} was slightly shifted towards lower wave number in α-Fe_2O_3/GO and appeared at 550 cm^{-1}. Additional weak bands at 940, 1630 and 3365 cm^{-1} are corresponds to C-H stretching, C=C and O-H stretching vibrations [Xu C *et al*; 2016, Guo S *et al*; 2013, Al-Bayati F A *et al*; 2009].

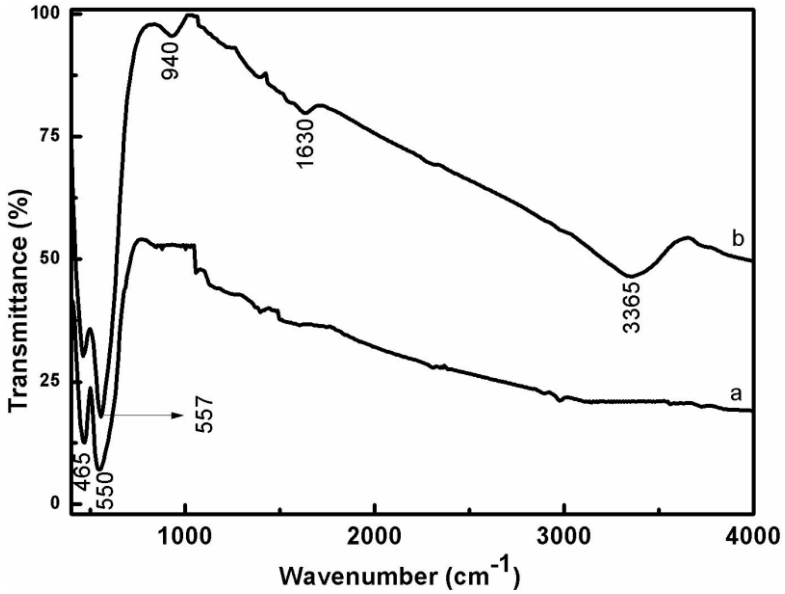

Figure. 4.2. *FTIR spectra of solvothermally prepared (a) α-Fe_2O_3 (b) α-Fe_2O_3 /GO composite.*

In the Raman spectra, defect related breathing mode of sp^2 ring was observed at 1326 cm^{-1} in both GO and α-Fe_2O_3/GO system (Figure 4.3). D band position of these compounds are shifted towards lower energy side with respect to that of GO previously reported at 1352 cm^{-1} [Sobon G *et al*; 2012, Ferrari A C *et al*; 2000]. Ratio of intensity of D band to G band of GO (1.218) and α-Fe_2O_3/GO (1.309) are almost similar and comparable to that of graphene oxide reported. This observation indicates that GO in α-Fe_2O_3/GO is relatively disordered than GO [Sobon G *et al*; 2012, Ferrari A C *et al*; 2006]. The G band (sp^2 C-atom) is observed at 1595 cm^{-1} in α-Fe_2O_3/GO which is not shifted with respect to that of Raman spectrum of GO (1592 cm^{-1}) and previously reported one [Sobon G *et al*; 2012]. Weak Raman bands seen at 228 (A_{1g}), 253 (E_g), 395 (E_g), 509 (A_{1g}) and

588 (E_g) cm^{-1} in α-Fe_2O_3/GO is corresponds to that of α-Fe_2O_3 [Rashid N M A *et al*; 2016].

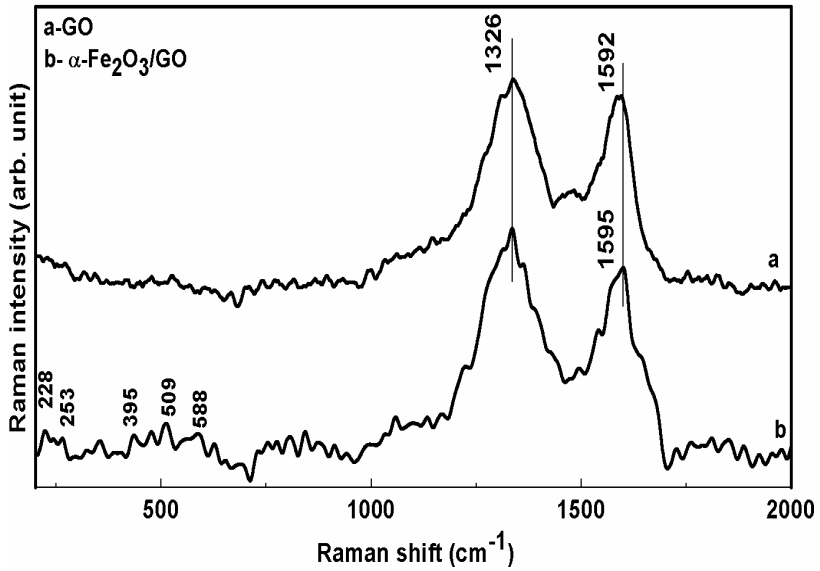

Figure. 4.3. *Raman spectra of (a) GO synthesized by Hummers method (b) solvothermally prepared α-Fe_2O_3/GO.*

Almost spherical morphology is shown by both α-Fe_2O_3 and α-Fe_2O_3/GO composite system, and its average particle size was 64 (α-Fe_2O_3) and 72 nm (α-Fe_2O_3/GO) calculated from SEM images (Figure 4.4). Transmission electron microscopy showed that α-Fe_2O_3 particles with average size of 73 nm were embedded in graphene oxide matrix (Figure 4.5a and b). HR-TEM images showed that interplanar distance was about 0.25 nm (110). SAED pattern of hematite graphene oxide system is indexed in figure 4.5e. EDAX spectra of α-Fe_2O_3/GO indicate the presence of the elements like carbon, iron and oxygen.

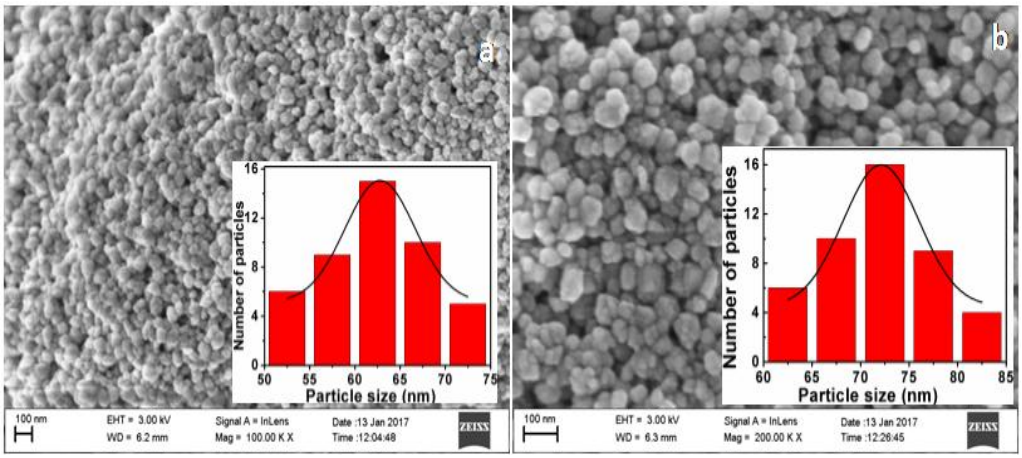

Figure. 4.4. *FE-SEM images of solvothermally prepared (a) α-Fe_2O_3 (b) α-Fe_2O_3/GO composite.*

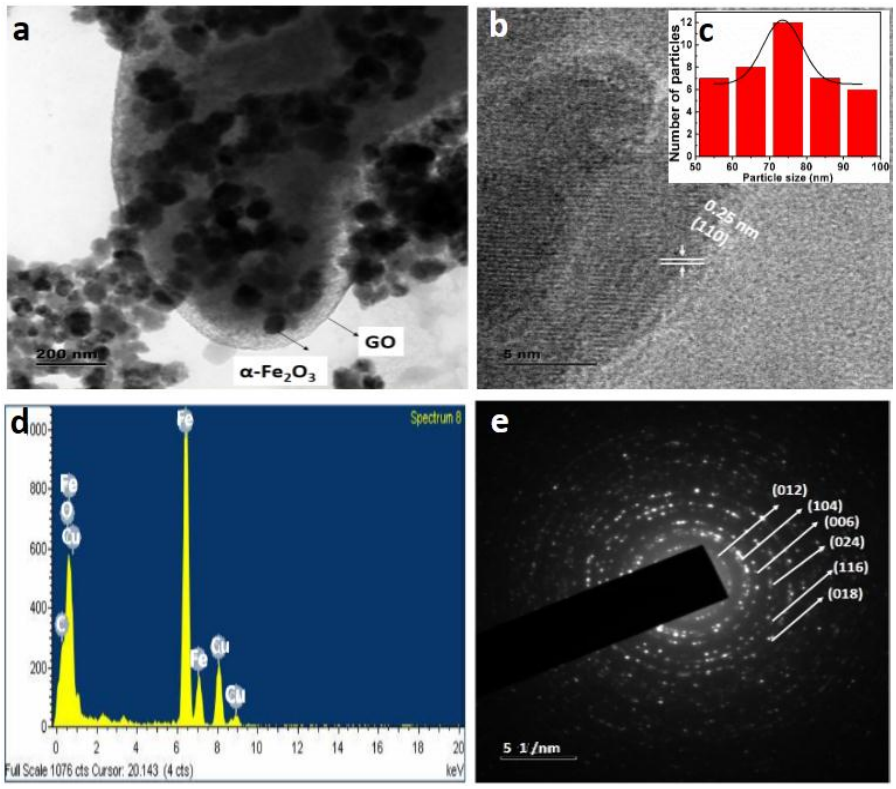

Figure. 4.5. *TEM images of solvothermally prepared α-Fe_2O_3/GO (a) Low resolution (b) HRTEM (c) Particle size distribution histogram (d) EDAX (e) SAED.*

Optical band gap of samples are estimated from Tauc plots drawn usnig Kubelka-Munk function [Kubelka P; 1948, Kubelka P *et al*; 1931]. Optical band gap of hematite is 1.8 and that of H-GO is slightly increased to 1.94 eV (Figure 4.6). These values are comparable with that of one reported for α-Fe_2O_3 previously [Nguyen M T *et al*; 2014].

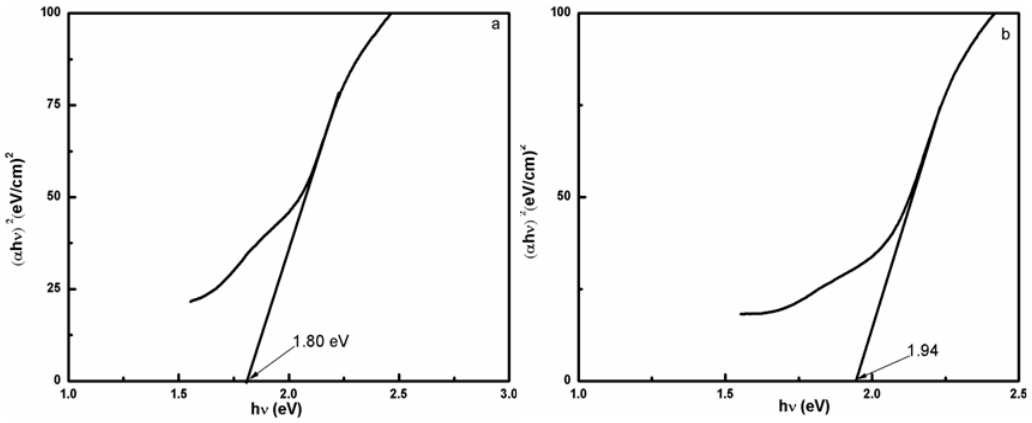

Figure. 4.6*. Tauc-plot of solvothermally prepared (a) α-Fe_2O_3 (b) α-Fe_2O_3/GO composite*

Room temperature *dc* conductivity of hematite (H) is 4.41x10^{-7} S/cm and that of hematite/GO composite (H-GO) is 7.23x10-6 S/cm. Both samples show conductivity increment with respect to temperature similar to semiconductors. Activation energy calculated from Arrhenius plot (E_a=slope x 0.8625) [Hassan A J *et al*; 2014] is 0.37 for hematite (H), and is less in (0.087 eV) graphene oxide added sample (H-GO) (Figure 4.7).

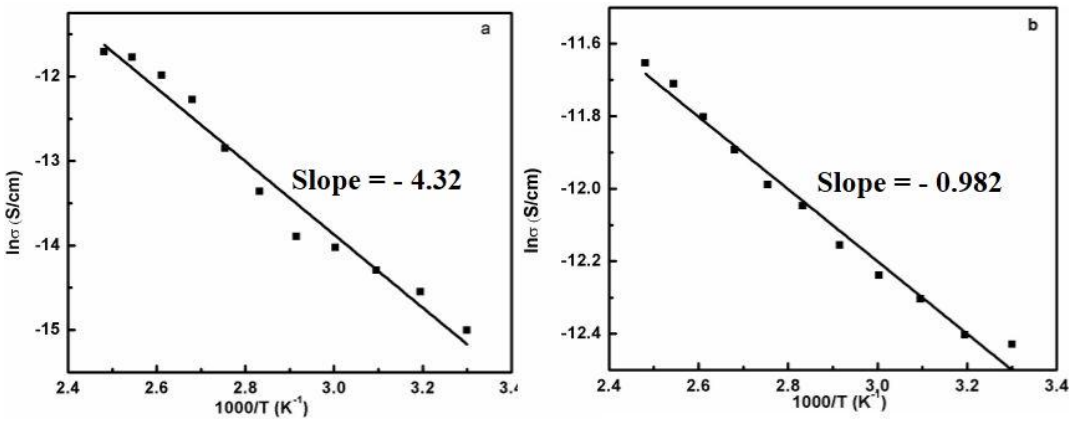

***Figure. 4.7**. Arrhenius plot of solvothermally prepared (a) α-Fe_2O_3 (b) α-Fe_2O_3/GO composite.*

The M-H curve of hematite α-Fe_2O_3 and α-Fe_2O_3/GO composites were not saturating at both room (300 K) and low temperature (5 K) (Figure 4.8 and Figure 4.9). Hysteresis loop indicates that both the samples are weakly ferromagnetic at room temperature and showed improved ferromagnetism at low temperatures (5 K). Coercivity and remanace of α-Fe_2O_3 were 76 Oe and 0.045 emu/g respectively which are slightly higher than those of hematite with size 40 nm at room temperature, reported by Lian J *et al* [Lian J et al; 2009]. Its coercivity is found to increase to 2.3 kOe and remanance increased to 0.4±0.003 emu/g at 5 K. Remanence of α-Fe_2O_3/GO is 0.06±0.0004 emu/g at 300 K, slightly higher than the value observed for α-Fe_2O_3 (0.045). Remanence (0.44±0.004 emu/g) of α-Fe_2O_3/GO was also found to increase on lowering the temperature to 5 K. In the case of non-saturating samples, magnetic saturation can be calculated by plotting the M Vs. 1/H curve [Tadic M *et al*; 2012], which gives a value of 3 emu/g at 300 K for α-Fe_2O_3, it has increased to 4.3±0.03 emu/g on lowering the temperature of the sample to 5 K. In the case of α-Fe_2O_3/GO

sample also, at room temperature, the saturation magnetization (3.2±0.04 emu/g) is increased slightly as compared to that of α-Fe_2O_3 (3±0.03 emu/g). M-H curve of GO (Synthesized by Hummers method) at 5 and 300 K were measured, in order to know the contribution of magnetic properties of GO in α-Fe_2O_3/GO system. Magnetic coercivity of GO was 70±1 and 75±1 Oe at room temperature (300 K) and 5 K respectively (Figure 4.10). Magnetic remanance of GO was 0.00114±0.0001 (300 K) and 0.0023±0.0002 at 5 K. At room temperature as well as at 5 K, GO showed weak super paramagnetic behaviour. The magnetic coercivity value of GO in the present study is different from one which is reported by Sarkar S K *et al* [Sarkar S K *et al*; 2014]. These variation are expected in materials having defect induced magnetic moments, its magnetic properties to a certain extent depends on the graphite used for the synthesis of GO and the synthesis pathway. Magnetic coercivity of GO added sample (α-Fe_2O_3/GO) is considerably increased from 88±1 Oe at room temperature to a value of about 3064±27 Oe at 5 K. As given previously, coercivity of α-Fe_2O_3 was 2335±23 Oe (Table 4.1).

The increase in the coercivity of α-Fe_2O_3/GO at low temperatures is similar to that reported in nanomagnetic particles embedded in amorphous carbon matrix [Host J J *et al*; 1998, Bonard J M *et al*; 2001, Nishi N *et al*; 2003]. Higher order magnetic field in reverse direction is required to align canted spins at low temperature which in turn gives higher value of coercivity and magnetic saturation observed in the present case [Nag S *et al*; 2016]. Indirect exchange coupling among the conducting electrons of graphene oxide and the ‘d’ electrons of α-Fe_2O_3 atoms leads to RKKY (Ruderman-Kittel-Kasuya-Yosida) interaction [Aigu L L *et al*; 2015, Nag S

et al; 2016, Ruderman M A *et al*; 1954], consequently increase in the coercivity of α-Fe_2O_3/GO.

Field cooling (FC) of α-Fe_2O_3 with an applied field of 300 Oe showed constant magnetisation up to 175 K, then it is slightly decreased on cooling up to 125 K. And thereafter on further cooling of the sample, the magnetisation is found to be constant. In zero field cooling (ZFC) condition, magnetisation of α-Fe_2O_3 showed gradual decrease on cooling. The ZFC and FC (at field strength 300 Oe) magnetisation curves of α-Fe_2O_3 coincided at around 324±1 K (blocking temperature) (Figure 4.11) [Hansen M F *et al*; 1999]. Graphene oxide added sample (α-Fe_2O_3/GO) showed similar behaviour in FC condition with an applied field of 300 Oe and ZFC curve. But its blocking temperature is slightly shifted to 348±1 K compared to that of α-Fe_2O_3 (Figure 4.12). The slight shift in blocking temperature might be due to the increase in the particle size of hematite in α-Fe_2O_3/GO composite [Chesnel K *et al*; 2014]. The Morin transition temperature of sample is calculated by plotting graph between the differential of magnetic saturation with respect to temperature Vs. temperature (dM/dT Vs. T) [Wu C *et al*; 2006]. The Morin transition temperature identified from ZFC (151±1 K) and FC (148±1 K) curves of α-Fe_2O_3 showed almost similar values. Average of Morin transition temperature under ZFC and FC of α-Fe_2O_3 was 150±1 K, which is less than that of bulk hematite (263 K) [Marcos J S *et al*; 2011]. The lowering of Morin transition temperature compared to that of bulk hematite (263 K) is attributed to its reduction in size [Ozdemir O *et al*; 2008]. α-Fe_2O_3/GO exhibits Morin transition temperatures at 139±1 K under ZFC condition and at 150±1 K under FC.

The difference in Morin transition temperature in ZFC and FC conditions (thermal hysteresis) of α-Fe_2O_3/GO is 11 K contributed to first order phase transition [Suber L *et al*; 2010, Luna C *et al*; 2012].

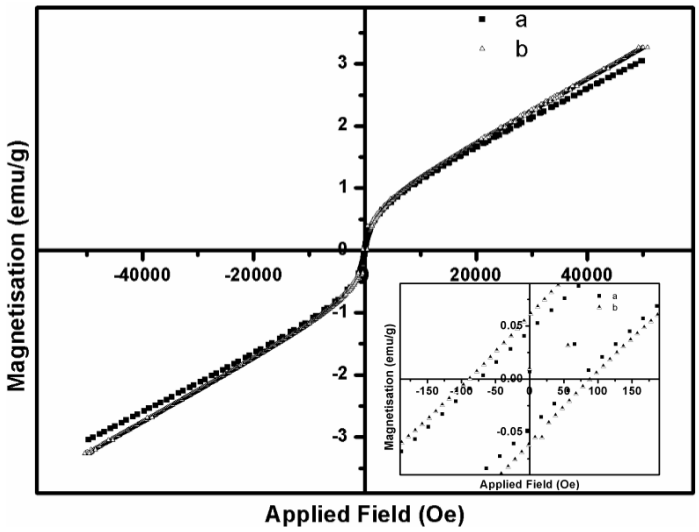

Figure. 4.8. *M-H curve of solvothermally prepared (a) α-Fe_2O_3 (b) α-Fe_2O_3/GO composite at 300 K. Inset show enlarged view.*

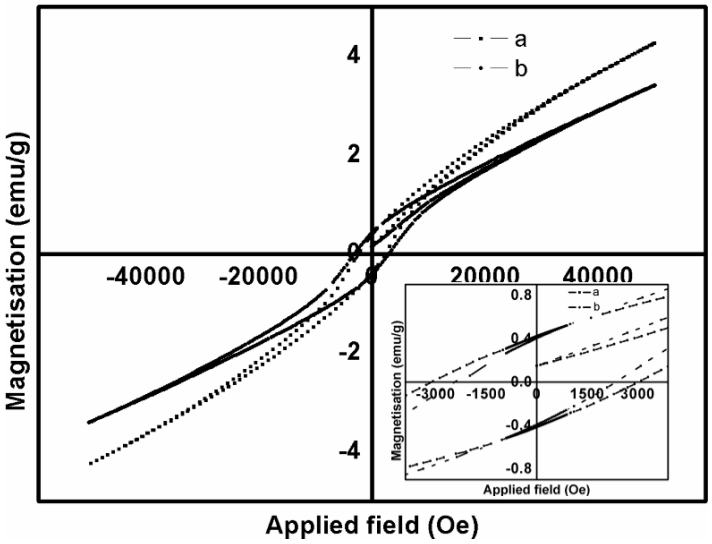

Figure. 4.9. *M-H curve of solvothermally prepared (a) α-Fe_2O_3 (b) α-Fe_2O_3/GO composite at 5 K. Inset show enlarged view.*

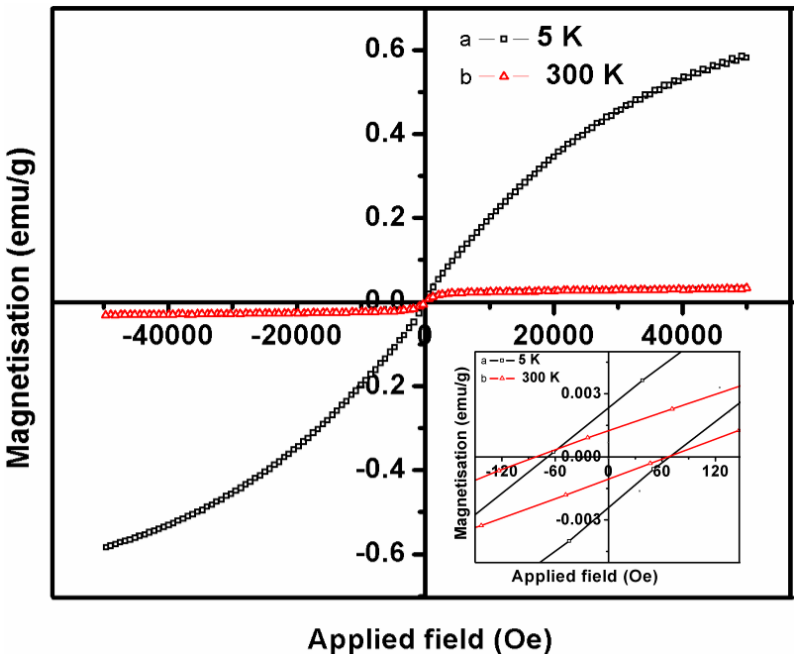

Figure. 4.10. *M-H curve of GO synthesised by Hummers method (a) at 5 K and (b) at 300 K. Inset show enlarged view.*

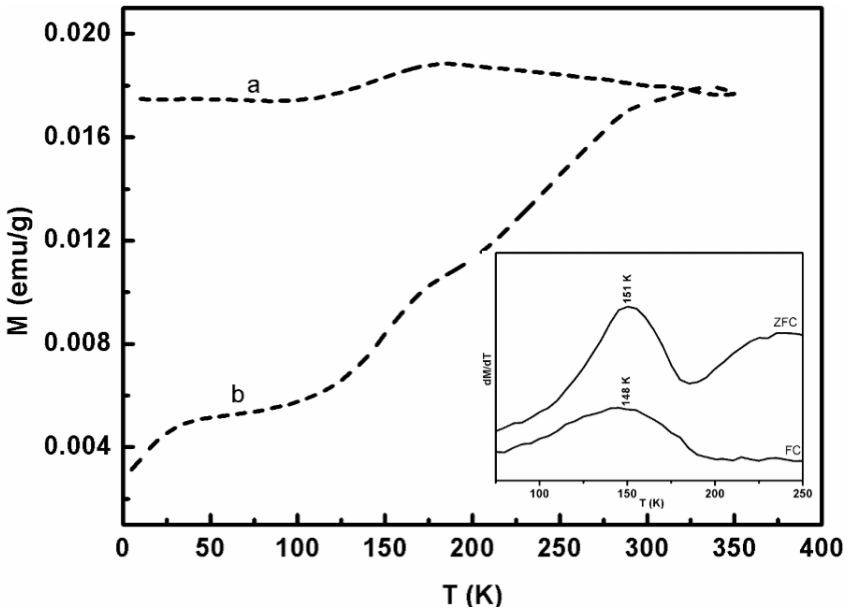

Figure. 4.11. *M-T curve of solvothermally prepared α-Fe_2O_3 (a) FC (b) ZFC. Inset show dM/T vs T curve.*

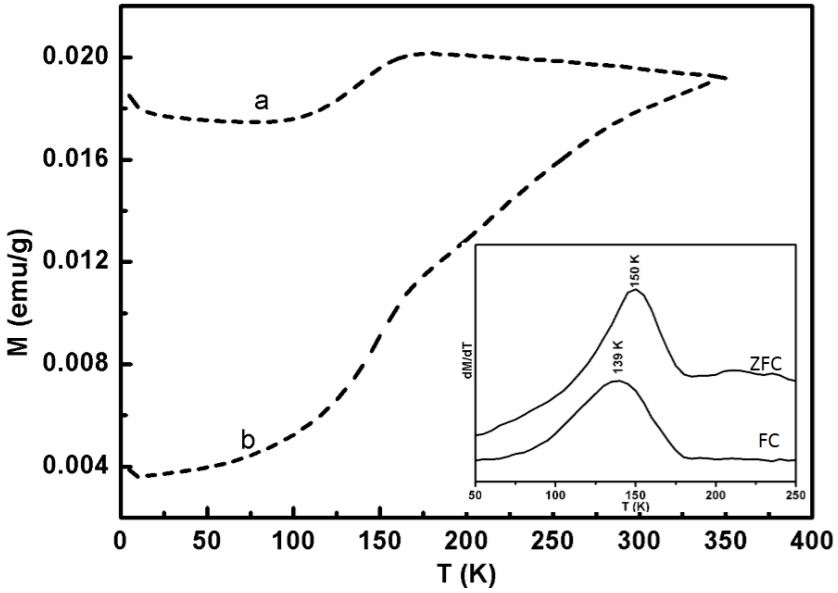

Figure .4.12*. M-T curve of solvothermally prepare α-Fe_2O_3/GO(a) FC (b) ZFC. Inset show dM/T vs T curve.*

Table. 4.1. *Magnetic parameters of solvothermally grown α-Fe_2O_3 and α-Fe_2O_3/GO.*

Sample	Average particle size nm) (FE-SEM)	Coercivity (H_C) (Oe)		Remanence (M_R)(emu/g)		Magnetic saturation (M_S)(emu/g)		Morin transition temperature (M_T) (K)	
		300 K	5 K	300 K	5 K	300 K	5 K	FC	ZFC
α-Fe_2O_3	64	76	2335	0.045	0.4	3	4.3	148	151
α-Fe_2O_3/GO	72	88	3064	0.060	0.44	3.27	4.4	139	150

4.4. Conclusions

Graphene oxide and spherical shaped α-Fe_2O_3/GO nanocomposites synthesized with GO and precursor salts of α-Fe_2O_3 in acetonitrile medium is disordered than GO. The electronic structure of GO is not disturbing the band structure of α-Fe_2O_3. Room temperature electrical conductivity and optical band gap of α-Fe_2O_3/GO are comparable to semiconductors. Magnetic coercivity of α-Fe_2O_3 is increased on lowering the temperature of the sample to 5 K due to frozen canted spin. The slight increase in magnetic coercivity of α-Fe_2O_3/GO with respect to α-Fe_2O_3 at room temperature and enhancement at 5 K is synergetic effect attributed to RKKY interactions between 'd' electrons of α-Fe_2O_3 and the conducting electrons of GO. The remanence and saturation magnetisation of α-Fe_2O_3/GO is higher than α-Fe_2O_3 may be related to the presence of weak super-paramagnetic graphene oxide. The thermal hysteresis at Morin transition temperature of the order of 11 K, is observed in α-Fe_2O_3/GO nanocomposites.

.....ꕥ.....

Chapter 4

Chapter 5

Magnetic properties of α/γ-Fe_2O_3 nanocomposite synthesized by solution combustion method

Contents

5.1. Introduction

Iron oxide nanoparticles can be used for magnetic storage applications [Vujtek M *et al;* 2003], gas sensors [Yan S *et al;* 2015], water purification [Zhong L S *et al;* 2006], catalysis [Weldemarim Y *et al;* 2015] and electrolyte materials [Ovshinsky S R *et al;* 1996] etc. Hematite (α-Fe_2O_3) and maghemite (γ-Fe_2O_3) are polymorphs of iron oxide exist in single or mixed phases with Fe^{3+} cation [Demir V *et al;* 2015].

Among the two phases of Fe_2O_3, hematite (α-Fe_2O_3) is abundant in nature, while maghemite (γ-Fe_2O_3) is formed by the reduction of hematite at higher temperatures. Hematite (α-Fe_2O_3), maghemite (γ-Fe_2O_3) shows antiferromagnetic and ferromagnetic properties respectively [Chirita M *et al;* 2009]. Composite phase of α/γ-Fe_2O_3 expected to show magnetic exchange biase it can be used for magnetic storage media [Dieny B *et al;* 1991]. Sol-gel method can be employed for the synthesis of ferromagnetic iron oxide with different shape and

morphology [Syed F N *et al;* 2014]. Magnetisation and coercivity of sol-gel prepared iron oxide is found to be increased with annealing temperature [Akbar S *et al;* 2004]. Mixed phase of α and γ-Fe_2O_3 were obtained by optimization of sol-gel method using reactants iron nitrate and citric acid [Kayani Z N *et al;* 2014]. Deraz *et al* synthesized α and γ-Fe_2O_3 by using glycine and ferric nitrate with combustion synthesis [Deraz N M *et al;* 2012]. Morphology and magnetic properties of combustion derived iron oxide nanoparticles depends on nature of initial reactants and molarity of the precursor solution used for the synthesis. A metallic salt is used as oxidizer and organic compound generally used as fuel, for combustion synthesis oxidizer to fuel ratio plays an important role in determining the chemical composition of end product. Magnetic properties of iron oxide is related to content of α and γ phases in it, the quantity of α and γ phase of Fe_2O_3 can be controlled by changing oxidizer to fuel ratio of precursor solution used for combustion synthesis. In the present work α/γ-Fe_2O_3 is synthesized by combustion method using iron chloride as oxidizer and citric acid as fuel and its magnetic properties are investigated.

5.2. Experimental

Iron oxide (α and γ) mixed phase nanoparticles were synthesized by solvent combustion synthesis method. $FeCl_3$ and citric acid were used as oxidizer and fuel respectively for the reaction. Dilute HNO_3 (25 ml) was added to $FeCl_3$ and citric acid solution (50 ml) and neutralised with ammonia. The reaction was carried out in a beaker kept over a hot plate set to a temperature of 300 ^{0}C. Sample of α-Fe_2O_3 enriched iron oxide (**Fe11**)

and γ-Fe2O3 enriched (**Fe14**) were synthesized by varying the oxidizer to fuel ratio 1:1 (6:6 gm) and 1:4 (1.5:6 gm) respectively. TEM and SAED pattern of the samples were measured with JEOL/JEM 2100 transmission electron microscope. Adsorption studies were carried out using UV-Visible (JASCO V-570) spectrometer. The surface area of sample was determined with Brunauer Emmett Teller analysis (BET) using Quantachrome Instruments version 3.0. The characterizations such as XRD, FTIR, DRS, dc conductivity were studied using same instruments reported in the experimental section of chapter 3 and 4. Magnetic studies were performed by using VSM Lakeshore 7410.

5.3. Results and Discussion

XRD of **Fe11** and **Fe14** matches to standard pattern of α and γ-Fe_2O_3 phases (JCPDS No: 13-0534, 39-1346). The X-ray diffraction pattern of both α and γ-Fe_2O_3 gives diffraction peaks corresponds to 2θ value at 35.6, α-Fe_2O_3 shows peak at 33.1 (Figure 5.1). The intensity ratio of XRD peak at 35.6 to 33.1 ($I_{35.6}$ /$I_{33.1}$) gives the information about enrichment of γ phase [Deraz N M *et al;* 2012]. The ratio ($I_{35.6}$ /$I_{33.1}$) of **Fe11** is estimated to be 0.67 and that of **Fe14** is about 3.43. The samples (**Fe11**) synthesised using less amount of fuel gives small value (0.67) of $I_{35.6}$ /$I_{33.1}$ indicate that less amount of γ-Fe_2O_3 is obtained. But γ-Fe_2O_3 found to increase with respect to fuel content up to an optimised value (1:4 oxidizer fuel ratio) which is clear from relatively larger $I_{35.6}$ /$I_{33.1}$ (3.43) value (Table 5.1). The enriched γ-Fe_2O_3 content in sample grown using 1:4 oxidizer fuel ratio is attributed to increased conversion of α-Fe_2O_3 to γ-Fe_2O_3 phase [Deraz N M *et al;*

2012]. EDAX analysis of both samples identifies the presence of iron and oxygen.

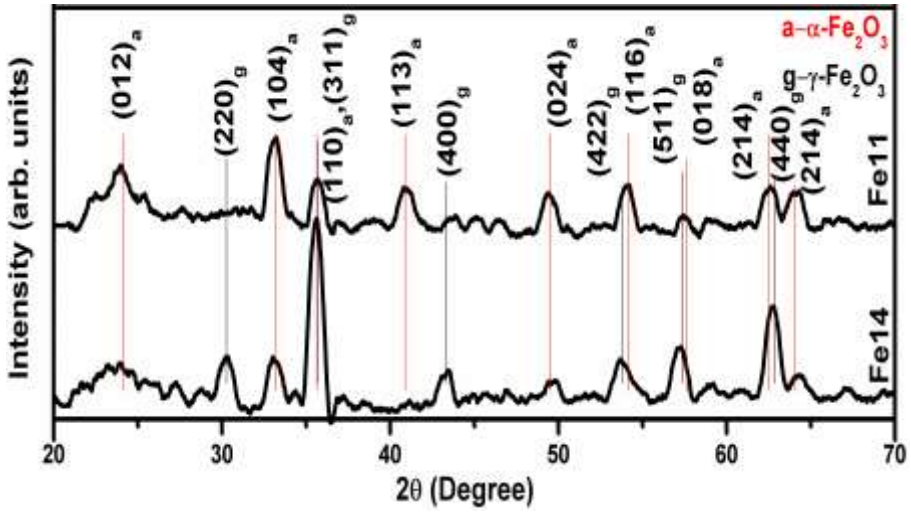

Figure. 5.1*. XRD pattern of combustion synthesized nanoparticles (a) (**FE11**) α/γ-Fe_2O_3 (α-enriched), (b) (**FE14**) (α/γ-Fe_2O_3 (γ-enriched)).*

Table. 5.1. *Lattice parameters of sample (**FE11**) α/γ-Fe_2O_3 (α-enriched) and (**FE14**) α/γ-Fe_2O_3 (γ-enriched).*

Sample	**Calculated lattice parameters (Å)**		**Peak intensity (arb. units)**		**($I_{35.6}/I_{33.1}$)**
	α-Fe_2O_3	**γ-Fe_2O_3**	33.1	35.6	
Fe11	a= 5.074 c=13.329	a=b=c=8.414	46	27	0.63
Fe14	a= 5.044 c=13.578	a=b=c=8.365	32	109	3.43

FTIR spectra of **Fe11** and **Fe14** shows intense band at 456 cm^{-1}, along with a broad band (500-767 cm^{-1}) centred at 555 cm^{-1}. In the case of **Fe14** additional shoulder band is seen at 630 cm^{-1} (Figure 5.2). The IR band at 456 cm^{-1} is corresponds to α-Fe_2O_3 [Umar A *et al;* 2014], and 555 cm^{-1} assigned to Fe-O vibration of γ-Fe_2O_3 [Ganachari S Y *et al;* 2012]. Weak band at 630 may be due to cation vacancies in the lattice which generated as a result of surface oxidation [Roca A G *et al;* 2007].

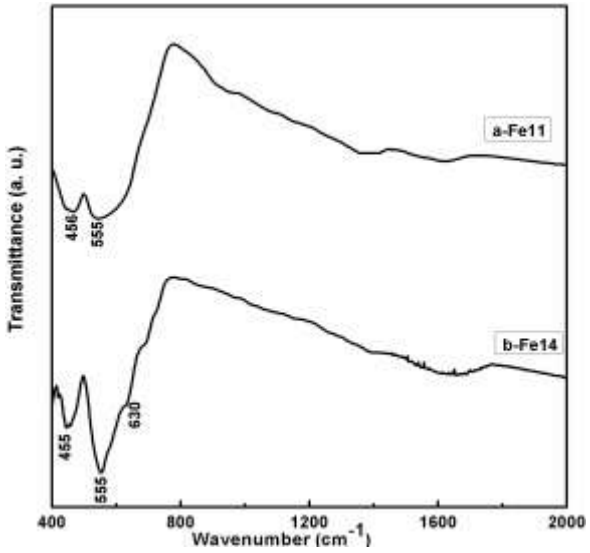

Figure. 5.2. *FTIR spectra of combustion synthesized nanoparticles (a) (**FE11**) α/γ-Fe_2O_3 (α-enriched, (b) (**FE14**) (α/γ-Fe_2O_3 (γ-enriched)).*

TEM images of **Fe11** shows that particles are in the size range 8 to 22 nm and that of the **Fe14** are 5 to 15 nm. The particle size distribution histogram of sample gives an average size of 12 and 11 nm for **Fe11** and **Fe14** respectively. HRTEM images indicate that α-Fe_2O_3 and γ-Fe_2O_3 crystalline phases are co-exist in the sample with inter-planar distance of 0.29 (α-Fe_2O_3) and 0.25 (γ-Fe_2O_3) nm. SAED of **Fe11** is having planes (404), (018), (113) corresponds to α-Fe_2O_3 and (611), (422) related to

γ-Fe_2O_3. Similarly **Fe14** is also having planes related to α-Fe_2O_3, which are (048) and (104). γ-Fe_2O_3 is also seen in **Fe14** with (521), (400) planes shown in Figure 5.3 and 5.4.

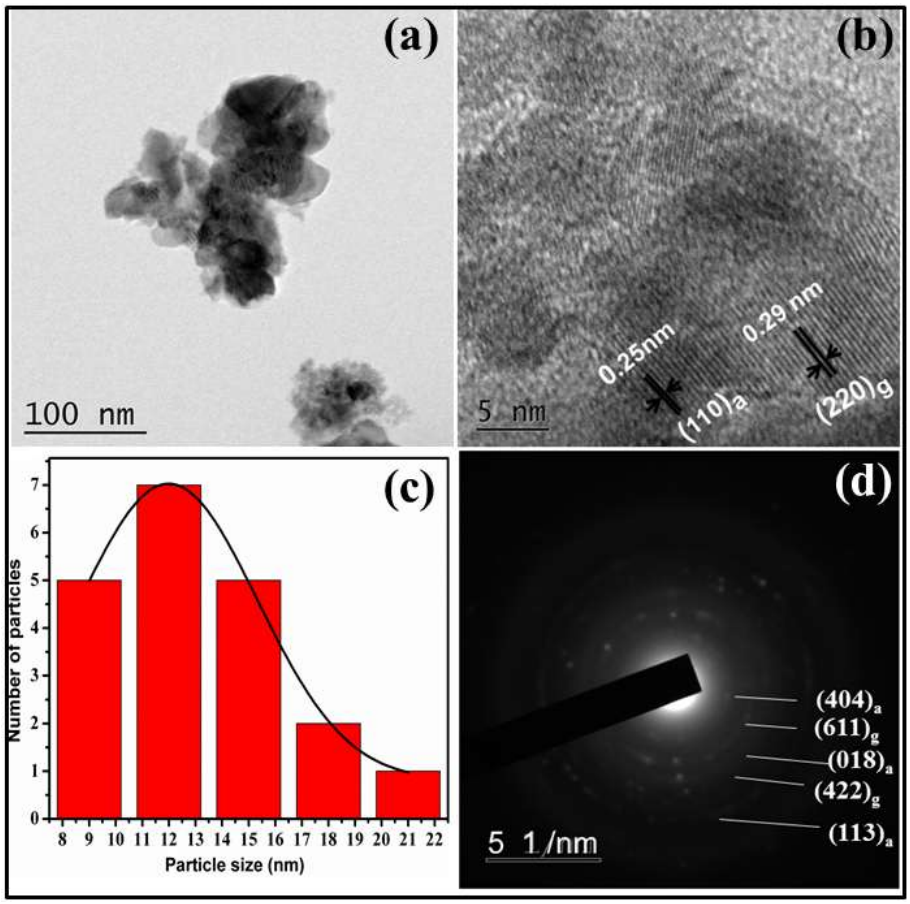

Figure. 5.3. *TEM images of (a) (**FE11**) α/γ-Fe_2O_3 (α-enriched) low resolution (b) high resolution (c) particle size distribution and (d) SAED pattern.*

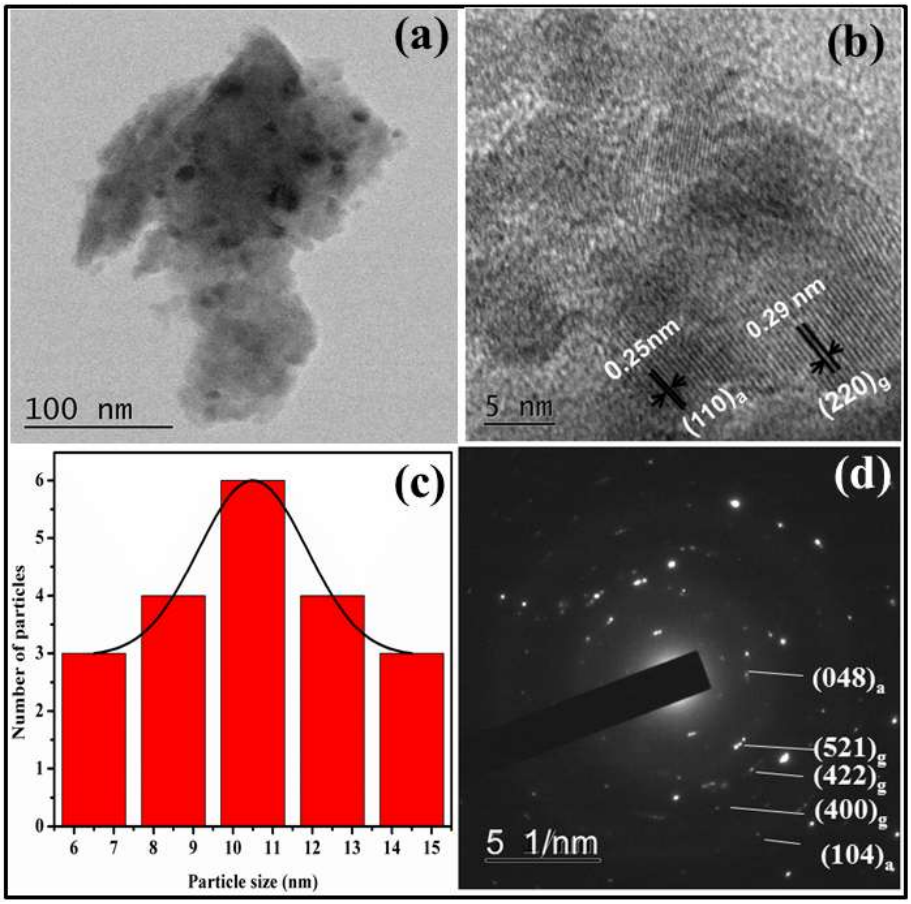

Figure. 5.4. *TEM images of (a) (**FE14**) α/γ-Fe_2O_3 (γ-enriched) (b) high resolution (c) particle size distribution and (d) SAED pattern.*

Optical band gap of α-enriched (1.97), and γ-enriched (1.87) mixed phase of α/γ-Fe_2O_3 samples shows almost same value for band gap (Figure 5.5) which lies within reported values [Syed F N *et al;* 2014].

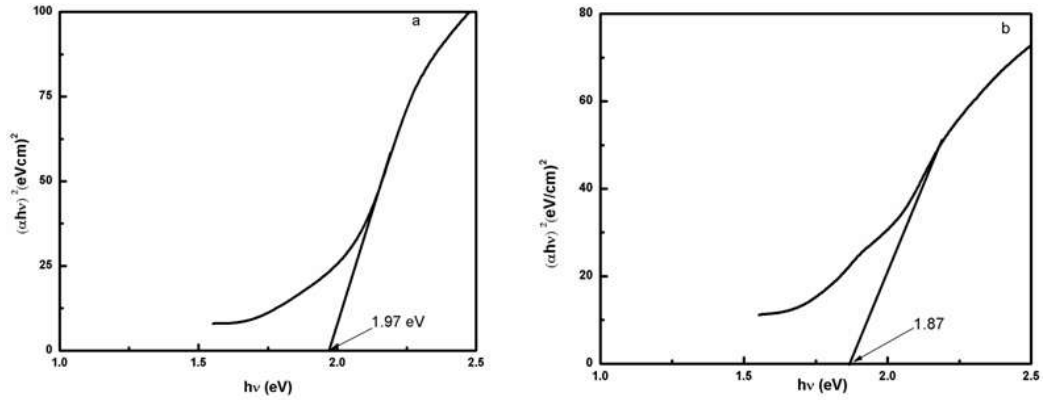

Figure. 5.5. *Tauc plot of (a) (**FE11**) α/γ-Fe_2O_3 (α-enriched) (b) (**Fe14**) α/γ-Fe_2O_3 (γ-enriched).*

Room temperature *dc* electrical conductivity of α-enriched mixed phase of Fe_2O_3 (**Fe11**) is 4.67×10^{-6} S/cm and that of γ-enriched mixed phase Fe_2O_3 (**Fe14**) is 4.02×10^{-7} S/cm (Figure 5.6). Both the samples show semiconducting behavior and its activation energy is 0.32 eV (**Fe11**) and 0.29 eV (Fe14). This observation indicates that combustion synthesis method can be used for the synthesis of semiconducting α/γ-Fe_2O_3.

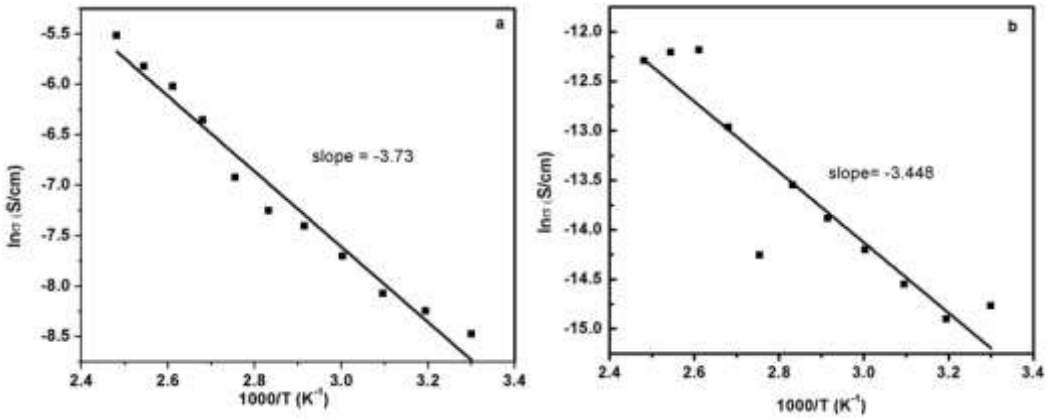

Figure. 5.6. *Arrhenius plot of (a) (**FE11**) α/γ-Fe_2O_3 (α-enriched) (b) (**Fe14**) α/γ-Fe_2O_3 (γ-enriched).*

M-H curve of **Fe11** at 300 and 20 K is non-saturated, whereas **Fe14** exhibit saturation on increasing field strength (Figure 5.7 and 5.8). Magnetic coercivity and exchange bias is calculated using equations '$H_E = -(H_{right} + H_{left})/2$, $H_C = (H_{right} - H_{left})/2$. H_{right} and H_{left} are points, where hysteresis loop intersect with the applied field axis [Iglesias A *et al;* 2008]. The room temperature (300 K) coercivity of **Fe11** is 492 Oe, which is increased to 859 Oe while lowering the temperature of the sample to 20 K. Magnetic remanence of **Fe11** at 300 K is 0.3 emu/g and it increase to 0.79 emu/g at 20 K. The M-H curve of **Fe14** is saturating at about an applied field of 3300 Oe (300 K) and low temperature 3200 Oe (20 K). The saturation magnetisation of this sample (**Fe14**) is 52 (20 K) and 48 (300 K) emu/g. Magnetic coercivity of **Fe14** is less than that of **Fe11** at room temperature, which shows a value of 149 Oe and its coercivity value at 20 K is 232 Oe (Table 5.2). However its room temperature (300 K) magnetic remanence (7.12 emu/g) is comparatively higher than that of **Fe11** and its low temperature value is also higher (10.11 emu/g). FC of **Fe11** shows zigzag appearance up to 165 K and is found to be increase until 41 K, then decreases (Figure 5.9).

Magnetisation increases with respect to decreases in temperature under field cooling condition (Figure 5.9). The FC and ZFC pattern of **Fe14** is different from **Fe11** (Figure 5.10). Magnetisation of ZFC is decreased gradually in the temperature range 300-110 K, and it is slightly increased up to 88 K, then magnetisation decreases rapidly on lowering the temperature. However, the magnetisation under FC condition shows almost constant value up to 115 K and is slightly increases until 66 K. FC and ZFC meet at 296 K corresponds to blocking temperature. The absence of

magnetic saturation of sample even at an applied field of 20 kOe is due to non collinear arrangements of magnetic moments random canting or thermal disorder [Garcia M P F *et al;* 2010]. XRD pattern of **Fe11** show the occurrence of α and γ phase of Fe_2O_3, α-Fe_2O_3 usually exhibit antiferromagnetism whereas γ-Fe_2O_3 show ferromagnetism at room temperature [Chirita M *et al;* 2009]. Saturation magnetisation can be estimated by plotting M Vs. 1/H graph [Tadic M *et al;* 2012]. The room temperature magnetic saturation values of both sample (**Fe11** (32.7 emu/g), **Fe14** (48 emu/g)) are less compared to the magnetic saturation value of bulk γ-Fe_2O_3 (73.5 emu/g) [Jing Z H *et al*; 2004]. Lowering of magnetic saturation of present sample may be due to surface spin canting effect accompanied by structural order-disorder differences [Morales M P *et al*, 1999; Asuha S *et al*, 2011]. Further, low value of magnetic saturation of **Fe11** is due to higher content of antiferromagnetic (α-Fe_2O_3) content compared to **Fe14**.

Magnetic irreversible nature of samples can be understood from the plot between magnetic irreversibility (M_{irr}) with temperature (T) (Figure 5.11). The magnetic irreversibility (M_{irr}) curve M_{FC}-M_{ZFC} Vs T of **Fe11** gradually increases with lowering of temperature. There is no change in M_{irr} of **Fe14** with respect to temperature. The blocking temperature of samples is found to be increasing with increase of particle size. Blocking temperature calculated using the equation $T_B=K_{eff}V/25K_B$, where V is the average volume of particles, K_B- Boltzman constant and K is the magnetic anisotropy constant and K_{eff} for Fe_2O_3 naoparticles is $1.6x10^4$ J/m^3 [Guivar J A R *et al;* 2014].

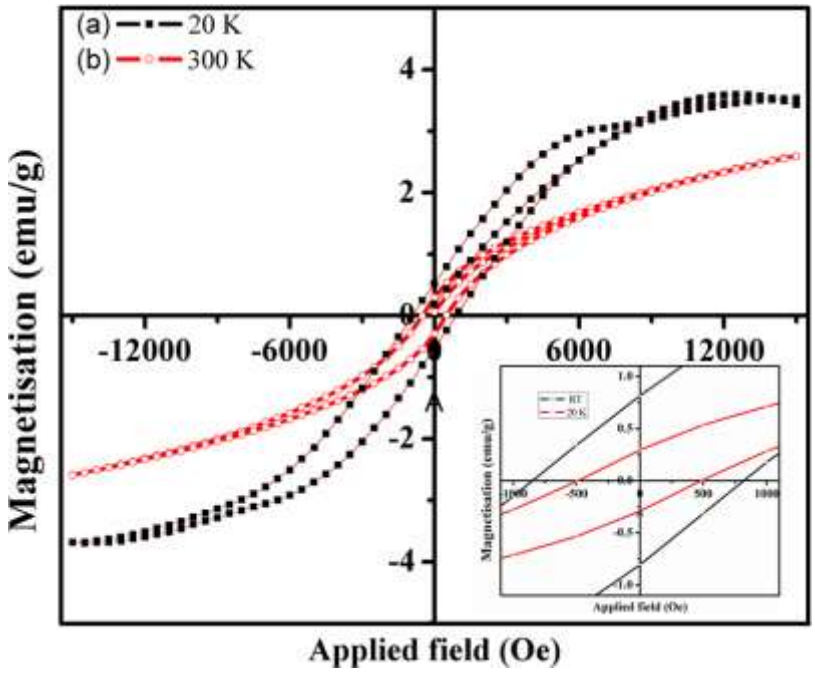

Figure. 5.7. *M-H curve of combustion synthesized sample (**FE11**) α/γ-Fe_2O_3 (α-enriched) (a) at 300 and (b) 20 K.*

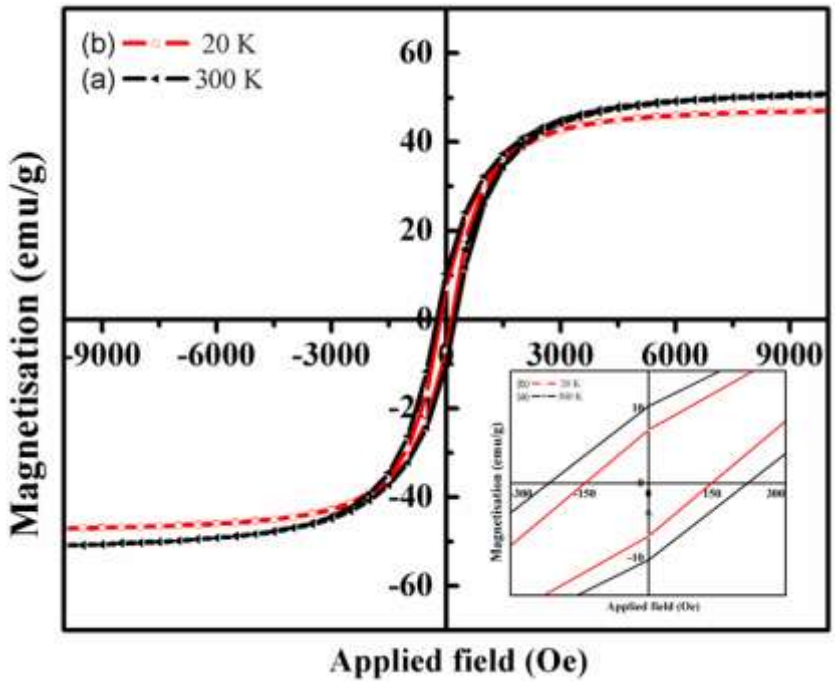

Figure. 5.8*. M-H curve of combustion synthesized sample (**FE14**) α/γ-Fe_2O_3 (γ -enriched) (a) at 300 and (b) 20 K.*

The blocking temperature is estimated to be 334 and 276 K for **Fe11** and **Fe14** respectively, which is almost close with obtained value. The slight difference in observed and theoretically calculated value is due to broad particle size distribution and magnetic anisotropy change [Knobel M *et al;* 2008, Silva M F *et al; 2013*].

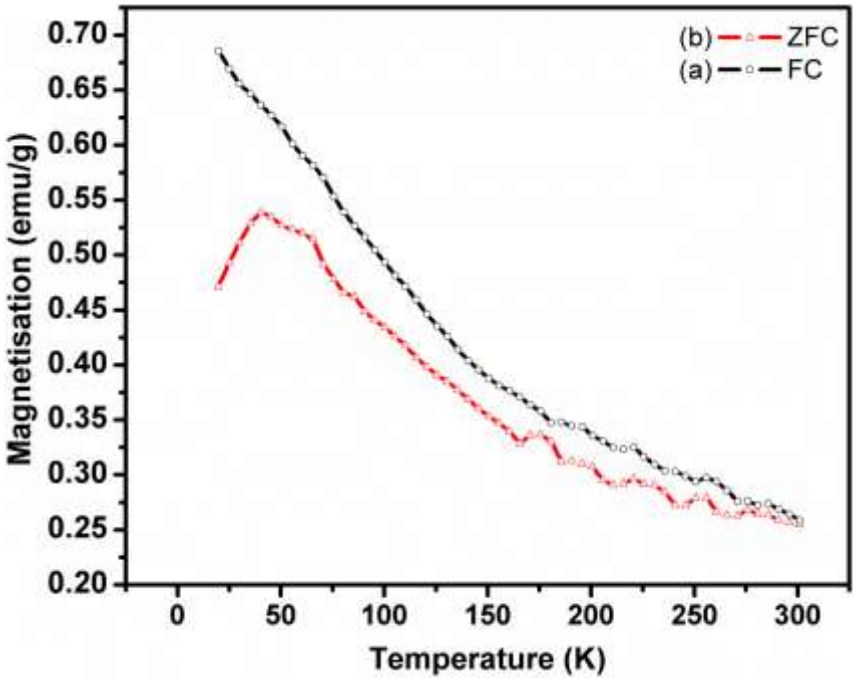

Figure. 5.9. *Temperture dependant magnetisation of combustion synthesized sample (**FE11**) α/γ-Fe_2O_3 (α-enriched) (a) FC and (b) ZFC.*

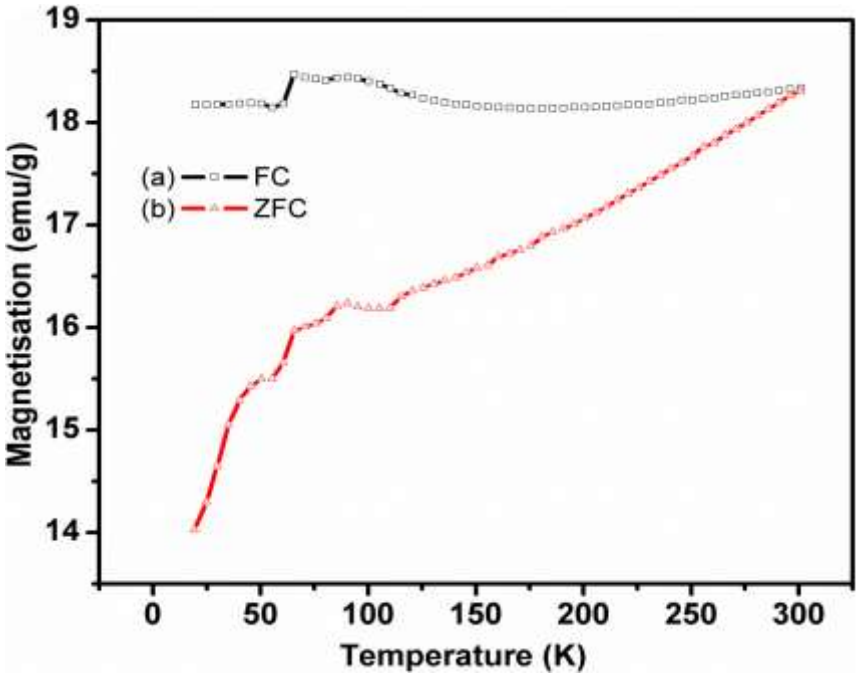

Figure. 5.10. *Temperture dependant magnetisation of combustion synthesized* ***(FE14)*** *α/γ-Fe_2O_3 (γ-enriched) (a) FC and (b)ZFC.*

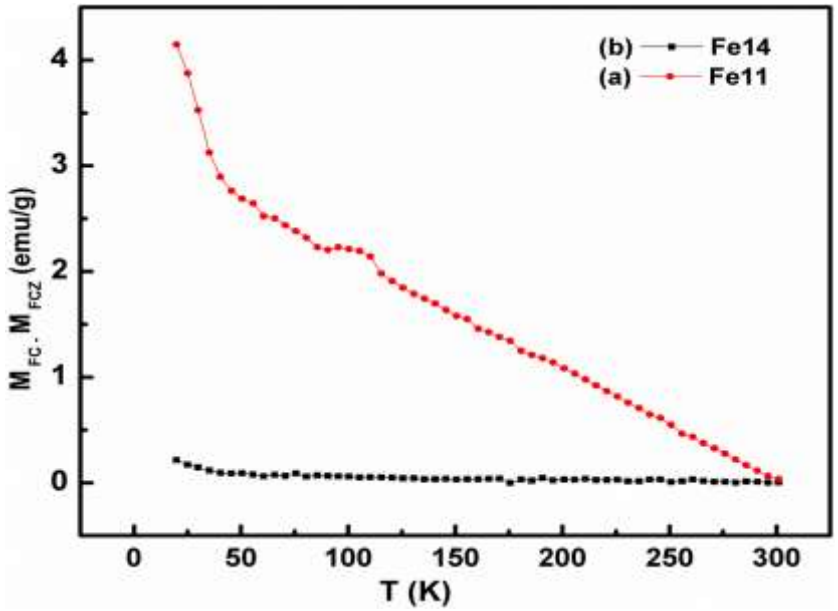

Figure. 5.11. *Magnetic irreversibility with temperature of combustion synthesized samples (a)* ***(FE11)*** *α/γ-Fe_2O_3 (α-enriched) and (b)* ***(FE14)*** *(α/γ-Fe_2O_3 (γ-enriched).*

Table. 5.2 *magnetic parameters of* ***FE11*** *(α/γ-Fe_2O_3 (α-enriched)) and (b)* ***FE14***

(α/γ-Fe_2O_3 (γ-enriched)).

Sample code	Particle size from TEM (nm)	H_c (Oe)		M_r (emu/g)		M_S (emu/g)		H_E (Oe)		B_T (K)
		300 K	20 K	300 K	20 K	300 K	20 K	300 K	20 K	
Fe11	11	486	848	0.30	0.79	32	33	6	12	256
Fe14	12	149	237	7.12	10.1	48	52	-	-	296

BET surface analysis of γ-Fe_2O_3 having size of 58 nm gives the surface area value of about 75.73 m^2/g and pore radius is 1.73 nm (Figure 5.12). These values are comparable with that of α/γ-Fe_2O_3 (γ-enriched) nanoparticle synthesized by citrate nitrate method [Ahmed M A *et al;* 2013].

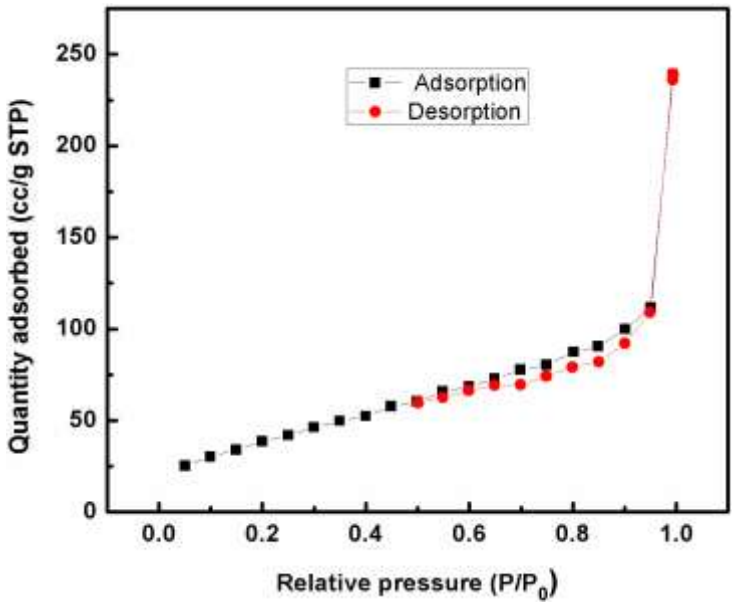

Figure. 5.12*. Adsorption-desorption isotherm of combustion synthesized α/γ-Fe_2O_3 (γ-enriched) nanoparticles.*

5.3.1. Nickel ion adsorption studies

Magnetic adsorbent materials are potentially important, since the adsorbents can be easily remove from the purifying system using magnets. α/γ-Fe_2O_3 particularly useful for absorption removal of Ni(II) from contaminated water. The intensity variation of absorption peak of Ni(II) at 388 nm (25773 cm^{-1}) is used for the present investigation to know the Ni(II) ion removal efficiency of α/γ-Fe_2O_3 (γ-enriched). The effect of contact time, adsorbent dosage and pH in the adsorption of Ni(II) ion by the α/γ-Fe_2O_3 (γ-enriched) are carried out. The removal efficiency of different samples under investigation is calculated using the equation, removal efficiency(R_E) = ((A_s–A_t)/(A_s)) x 100 %) [Dong Z *et al;* 2014] where, A_s-absorbance of stock solution, A_t-absorbance of treated stock solution.

Optical absorption property of 0.1 M nickel acetate solution (stock solution) after adsorption treatment using α/γ-Fe_2O_3 (γ-enriched) is studied. Figure 5.13(a) depicts the absorption spectrum corresponds to 0.1 M nickel acetate solution (stock solution) and figure 5.13 (b) represent α/γ-Fe_2O_3 (γ-enriched) (20 mg/L) treated nickel acetate solution. An intense peak is seen from the nickel acetate solution at 387 nm (25839 cm^{-1}) followed by a broad peak which extends from 565 (17699 cm^{-1}) to 855 nm (11695 cm^{-1}), with peaks at 654 nm (15290 cm^{-1}) and 707 nm (14144 cm^{-1}) [Narayana P A *et al;* 1968]. The intensity of absorption band at 387 nm (25839 cm^{-1}) is found to be reduced to 9 % on α/γ-Fe_2O_3 (γ-enriched) nanoparticles treatment. Further, an intense band is observed in the treated solution at 297 nm (33670 cm^{-1}) which indicates the presence of Fe(III) ions [Seraghni N *et al;* 2012]. The reduction in intensity of absorption peak at 387 nm (25839 cm^{-1}) indicates the decrease of Ni(II) ion concentration in treated solution, which is due to the adsorption of Ni(II) ions by α/γ-Fe_2O_3 (γ-enriched).

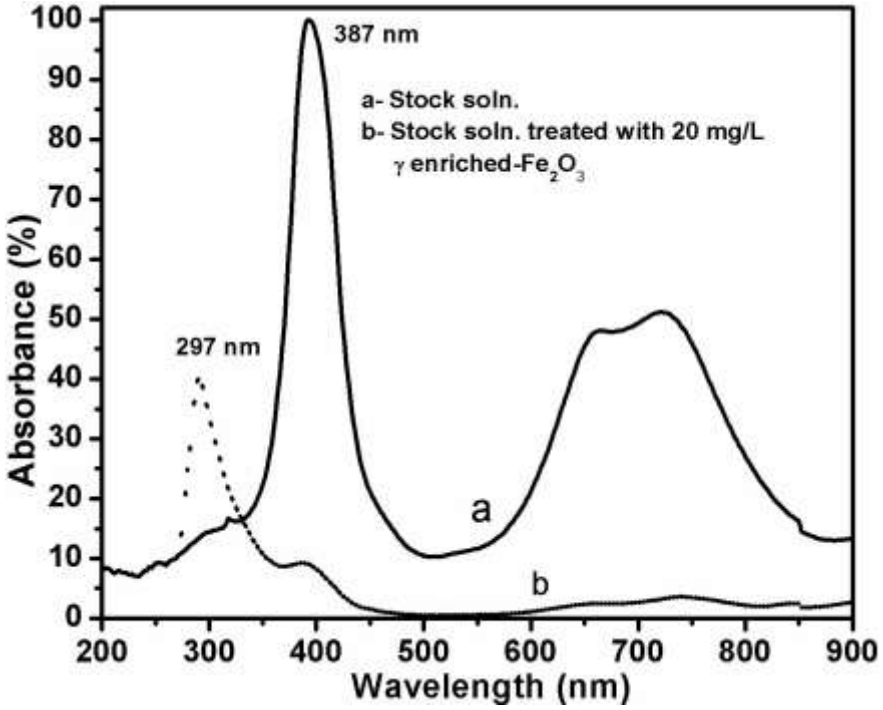

Figure. 5.13. *Optical absorption spectra of (a) stock solution and (b) stock solution after treat with combustion synthesized* α/γ-Fe_2O_3 (γ- *enriched) (20 mg/L).*

The effect of pH on adsorption removal efficiency of α/γ-Fe_2O_3 (γ-enriched) (1 to 8) with fixed time of contact (10 min.) and adsorbent dosage (6 mg/L) is shown in the Figure .5.14. The removal efficiency at acidic pH 1 is low and it increases with pH value. The Ni(II) removal efficiency further increases with increase of pH value to 8, as one can see from the graph (Figure 5.14). The adsorption of Ni(II) ions is low because of this mechanism happening through ion exchange between H^+ and Ni^{2+} ions similar to that of between Cu^{2+} and H^+ [Hu J *et al;* 2006]. In alkaline pH (pH=8), good removal efficiency is obtained as the surface charges are more electronegative attributed to higher concentration OH^- which increase cation (Ni(II)) ion adsorption [Hu J *et al;* 2006]. However, on increasing the pH beyond 9, Ni(II) precipitate out as its hydroxides which make

difficult the adsorption study similar to reported previously [Salmani M H *et al;* 2013].

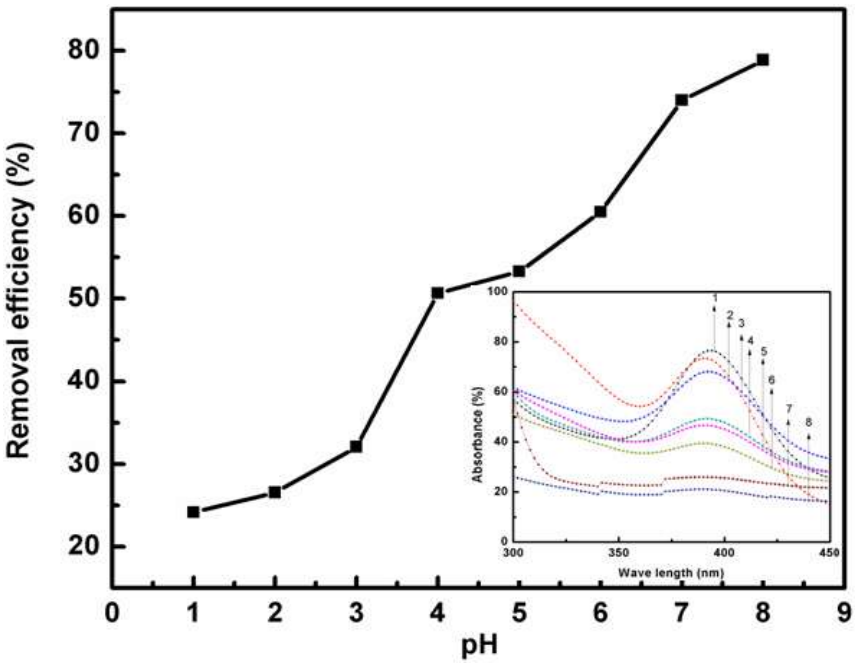

Figure. 5.14. *The effect of pH on Ni(II) removal from 0.1 M nickel acetate solution using combustion synthesized 6 mg/L α/γ-Fe_2O_3 (γ-enriched) with a time of contact 8 min. Inset shows optical absorption spectra of stock solution after treated with 6 mg/L α/γ-Fe_2O_3 (γ-enriched).*

To study the effect of time of contact on the Ni(II) ion removal efficiency we performed adsorption experiments by varying contact time as 2, 4, 6, 8, 10, 20, 30 min. with adsorbent dosage (6 mg/L) while keeping the pH at 8. The Ni(II) removal efficiency of α/γ-Fe_2O_3 (γ-enriched) increases with time of contact up to 8 min. (Figure 5.15) after that there is no variation. This behaviour shows that the adsorption of Ni(II) ion on α/γ-Fe_2O_3 (γ-enriched) is a gradual process that requires certain time to fill all adsorption sites in an adsorbent. In the present case, the time required to occupy adsorbate in all adsorption sites is about 8 min. Exposing the adsorbent material to stock solution (nickel acetate) more than 8 min. did

not give any appreciable differences in Ni(II) ion removal efficiency of α/γ-Fe_2O_3 (γ-enriched). The minimum time required for the adsorption to reach equilibrium (equilibrium time) is 8 min.

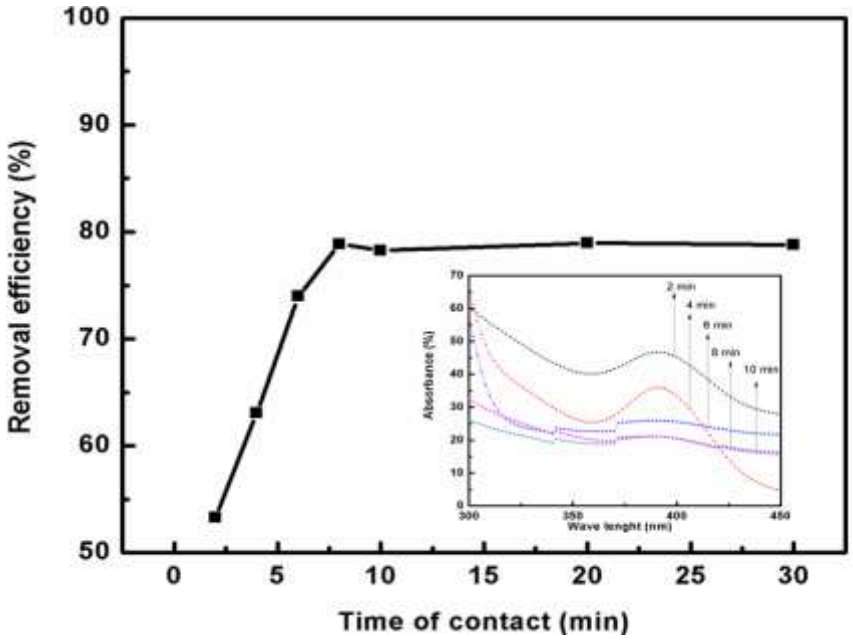

Figure. 5.15. *The effect of contact time (min.)on Ni(II) removal from 0.1 M nickel acetate solution (pH=8) by using 6 mg/L combustion synthesized α/γ-Fe_2O_3 (γ-enriched). Inset shows optical absorption spectra of stock solution after treated with 6 mg/L α/γ-Fe_2O_3 (γ-enriched) with different contact time.*

The effect of adsorbent dosage (6, 10, 15 and 20 mg/L) with constant time of contact (8 min.) and pH 8 are shown in the figure 5.16. The Ni (II) removal efficiency is about 78 % when the experiment is conducted with an adsorbent dosage of 6 mg/L. But Ni(II) removal efficiency is increased with respect to adsorbent dosage. It shows maximum value of 91 % efficiency when the adsorbent dosage is 20 mg/L measured using UV-Visible absorption spectra. This adsorption removal efficiency value of combustion derived. α/γ-Fe_2O_3 (γ-enriched) with lower adsorbent concentration and time of contact is highest one to the best of our knowledge. The adsorption

removal efficiency with adsorbent dosage above 20 mg/L by using UV-Visible-NIR spectrum is not able to measure due to the overlapping of absorption peaks of Ni(II) and Fe(III). The α/γ-Fe_2O_3 (γ-enriched) nanoparticles (20 mg/L) is sufficient quantity for the complete removal of Ni(II) from the stock solution.

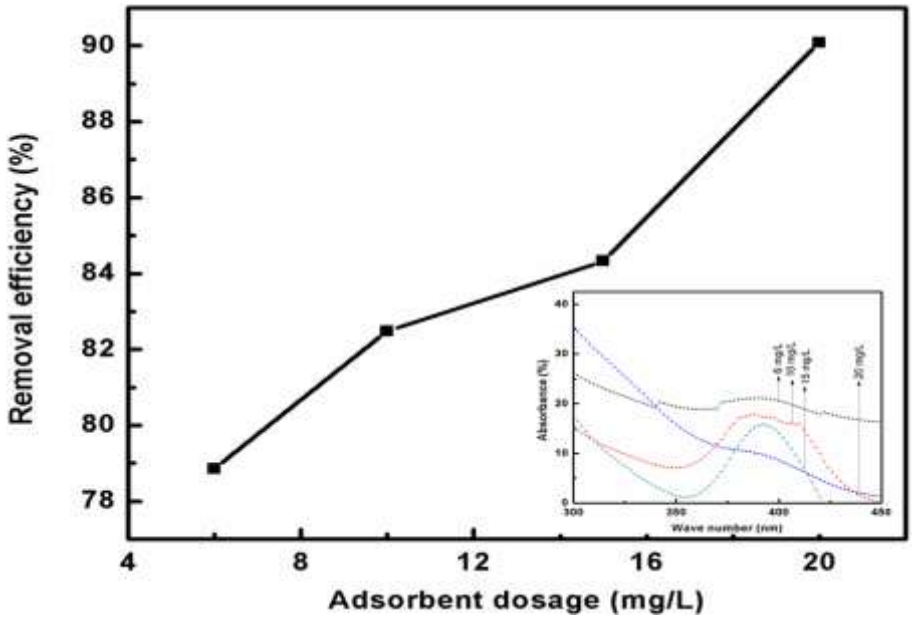

Figure. 5.16*. The effect of adsorbent dosage on Ni(II) removal from 0.1 M nickel acetate solution (pH=8) at fixed time of contact (8 min.) by using combustion synthesized* α/γ-Fe_2O_3 (γ-enriched)*. Inset shows optical absorption spectra of stock solution after treated with α/γ-Fe_2O_3 (γ- enriched) different dosage.*

The higher value of surface area is usually required to get better adsorption removal of heavy metal ions. The observed better efficiency of Ni(II) ion removal efficiency of α/γ-Fe_2O_3 (γ-enriched) with comparatively higher surface area and presence of OH^- already on the α/γ-Fe_2O_3 surface, which detected from FTIR analysis. Since these OH^- making the surface, charge electronegative for easy binding of cations like Ni(II) on its surface [Hu J *et al;* 2006]. In order to check the reusability of α/γ-Fe_2O_3

(γ-enriched) for adsorption removal of Ni(II) ion from the nickel acetate solution, Ni(II) adsorbed α/γ-Fe_2O_3 is treated with 0.2 M HCl and then reused for Ni(II) adsorption removal. Almost same Ni(II) removal efficiency is obtained on reusing these α/γ-Fe_2O_3 (γ-enriched) for the adsorption study on second time.

5.4. Conclusions

α/γ-Fe_2O_3 nanocomposite with different amount of alpha and gamma phases can be synthesized by varying oxidizer to fuel ratio. α/γ-Fe_2O_3 nanocomposite are exhibiting semiconducting behaviour with band gap of 2 eV. Magnetic coercivity and magnetic saturation of the samples increased with respect to γ-Fe_2O_3 content in the α/γ-Fe_2O_3 nanocomposite. The higher amount of fuel gives sample with more content of γ-Fe_2O_3, which is related to fuel content. Lower value of magnetic saturation in both sample compared to bulk γ-Fe_2O_3 is attributed to crystalline vacancies in the α/γ-Fe_2O_3 nanocomposite. α/γ-Fe_2O_3 nanocomposite is a suitable material for the adsorption removal of Ni(II) (about 90%) from the nickel acetate solution with a short time of 8 min. due to its higher order surface area and presence of crystalline defects in the nanocomposite.

.....ꕥ.....

Chapter 6

Synthesis and magnetic properties of α/γ-Fe_2O_3/graphite nanocomposite

Contents

6.1. Introduction

Hematite (α-Fe_2O_3) is an antiferromagnetic phase of iron oxide which exhibit semiconducting properties. Maghemite (γ-Fe_2O_3) is one of the ferromagnetic phases of iron oxide with wide range of technological applications [Chirita M *et al;* 2009]. The combination of hematite and maghemite phases expected to exhibit modified magnetic properties. Maghemite enriched phase of Fe_2O_3 nanoparticles find applications for magnetic fluids [Chikazumi S *et al;* 1987], magnetic storage [Hyeon T *et al;* 2001], gas sensors [Yan S *et al;* 2015], water purification [Zhong L S *et al;* 2006], catalysis [Weldemarim Y *et al;* 2015]. Interestingly, graphite is an allotrope of carbon with good mechanical strength and electrical conductivity [Raza M A *et al;* 2011, Haering R R *et al;* 1957, Chung D D L *et al;* 2002]. Iron oxide nanoparticles embedded in diamagnetic graphitic matrix likely to have good electrical conductivity and magnetism etc. Synthesis and applications of carbon based composites of α/γ-Fe_2O_3 [Lyubutina I S *et al;* 2009, Sun Y *et al;* 2013, Ye J *et al;* 2015], iron oxide

(α/γ-Fe_2O_3)/carbon nanotubes are reported previously [Lyubutin I S *et al;* 2009]. Mixed phase of Fe_2O_3/CNT is particularly useful as an anode material for lithium ion batteries [Sun Y *et al;* 2013]. Ye J *et al* reported that graphene tented iron oxide can be used in lithium storage capacities [Ye J *et al;* 2016]. In the present chapter contains the combustion synthesis of mixed alpha and gamma phase of iron oxide (α/γ-Fe_2O_3) in graphite matrix and its optical, dc conductivity, adsorption and magnetic properties.

6.2. Experimental

The precursor solution was prepared by mixing solutions of 1.5 g of $FeCl_3$ (oxidizer) in 25 ml water, 6 g of citric acid in 25 ml water along with 0.3 g of graphite powder. In the above mixture, 25 ml dilute HNO_3 was added and neutralised to pH 7 with the addition of ammonia in it. The resultant mixture of solution was heated with hot plate till the occurrence of combustion reaction with flames. Sample was collected after natural cooling of reaction system. The experiment was repeated with the identical condition, by changing the quantity of graphite (0.6 and 0.9 g) added in each experiment.

XRD, FTIR, Raman, TEM, SAED, DRS, BET, conductivity, magnetism and adsorption studies were done using same instrument mentioned in chapter 3.

6.3. Result and Discussion

XRD pattern of sample under investigation shows diffraction peaks of both α (JCPDS No: 13-0534) and γ (JCPDS No: 39-1346) phase of Fe_2O_3

and that of graphite [Uhl F M *et al*; 2005, Wakabayashi K *et al*; 2008]. Diffraction peak corresponds to graphite is seen at 26.6^0, its relative intensity increase with respect to quantity of graphite added to the precursor salts used for the combustion reaction (Figure 6.1).

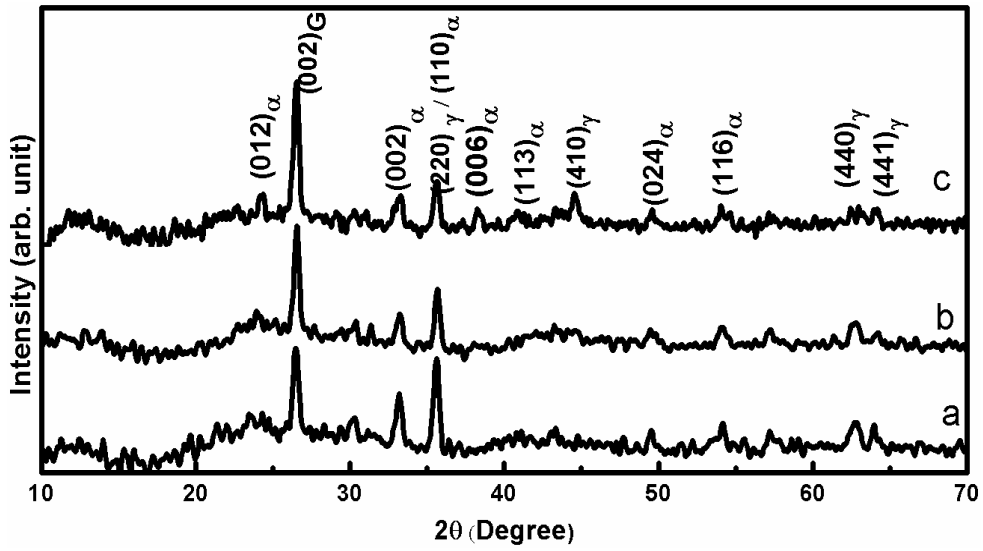

Figure. 6.1. *XRD of α/γ-Fe_2O_3/graphite composite synthesized by combustion method with the addition of (a) 0.3 g (b) 0.6 g and (c) 0.9 g graphite in the precursor solution.*

FTIR spectra of samples in the range 400-4000 cm^{-1} are shown in figure 6.2. A moderately intense IR band is seen at 458 cm^{-1} corresponds to Fe-O vibration of α-Fe_2O_3 in 0.3 g of graphite added sample [Umar A *et al;* 2014]. This band is shifted to lower energy side (451 cm^{-1}) in 0.6 and 0.9 g graphite added samples. The characteristics vibrational band of γ-Fe_2O_3 is reported at 555 cm^{-1} contributed to Fe-O [Ganachari S V *et al;* 2012]. In the the present case an intense band is seen at 549 cm^{-1} in 0.3 g graphite added sample related to Fe-O vibration. This band is shifted towards lower energy side to 543 and 536 cm^{-1} in 0.6 and 0.9 g graphite added sample

respectively. IR band at 1387 cm^{-1} attributed to C-H stretching [Xu C *et al;* 2016], and at 1632 cm^{-1} related to C=C [Gou S *et al;* 2013].

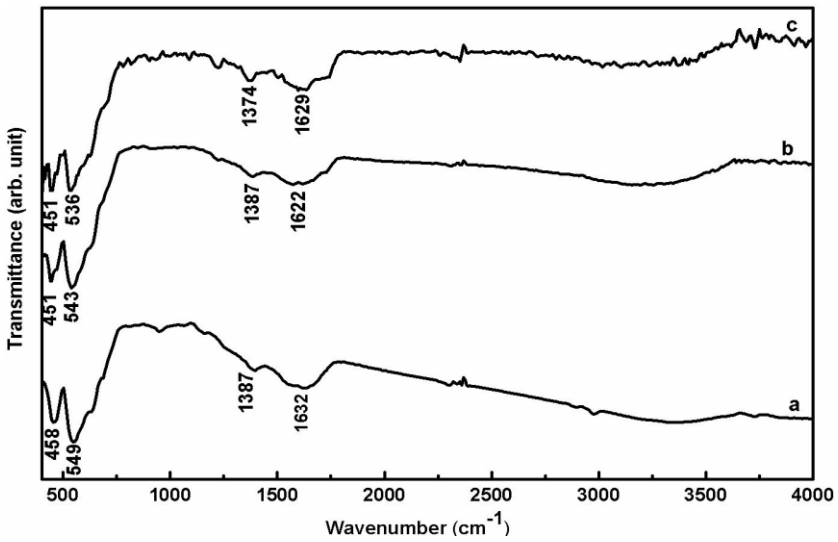

Figure. 6.2. *FTIR spectra of α/γ-Fe_2O_3/graphite composite synthesized by combustion method with the addition of (a) 0.3 g (b) 0.6 g and (c) 0.9 g graphite in the precursor solution.*

Raman spectra of 0.3 g graphite added sample show moderately intense band at 2656 and 1333 cm^{-1} followed by an intense band at 1572 cm^{-1}. These bands are also observed in other samples without much shift in its energy position. The Raman band at 1576 cm^{-1} related to G band of graphite and at 1333 cm^{-1} is defect related D band [Tuinstra F *et al;* 1970]. The intensity of Raman band corresponds to G band is relatively higher than that of D band which indicate the existence of higher crystallinity of graphite in the samples (Figure 6.3). Raman band corresponds to iron oxide is not seen in the spectra.

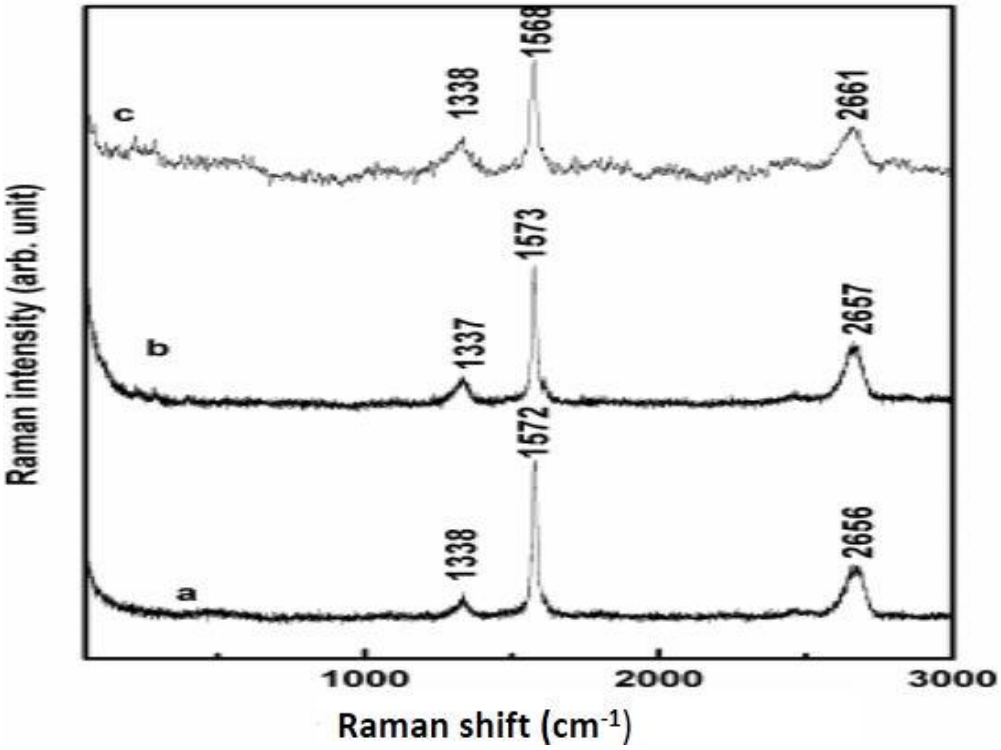

Figure. 6.3. *Raman spectra of α/γ-Fe_2O_3/graphite composite synthesized by combustion method with the addition of (a) 0.3 g (b) 0.6 g and (c) 0.9 g graphite in the precursor solution.*

TEM images of the samples indicate that iron oxide nanoparticles are dispersed in the graphite matrix (Figure 6.4, 6.5 and 6.6). Iron oxide particles having size in the range 5-30 nm with an average size of 20 nm (0.3 g graphite added sample). In the case of 0.6 g graphite added sample, average size of iron oxide particle is 37 nm in which particle size distribution is 25-50 nm. The particle size distribution of 0.9 g graphite added sample is in the range 30-55 nm with an average size of 40 nm. HRTEM image shows that the interplanar distance is 0.29 and 0.25 nm corresponds to α-Fe_2O_3 and γ-Fe_2O_3 respectively.

SAED pattern of 0.3 g graphite added sample gives diffraction rings from planes (104), (300), (024) related to α-Fe_2O_3, (201), (440) and (533) contributed to γ-Fe_2O_3. Similarly, SAED pattern of 0.6 g graphite added sample shows diffraction rings from the planes (048) and (104) related to α-Fe_2O_3. γ phase of Fe_2O_3 is also seen in 0.6 g graphite added sample evidenced by the diffractions ring from (521), (400) planes.

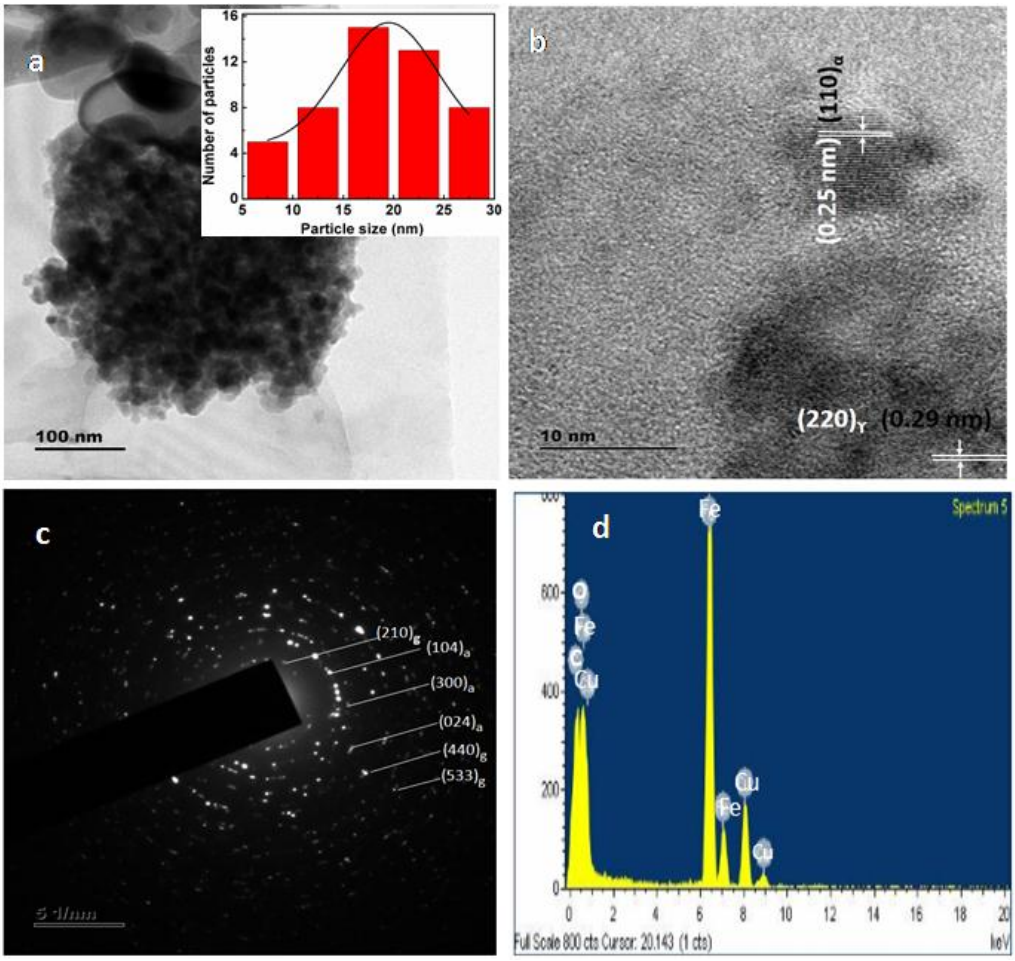

Figure. 6.4. *TEM images of α/γ-Fe_2O_3/graphite composite synthesized by combustion method with the addition of 0.3 g graphite in the precursor solution.*

The 0.9 g graphite added sample also shows diffraction ring from planes (110), (202) and (300) related to α-Fe_2O_3. This sample also shows diffraction planes (211), (130), (134) which is contributed to γ phase of iron oxide.

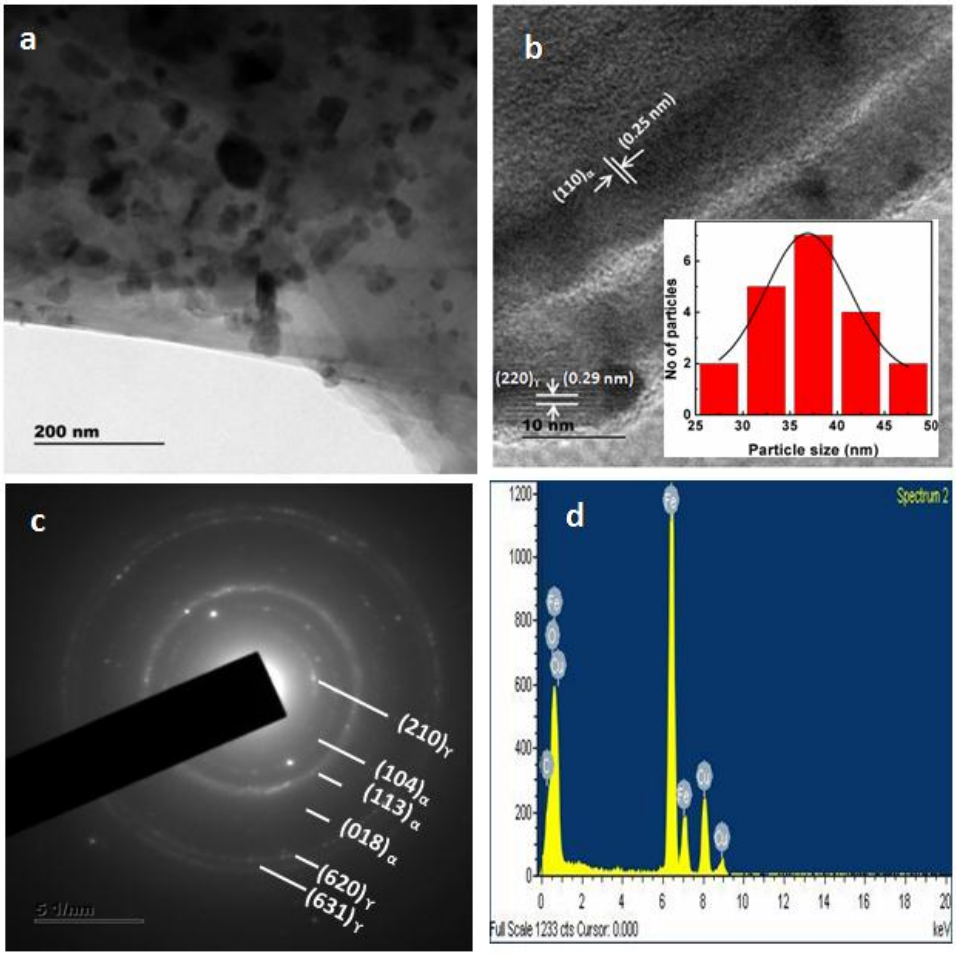

Figure. 6.5. *TEM images of α/γ-Fe_2O_3/graphite composite synthesized by combustion method with the addition of 0.6 g graphite in the precursor solution.*

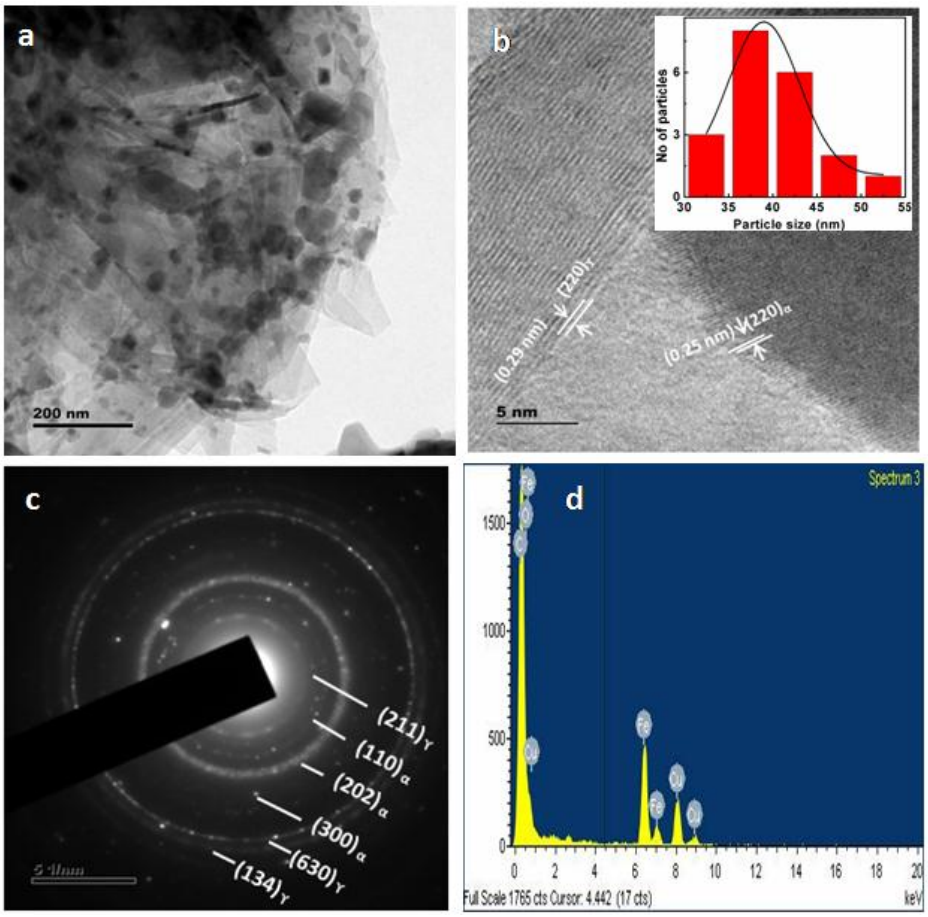

Figure. 6.6. *TEM images of α/γ-Fe_2O_3/ graphite composite synthesized by combustion method with the addition of 0.9 g graphite in the precursor solution.*

Optical band gap obtained with Kubelka-Munk function is 1.98, 1.99 and 1. 87 eV for 0.3, 0.6 and 0.9 g graphite added samples respectively (Figure 6.7) [Kubelka P; 1948, Kubelka P *et al*; 1931]. These optical band gap values indicate that these are semiconductors and comparable with one that of mixed phase of α and γ Fe_2O_3 [Syed F N *et al;* 2015]. Further, the presence of graphitic matrix for α, γ mixed phase of Fe_2O_3 are not making any appreciable change in the optical band gap of these materials.

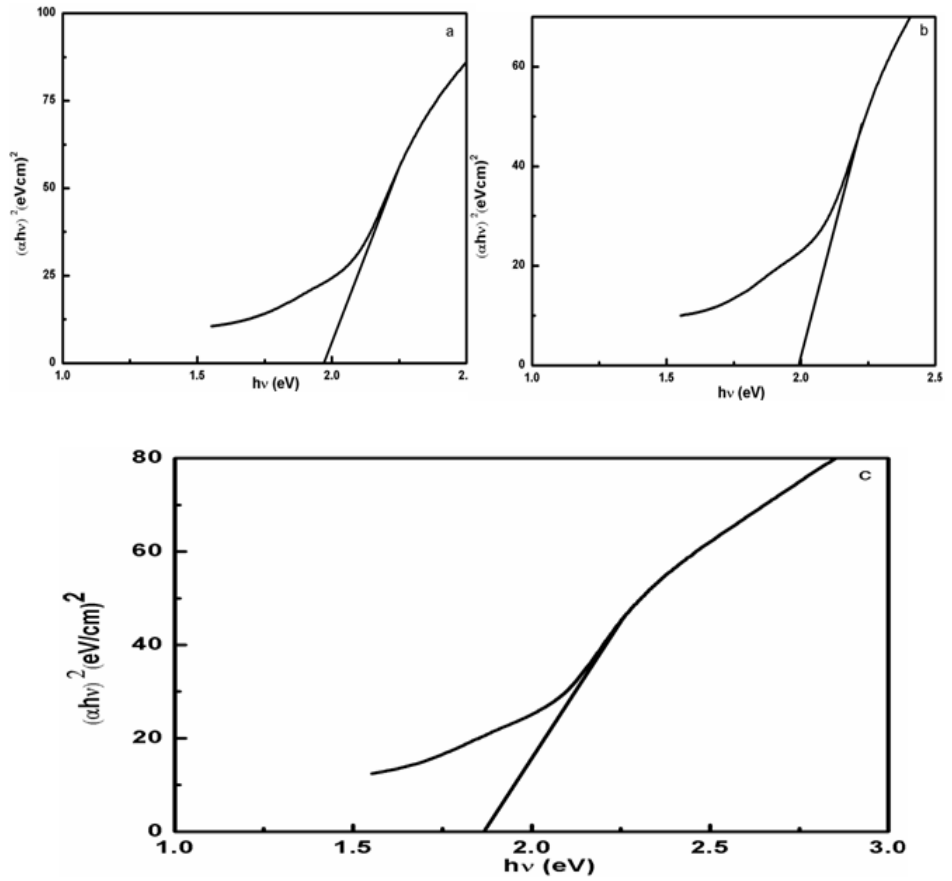

Figure. 6.7. *Tauc plot of α/γ-Fe_2O_3/ graphite composite synthesized by combustion method with the addition of (a) 0.3g (b) 0.6 g and (c) 0.9 g graphite in the precursor solution.*

Room temperature *dc* conductivity of 0.3 g and 0.6 g graphite added samples are 4.67×10^{-6} and 4.46×10^{-3} S/cm respectively. However, *dc* conductivity of 0.9 g graphite added sample is 9.71×10^{-2} S/cm which is more than other two samples at room temperature. All the samples show a negative slope in Arrhenius plot and its conductivity increase with respect to temperature, corresponds to semiconducting material. Activation energy calculated based on Arrhenius plot (E_a= slope x 0.8625) [Hassan A J *et al;* 2014] is 0.05, 0.007 and 0.0057 eV for 0.3, 0.6 and 0.9 g graphite added

samples respectively (Figure 6.8). The activation energy of these samples are decreases with increasing quantity of graphite. Similar observation is observed in CsPOMo/GO system with varying GO content [Huang M *et al;* 2017].

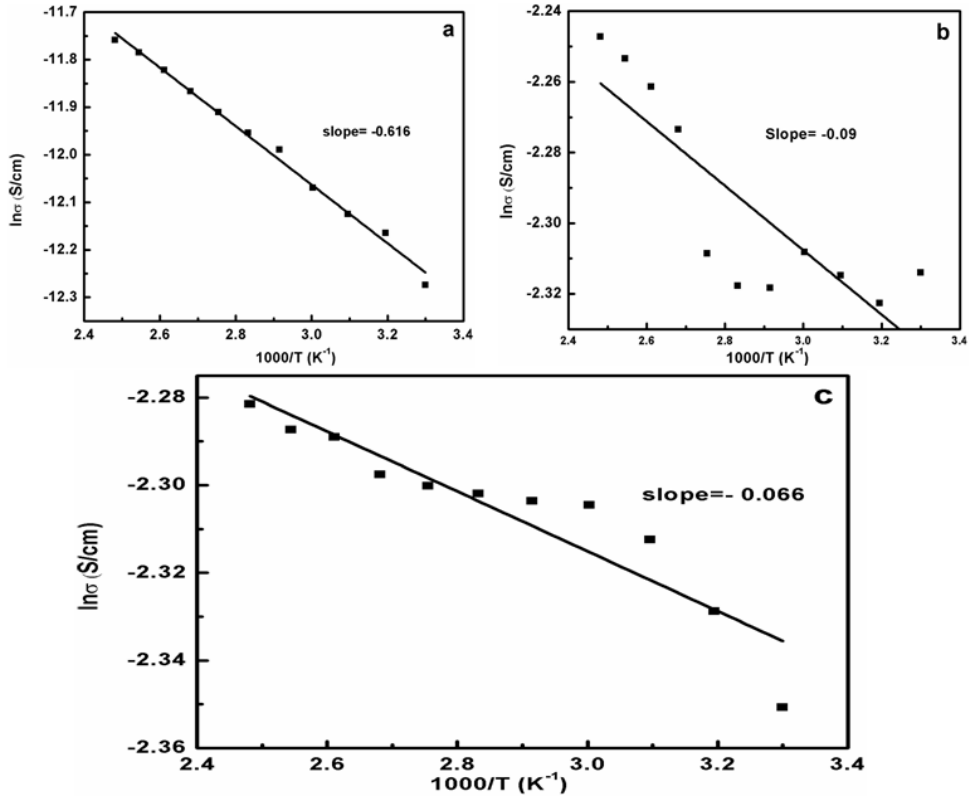

Figure. 6.8. *Arrhenius plot of α/γ-Fe_2O_3/graphite composite synthesized by combustion method with the addition of (a) 0.3 g (b) 0.6 g and (c) 0.9 g graphite in the precursor solution.*

Our XRD and TEM analysis shows that there exist combination of semiconducting iron oxide and conducting graphite (Figure. 6.1, 6.4, 6.5 and 6.6). The occurrence of conducting and semiconducting material together may give complicated conducting mechanism. The *dc* conductivity studies indicate that semiconducting type conductivity is dominant over conducting type conductivity of graphite. Since the percentage of graphite

in all samples are relatively less than that of semiconducting mixed phase of α and γ Fe_2O_3. Moreover the conducting channels of graphite may be broken due to the presence of α-Fe_2O_3 and γ-Fe_2O_3 grains. Increasing room temperature conductivity of samples with respect to quantity of graphite is probably due to the presence of more amount of conducting graphite.

Among the three samples, 0.3 and 0.9 g graphite added α/γ Fe_2O_3 are subjected to magnetic studies, in order to know its magnetic properties. The M-H curve of both sample at 5, 100, 200 and 300 K is saturating with respect to increasing field strength (Figure 6.9 and 6.11). Room temperature coercivity of both samples is around 174 Oe, higher than that of coercivity value (149 Oe) obtained for α/γ-Fe_2O_3 synthesized by combustion synthesis method (Chapter 5). Magnetic coercivity of both samples increases with lowering the measurement temperature may be related to increasing anisotropy attributed to the transition of weak ferromagnetic α-Fe_2O_3 to antiferromagnetic phase at its Morin transition temperature [Morin F J; 1950]. The room temperature magnetic remanence of sample grown with 0.3 g graphite added sample is about 6 emu/g. Remanent magnetisation of 0.9 g graphite added sample is decreased to 2.6 emu/g compared to 0.3 g graphite added sample. Room temperature magnetic saturation of 0.3 g and 0.9 g graphite added samples are 24 and 15 emu/g respectively (Table 6.1). These observed saturation magnetisation of both samples are less compared to α/γ-Fe_2O_3 and also found to be decreasing with increasing graphitic content.

The M-T curve of the sample under zero field cooling (ZFC) and field cooling (FC) with an applied field of 300 Oe meet around 300 K for both samples [Ann M H *et al;* 2017] (Figure 6.10 and 6.12). Magnetisation of samples gradually decreases with respect to temperature up to 50 K under ZFC condition. Below 50 K magnetisation values decreases on lowering the temperature of sample under zero field cooling condition.

Table 6.1. *Magnetic parameters of α/γ-Fe_2O_3/graphite composite synthesized by combustion method with the addition of 0.3 and 0.9 g graphite.*

Magnetic parameters	**0.3 g graphite added α/γ-Fe_2O_3**				**0.9 g graphite added α/γ-Fe_2O_3**			
	5 K	**100 K**	**200 K**	**300K**	**5 K**	**100 K**	**200 K**	**300 K**
H_C (Oe)	290	237	178	175	327	238	182	174
M_r (emu/g)	8	7.5	7.4	6	4.5	3.6	2.9	2.6
M_S (emu/g)	26.58	26.2	25.4	24	16.3	16	15.7	15

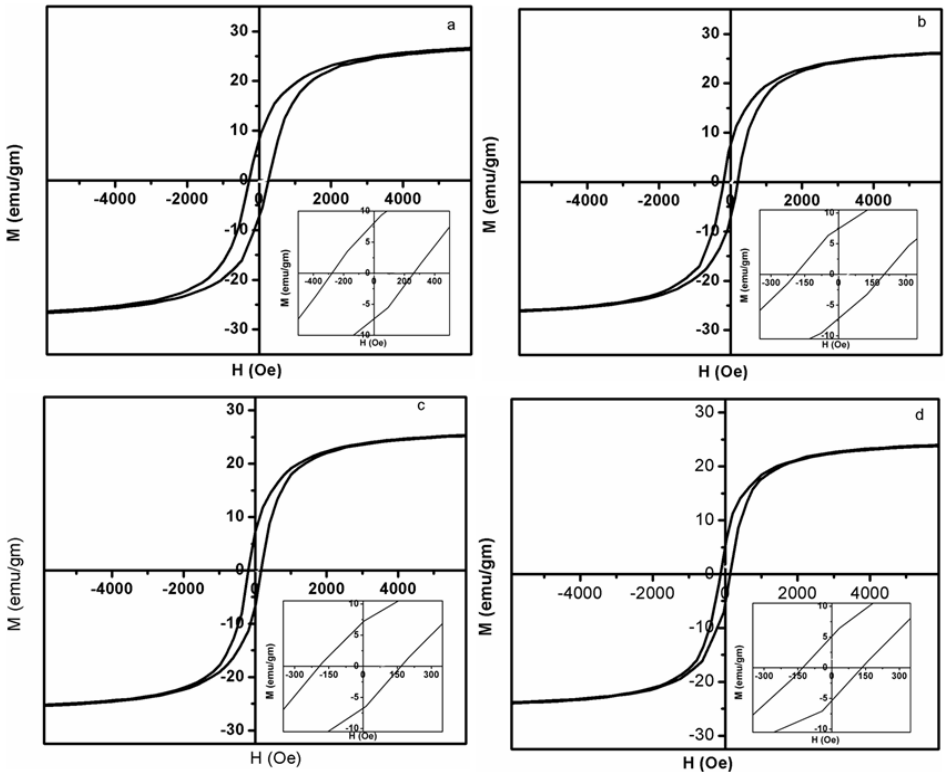

Figure. 6.9. *M-H curve of α/γ-Fe_2O_3/graphite composite synthesized by combustion method with the addition of 0.3 g graphite in the precursor salt (a) 5 (b)100 (c) 200 and (d)300 K.*

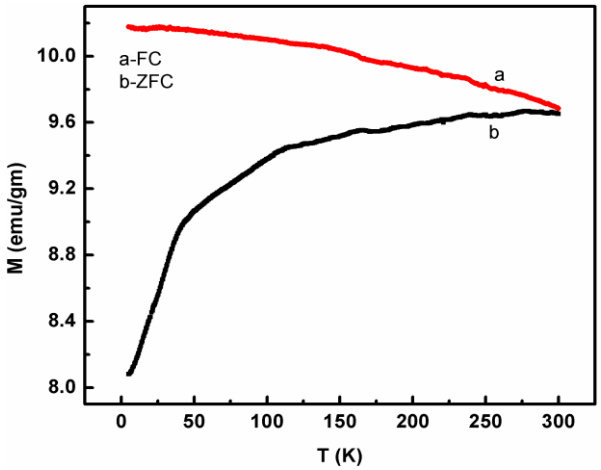

Figure. 6.10. *M-T curve of α/γ-Fe_2O_3/graphite composite synthesized by combustion method with the addition of 0.3 g graphite in the precursor solution (a) ZFC (b) FC.*

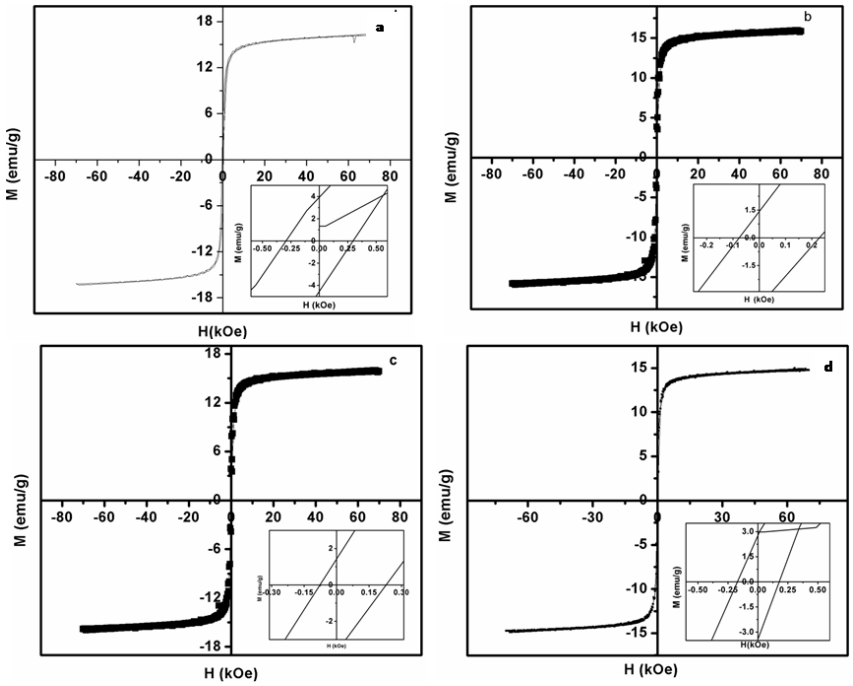

Figure. 6.11. *M-H curve of α/γ-Fe_2O_3/graphite composite at (a) 5 (b)100 (c) 200 and (d)300 K synthesized by combustion method with the addition of 0.9 g graphite in the precursor solution*

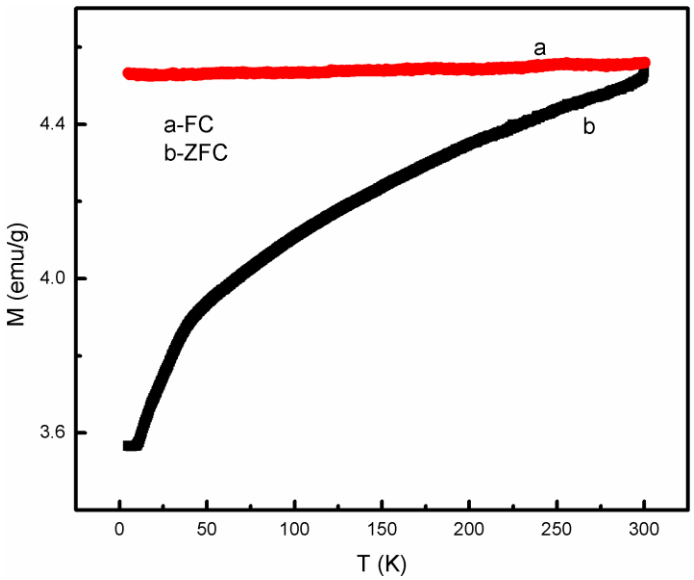

Figure. 6.12. *M-T curve of α/γ-Fe_2O_3/graphite synthesized by combustion method with the addition of 0.3 g graphite in the precursor solution (a) ZFC (b) FC.*

BET surface area of α/γ-Fe_2O_3/graphite composite (0.3 g) is 95.14 m^2/g with a pore radius of 1.73 nm (Figure 6.13) higher than that of reported one in α/γ-Fe_2O_3/graphene oxide [Santos T R T *et al;* 2017].

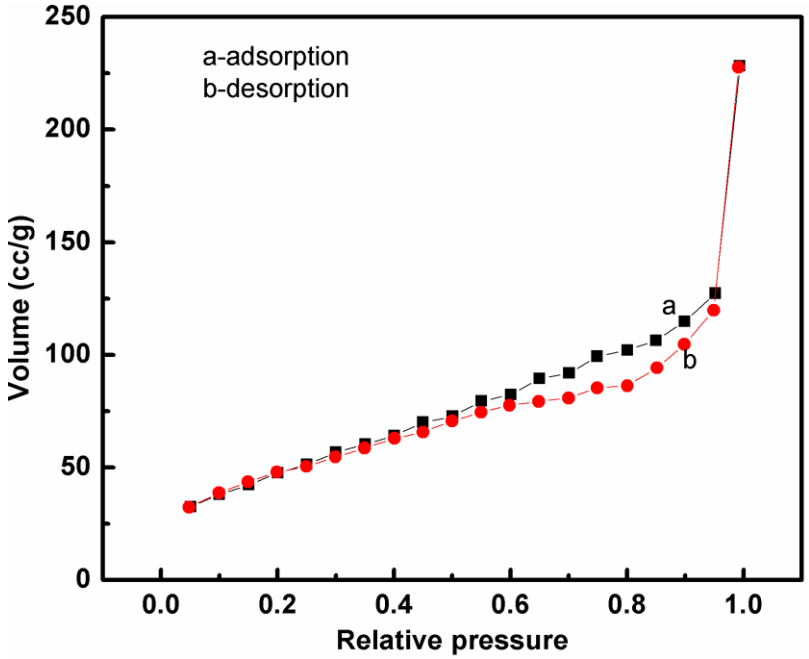

Figure. 6.13. *BET isotherm curve of α/γ-Fe_2O_3/graphite composite synthesized by combustion method with the addition of 0.3 g graphite in the precursor solution (a) adsorption and (b) desorption.*

6.3.1. Ni (II) ion adsorption study

Ni(II) ion removal efficiency is calculated using the standard formula (R_E) = ((A_s-A_t) / (A_s)) x 100 % [Dong Z *et al;* 2014], where, A_s is the absorbance of stock solution (0.1 M nickel acetate) at 387 nm (Ni(II)). A_t is the absorbance of nickel acetate solution after treating with α/γ-Fe_2O_3/graphite (0.3 g added) composite.

The Ni(II) removal efficiency of 0.3 g graphite added α/γ-Fe_2O_3 (6 mg/L) investigated in alkaline and acidic stock solution of nickel acetate. Initially, the experiment is carried out with 6 mg/L of adsorbent for a time of contact of 10 min. by varying the pH of the stock solution (0.1 M nickel acetate) from 1 to 8. Ni(II) ion removal efficiency is increase with respect to pH of the stock solution (Figure 6.14). Ni(II) removal efficiency in acidic medium (pH 1) is about 23.2 %, and 98 % in alkaline medium (pH 8). Adsorption experiments with more than pH 8 nickel acetate solution produces precipitates [Salmani M H *et al;* 2013]. Interestingly, the Ni(II) removal efficiency of the α/γ-Fe_2O_3/graphite (0.3 g) is increases with pH of the stock solution (nickel acetate). At lower pH, stock solution may have more H^+ ions, which react with anionic functional groups on the surface of iron oxide and graphite which restrict the available binding sites for nickel ion adsorption. When pH increases, adsorbent surface is less protonated, so available adsorption sites enhances which in turn increases the Ni(II) removal efficiency [Sen T K *et al;* 2002]. The observed higher order Ni(II) removal efficiency of sample in alkaline medium (pH 8) is due to formation of more electronegative surface charge in agreement with previous report [Hu J *et al;* 2006].

To find the effect of time of contact on the Ni(II) ion removal efficiency and equilibrium time of contact, the measurement is carried out by varying contact time (2, 4, 6, 8, 10, 20 and 30 min.) with adsorbent dosage (6 mg/L). In all the cases pH of the nickel acetate is maintained at 8. Ni(II) removal efficiency of α/γ-Fe_2O_3/graphite (0.3 g) increases with respect to time of contact up to 8 min. (Fig. 6.15), after that there is no appreciable effect. Above observation indicate that the adsorption of Ni(II)

ion on α/γ-Fe_2O_3/graphite (0.3 g) is a gradual process, that requires minimum time (equilibrium time of contact) to fill all adsorption sites in an adsorbent. In the present case obtained equilibrium time of contact is 8 min.

To know the effect of adsorbent dosage on Ni(II) removal efficiency of 0.3 g graphite added α/γ-Fe_2O_3 at equilibrium contact time (8 min.) with pH 8 of the stock solution, the adsorbent dosage is varied to 2, 4, 6, 8 and 10 mg/L. The Ni(II) removal efficiency is about 95 % with an adsorbent dosage of 2 mg/L α/γ-Fe_2O_3/graphite (0.3 g). The maximum Ni(II) removal efficiency (98 %) is obtained for 10 mg/L adsorbent dosage with 8 min. of time of contact and at a pH of 8. Further increase in the adsorbent dosage is not making any appreciable change in the Ni(II) removal property of the sample under investigation (Figure 6.16). Ni(II) adsorption removal efficiency of 0.3 g α/γ-Fe_2O_3 is higher than that of α/γ-Fe_2O_3. The BET surface area of 0.3 g graphite added α/γ-Fe_2O_3 is 95.14 m^2/g, which is more than that of α/γ-Fe_2O_3 (75.73 m^2/g). The increased Ni(II) adsorption removal efficiency of 0.3 g graphite added α/γ-Fe_2O_3 is contributed to the enhanced surface area.

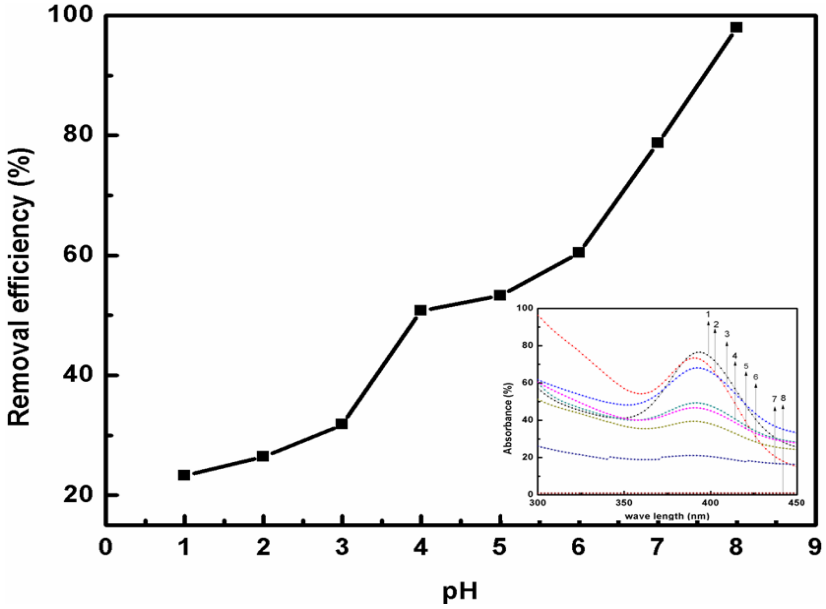

Figure. 6.14. *The effect of pH on Ni(II) removal from 0.1 M nickel acetate solution using 6 mg/L α/γ-Fe_2O_3/graphite (0.3 g) composite with a time of contact 10 min. Inset shows optical absorption spectra of stock solution after treated with 6 mg/L α/γ-Fe_2O_3/graphite (0.3 g)..*

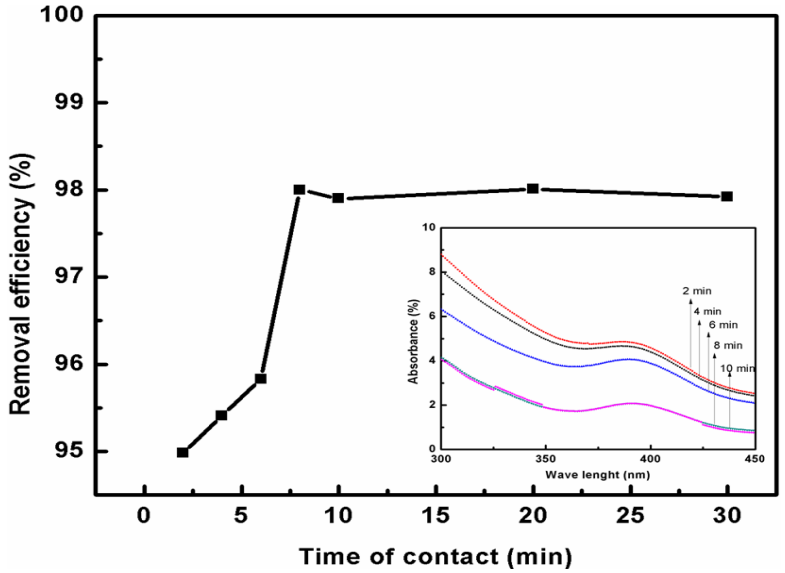

Figure. 6.15. *The Effect of contact time (min) on Ni(II) removal from 0.1 M nickel acetate solution (pH 8) by using 6 mg/L combustion synthesized α/γ-Fe_2O_3/graphite (0.3 g) composite. Inset shows optical absorption spectra of stock solution after treated with 6 mg/L α/γ-Fe_2O_3/graphite (0.3 g) with different contact time.*

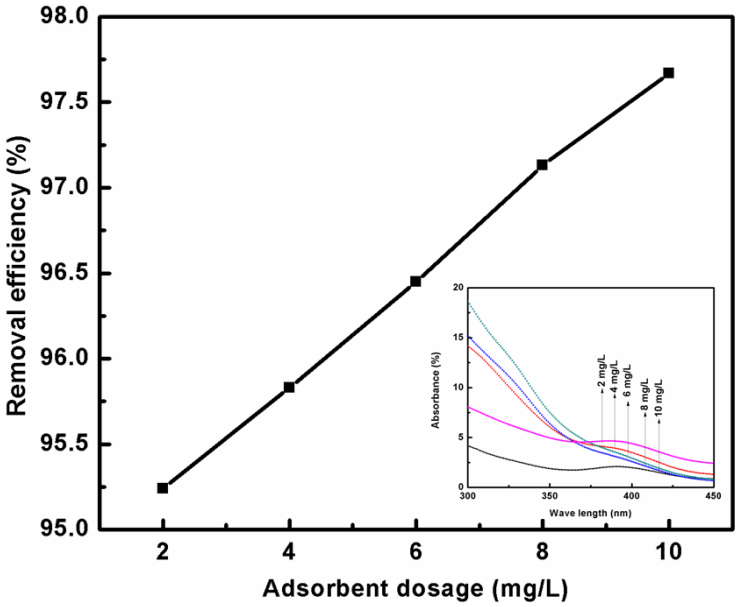

Figure. 6.16. *The effect of adsorbent dosage (2, 4, 6, 8, 10 mg/L) on Ni(II) removal from 0.1 M nickel acetate solution (pH=8) with constant time of contact (8 min) using combustion synthesized α/γ-Fe_2O_3/graphite (0.3 g). Inset shows optical absorption spectra of stock solution after treated with α/γ-Fe_2O_3/graphite (0.3 g) different dosage.*

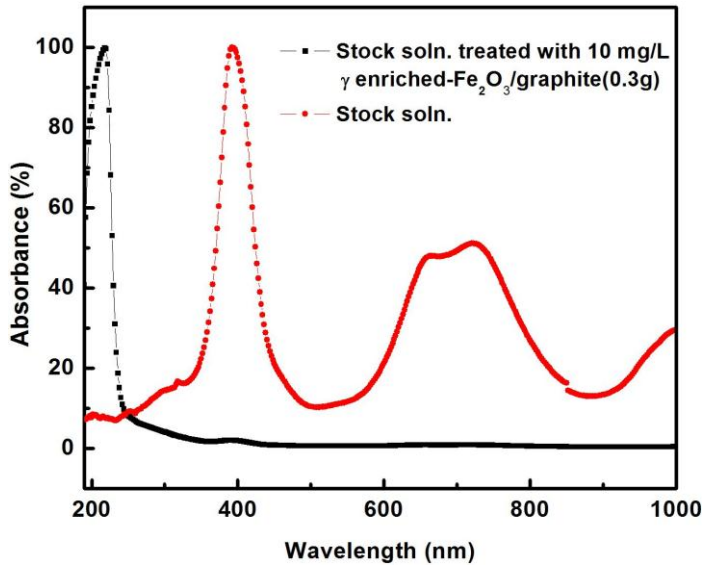

Figure. 6.17. *Optical absorption spectra of (a) stock solution (0.1 M nickel acetate) and (b) stock solution after treating with combustion synthesized α/γ Fe_2O_3/graphite (0.3 g) composite (10 mg/L) at pH 8 for a time of contact 8 min.*

6.4. Conclusions

Mixed phases of α and γ Fe_2O_3 nanoparticles in graphitic matrix (0.3, 0.6, 0.9 g) can be synthesized by combustion method with the precursor salts of iron oxide and graphite. The samples show band gaps similar to that of mixed phases of α and γ Fe_2O_3, which indicate that the presence of graphite in these sample could not disturb the band structure of iron oxide. The dc conductivity studies showed that the samples are semiconducting in nature. The magnetic remanence and saturation of the samples are found to decrease with increase in the quantity of graphite added to the precursor salt before the synthesis. 0.3 g graphite added α/γ Fe_2O_3 showed 98 % Ni(II) removal efficiency from 0.1 M nickel acetate solution, which is higher than that of α/γ Fe_2O_3 nanoparticles. Enhanced Ni(II) adsorption property of 0.3 g graphite added α/γ-Fe_2O_3 is related to the increase in the surface area of the material as understood from BET measurement. Thus, α/γ-Fe_2O_3 graphite magnetic system can be effetively used for the removal of toxic Ni(II) ion from the nickel contaminated water.

Chapter 7

Summary and future scope of the present work

Contents

7.1. Summary of the present work

Synthesis of iron based nano and microstructures has got great attention in the past a few years. Iron oxide nano and micro structures shows superior physical properties compared to its bulk counterpart make it as more efficient choice for medical and water treatment applications. Iron oxide has semiconducting nature with band gap of nearly 2 eV which is suitable for photocatalytic and gas sensing applications. Iron oxide exhibits ferromagnetic property at room temperature, this property is particularly useful for magnetic storage and medical applications. Iron oxide with relatively large surface area are good for heavy metal ion adsorption removal from the contaminated water. Interestingly, the magnetic property ensures easy magnetic separation of heavy metal ion adsorbed iron oxide after treatment. The magnetic and adsorption property of iron oxide can be improved by incorporating it in carbaneous matrix. This thesis deals with the synthesis and magnetic properties of iron oxide and iron oxide in graphitic matrix, adsorption removal of Ni(II) ion from contaminated system.

Solvothermal synthesis method can be effectively used to control size, shape and crystalline defects in hematite crystals with different solvent combination of precursor solution. Size, shape and population of oxygen vacancies will contribute to variation in optical, *dc* conductivity and magnetic properties of solvothermaly grown spheroid shaped hematite crystals. The enhanced room temperature magnetic coercivity (5.23 kOe) observed in spheroid and pseudocubic micro crystals (6.16 kOe) is contributed to shape anisotropy and defect related spin pinning effects. The inhomogeneous particle distribution in spheroid shaped sample grown with methanol leads to the appearance of high intensity UV absorption peaks and two Morin transition temperatures at 189 and 243 K. The variation in number of oxygen vacancies leads to the shifting of Morin transition temperature of the spheroid and pseudocubic hematite samples compared to its bulk haematite. The morphology dependant optical and magnetic properties presented in this study provide information about the optimisation of synthesis condition of new hematite micro structures for future technological applications.

Graphene oxide and α-Fe_2O_3 combined system is an interesting combination of materials for various technological applications. Spherical shaped α-Fe_2O_3/GO nanocomposites synthesized with GO and precursor salts of α-Fe_2O_3 in acetonitrile medium shows disorder than GO as revealed by the Raman studies. The electronic structure of GO is not interacting with the band structure of α-Fe_2O_3. Optical band gap of α-Fe_2O_3/GO are comparable to semiconductors, room temperature electrical conductivity similar to that of semiconducting materials. Magnetic coercivity of α-Fe_2O_3 is increased on lowering the temperature of the sample to 5 K due to frozen

canted spin. The interactions of the conducting electrons of carbonaceous material with "d" electrons of the metal oxide leads to increase in anisotropy (RKYY interaction). The slight increase in magnetic coercivity of α-Fe_2O_3/GO with respect to α-Fe_2O_3 at room temperature and enhancement at 5 K is synergetic effect attributed to RKKY interactions between 'd' electrons of α-Fe_2O_3 and the conducting electrons of GO. The presences of super-paramagnetic graphene oxide contribute to increase in remanence and saturation magnetisation of α-Fe_2O_3/GO. The thermal hysteresis at Morin transition temperature of the order of 11 K, is observed in α-Fe_2O_3/GO nanocomposites due to the presence of GO.

Citric acid is one of the important fuel used in the combustine synthesis of oxide materials and metallic chloride as oxidiser. Oxidizer to fuel ratio is one of the important parameter which determines formation of different phases of iron oxide. α/γ-Fe_2O_3 with different phases can be synthesized by varying oxidizer to fuel ratio. α/γ-Fe_2O_3 nanocomposite are exhibiting semiconducting behaviour with band gap of 2 eV. Magnetic coercivity and magnetic saturation of the samples increased with respect to γ-Fe_2O_3 content in the α/γ-Fe_2O_3 nanocomposite. The higher amount of citric acid gives sample with more content of γ-Fe_2O_3. Lower value of magnetic saturation in both sample compared to bulk γ-Fe_2O_3 is attributed to crystalline vacancies in the α/γ-Fe_2O_3 nanocomposite. α/γ-Fe_2O_3 nanocomposite can be utilized as a material choice for the adsorption removal of about 90% Ni(II) from the nickel acetate solution with a short time of 8 min. The higher order adsoption removal of α/γ-Fe_2O_3 nanocomposite due to its higher surface area (75 m^2/g) and also contributed to crystalline defects in the nanocomposite. α/γ-Fe_2O_3 nanocomposite with

room temperature coercivty is a suitable material for removing heavy metal ions from contaminated water and the α/γ-Fe_2O_3 nanocomposite can be collected back from the treated solution with magnets.

α and γ-Fe_2O_3 nanoparticles embedded in graphitic matrix is a ferromagnetic functional material. Mixed phase of α and γ Fe_2O_3 nanoparticle in graphitic matrix (0.3, 0.6, 0.9 g) can be synthesized by combustion method with the precursor salt of iron oxide and graphite in aqueous medium. The optical band gap of the samples is similar to that of mixed phase α and γ Fe_2O_3. More amount of graphite in the growth medium leads to the reduction of magnetic coercivity of α/γ-Fe_2O_3 graphitic system. The α/γ-Fe_2O_3 nanoparticles are having average size of 57 nm, the enhanced Ni(II) adsorption property of 0.3 g graphite added α/γ-Fe_2O_3 is related to increase in surface area (95 m^2/g) of the material as revealed from BET measurement.

7.2. Future scope

In the present study, pseudocubic and spheroid microstructures with high coercivity are synthesized by using methanol, propanol, methanol:water and propanol:water solvents or solvent combinations for the preparation of solution of precursor salt. Changing the solvent, solvent combination, molarity of the solvent, quantity of the solvent etc. will contribute to morphology, size, shape, crystalline defects and vacancies etc. ofcourse by changing the solvent used for the synthesis process, one can effectively change the morphologies and morphology dependent magnetic properties, which will be very useful for high coercive magnetic applications. The synthesized micro crystallites of hematite samples had

semiconducting nature, which can be used for photocatalysis and gas sensing applications. The porous hematite microstructures with more photocatlytic and gas sensing properties can be grown by changing the solvothermal reaction conditions. The *dc* conductivity, magnetic properties and heavy metal ion adsorption properties of iron oxide can be enhanced by optimizing the suitable solvent combination for the growth of these materials. An attempt can be made to improve the above mentioned properties of iron oxide by embedding it in graphite matrix. Further, the growth of iron oxide nanoparticles in the nano regime (with size less than 10 nm) can be achieved by changing solvent and temperature combination of the reaction system.

Further, the combination of iron oxide and CNT, MWCNT, graphene, reduced grapheme oxide systems are another interesting group of compounds. All these materials can be made in to thin films either by spin coating or by pulsed laser deposition. Synthesis of α-Fe_2O_3 nanoparticles in oxygen free acetonitrile solvent in inert atmosphere can effectively minimise the oxygen related impurities, which will ensure high purity for the synthesised samples for various applications. So this is an important research topic with wide future scope. γ enriched mixed phase α/γ-Fe_2O_3 is prepared by changing the oxidizer (Iron(III) chloride) to fuel (Citric acid) ratios during combustion process. Combustion synthesis method employed in this work for the preparation of mixed phase of α and γ-Fe_2O_3, which is cost effective and industrially scalable method for the large scale synthesis. Since γ-Fe_2O_3 is more ferromagnetic compared to α-Fe_2O_3, the synthesis of single phase γ-Fe_2O_3 for the magnetic storage applications is an interesting area; by optimising the combustion synthesis parameters, single phase

γ-Fe_2O_3 can be synthesized in large scale. The magnetic nanoparticles can be easily separated by using magnet from treated water in purification process after adsorption of impurities; this makes it highly suitable for water purification applications. α/γ-Fe_2O_3 and graphite added α/γ-Fe_2O_3 are found to be efficient material for Ni(II) adsorption removal from 0.1 M nickel solution. The adsorption efficiency of α/γ-Fe_2O_3 and graphite added α/γ-Fe_2O_3 can be investigated for the removal of heavy metal ions such as Cd(II), Hg(II), Co(II), As(III) etc. from contaminated water. Since iron oxide is nontoxic, the waste water purification using iron oxide nanoparticles is a promising method to solve water scarcity. So investigation of adsorption efficiencies of magnetic iron oxide is an important research area.

Further, the combination of iron oxide and CNT, MWCNT, graphene, reduced graphene oxide systems can be made in to thin films either by spin coating or by pulsed laser deposition. These magnetic thin films are expected to be very useful for magnetic data storage application and for the fabrication of spin valves etc. Magneto resistance studies of iron oxide in graphite or CNT systems is an interesting area of research in future.

.....ꕥ.....

Abbreviations

ATR	-	Attenuated Total Reflection
BET	-	Brunauer-Emmett-Teller analysis
Cd(II)	-	Cadmium ion
CTAB	-	Cetyl Trimethyl Ammonium Bromide
DRS	-	Diffused Reflectance Spectra
EDAX	-	Energy Dispersive Analysis of X-Ray
FC	-	Field Cooling
Fe_3O_4	-	Magnetite
$FeCl_3$	-	Iron (III) Chloride
FE-SEM	-	Field Emission Scanning Electron Microscope
FTIR	-	Fourier Transform Infra Red spectra
GO	-	Graphene Oxide
HEPES	-	Hydroxy ethyl piperazine ethane sulfonic acid
HNO_3	-	Nitric Acid
HRTEM	-	High Resolution Transmission Electron Spectroscopy
ICP-AES	-	Inductive coupled plasma-atomic emission spectroscopy
ICP-MS	-	Inductive coupled plasma mass spectrometer
JCPDS	-	Joint Committee for Powder Diffraction
MB	-	Methylene Blue

MRI - Magnetic resonance imaging

NaOH - Sodium Hydroxide

Ni(II) - Nickel ion

Pb(II) - Lead ion

PEG - Poly Ethylene Glycol

PID - Proportional Integral Derivative

PPMS - Physical Property Measurement System

RB5 - Reactive Black 5

rGO - Reduced Graphene Oxide

RhB - Rhodamine Blue

SAED - Selected Area Electron Diffraction

SEM - Scanning Electron Microscopy

SHS - Self propagating High temperature Synthesis

SQUID - Superconducting Quantum Interference Device

TEM - Transmission Electron Microscopy

UV - Ultra Violet

VSM - Vibrating Sample Magnetometer

XRD - X-Ray Diffraction

ZFC - Zero Field Cooling

α-Fe_2O_3 - Hematite

γ-Fe2O3 - Maghemite

.....ಠಠ.....

References

[1] Ahmed M A, Ali S M, El-dek S I, Galal A, Mater. Sci. Eng. B, **178**, 744 (2013).

[2] Aigu L L, Rodrigues J N B, Su C, Milletari M, Loh K P, Wu T, Chen W, Neto A H C, Adam S, Wee A T S, Sci. Rep., **5**, 11430 (2015).

[3] Akbar S, Hasanain S K, Azmat N, Nadeem M, Conden. Mat., **480**, 1 (2004).

[4] Al-Bayati F A, Annal. Clin. Microbio. Antimicrob., **8**, 20 (2009).

[5] Almeida T P, Fay M W, Zhu Y, Brown P D, Nanoscale., **2**, 2390 (2010).

[6] An Z, Zhang J, Pan S, Yu F, J. Phys. Chem. C, **113**, 8092 (2009).

[7] Ann M H, Monika K, David H, Alexander K, Molecules, **22**, 2204 (2017).

[8] Asuha S, Gao Y W, Deligeer W, Yu M, Suyala B, Zhao S, J. Porous. Mater., **18**, 581 (2011).

[9] Ayachi A A, Mechakara H, Silva M M, Boudjaadar S, Achour S, Ceram. Int., **41**, 2228 (2015).

[10] Bai S, Chen S Q, Shen X, Zhu G, Wang G, RSC Adv.,**2**, 10977 (2012).

[11] Banwell C N, Cash E M M, Fundamentals of molecular spectroscopy, Tata McGraw Hill, 4th edition, (1994).

[12] Barinova T V, Boroviaskaya I P, Int. J. Self-Propag. High-Temp Synth., **21**, 1 (2012).

[13] Baumanis C, Bloh J Z, Dillert R, Bahnemann D W, J. Phys. Chem. C,**115**, 25442 (2011).

[14] Bercoff P G, Bertorello H R, Appl. Phys. A, **100**, 1019 (2010).

[15] Bharathi S, Nataraj D, Seetha M, Mangalaraj D, Ponpandian N, Masuda Y, Senthil K, Yonoj K, Cryst. Eng. Comm., **12**, 373 (2010).

[16] Bhuvaneswari S, Pratheeksha P M, Anandan S, Rangappa D, Gopalan R, Rao T N, Phys. Chem. Chem. Phys., **16**, 5284 (2014).

[17] Bogeat A B, Franco M A, Gonzalez C F, Gonzalez J S, Serrano V G, Phys. Chem. Sol. **87**, 259 (2015).

[18] Bogeat A B, Franco M A, Gonzalez C F, Gorcia A M, Serrano V G, Phy. Chem. Chem. Phys., **16**, 25165 (2014).

[19] Bonard J M, Seraphin S, WegroweJ E, Jiao J, Chatelain A, Chem. Phys. Lett., **343**, 251 (2001).

[20] Bourlinos A B, Karakassides M A, Petridis D, J. Phys. Chem. B, **104**, 4375 (2000).

[21] Byrappa K, Adschiri T, Prog. Cryst. Growth Charact. Mater., **53**, 117 (2007).

[22] Can M M, Firat T, Ozcan S, Physica B, **406**, 2483 (2011).

[23] Cao Z, Qin M, Jia B, Gu Y, Chen P, Volinsky A A, Qu X, Ceram. Int., **41**, 2806 (2015).

[24] Cesar I, Kay A, Martinez J A G, Gratzel M, J. Am. Chem. Soc., **128**, 4582 (2006).

[25] Chakrabarty S, Chatterjee K, J. Cryst. Growth, **381**, 107 (2013).

[26] Chakrabarty S, Jana T K, De K, Das S, Dey K, Chatterjee K, Mater. Res. Express, 1, 046104 (2014).

[27] Chaudhari N K, Kim H C, Kim C S, Park J, Yu J S, Cryst. Eng. Comm., **14**, 2024 (2012).

[28] Chen H, Zhao Y, Yang M, He J, Chu P K, Zhang J, S Wu, Analytica. Chimica. Acta., **659**, 266 (2010).

[29] Chesnel K, Trevino M, Cai Y, Hancock J M, Smith S J,Harrison R G, J. Phy.,**521**, 12004 (2014).

[30] Chikazumi S, Taketomi S, Ukita M, Mizukami M, Miyajima HSetogawa M, Kurihara Y, Phys. Mag. Fluid., J. Magn. Magn. Mater., **65**, 245 (1987).

[31] Chirita M, Grozescu I, Chem. Bull. Politehnica. Univ., **54**, 1 (2009).

[32] Chun L, WuX, LouX, ZhangY, Electrochim. Acta., **55**, 3089 (2010).

[33] Chung D D L, J. Mater. Sci., **37**, 1475(2002).

[34] Coey J M D, Magnetism and magnetic materials, Cambridge University Press, New York, 1st edition, (2010).

[35] Cornell R M, Schwertmann U, The iron Oxides: structure, properties, reactions, occurences and uses, Willey-VCH, Heppenheim, 2nd edition, 694 (2003).

[36] Costa G M D, San E V, Grave E D, Vandenberghe R E, Barron V, Datas L, Phy. Chem. Minerals, **29**, 122 (2002).

[37] Culity B D, Graham C D, Introduction to magnetic materials, John Wiley and Sons, New Jersey, 2nd edition, (2009).

[38] Dekker A J, Solid state physics, Mcmillan publicatishers limited, (1981).

[39] Demir V, Celik F, Ates M, Bogatu C , Arslan Z , Camas M, Can S S, Bull. Environ. Contam. Toxicol., **95**, 752 (2015).

[40] Deraz N M, Alarifi A, Ceram. Int., **38**, 4049 (2012).

[41] Deshpande K, Mukasyan A, Varma A, Chem. Mater., **16**, 4896 (2004).

[42] Dieny B, Speriousu V S, Perkin S S P, Gurney B A, Wilhoit P R, Mauri D, Phys. Rev. B, **43**, 1297 (1991).

[43] Dikio E D, Nelana S M, Isabirye D A, Ebenso E E, Int. J. Electro. Chem. Sci., **7**, 1101 (2012).

[44] Dong Q, Wang D, Yao J, Kumada N, Kinumora N, Takei T, Yonesak Y, Cai Q, J. Cer. Society of Japan, **117**, 245 (2009).

[45] Dong Z, Wang D, Liu X, Pei X, Chen L, Jin J, J. M. Chem. A, **2**, 5034 (2014).

[46] Dunlop D J, Ann. Geophys., **27,** 269 (1971).

[47] Eggleston C M, Hochella M F, Am. Mineral., **77,** 911 (1992).

[48] Fassel V A, Peterson C A, Abercrombie F N, Kniseley R N, Anal. Chem., **48**, 516 (1976).

[49] Fernández-García M P, Gorria P, Blanco J A, Phy. Rev. B, **8**, 094418 (2010).

[50] FerrariA C,RobertsonJ, Phy. Rev. B, **61**, 14095 **(**2000).

[51] Flewitt P E J, Wild R K, Physical methods for materials characterization, IOP Publishing Ltd., (2003).

[52] Foner S, Rev. Sci. Instrum., **30**, 548 (1959).

[53] Frandsen C, Mørup S, Phy. Rev. Lett., **94**, 027202 (2005).

[54] Ganachari S V, Joshi V K, Salimath B, Deshpande R, Rao N V S, Venkataraman A, Int. J. Sci. Res., **1**, 77 (2012).

[55] Garcia M P F, Gorria P, Blanco J, Fuertes A B, Sevilla M, Boada R, Chaboy J, School D,

[56] Goya G F, Veith M, Rapalavicuite R, Shen H, Mathur S, Appl. Phys. A, **80**, 1526 (2005).

[57] Gramm K, Lundgren L, Beckman O, Physica scriptra, **13**, 2 (2008).

[58] Greneche J M, Phy. Rev. B 81, 094418 (2010).

[59] Guivar J A R, Martinez A I, Anaya A O, Valladares L D L S, Felix L L, Dominguez A B, Adv. Nanopart., **3**, 114 (2014).

[60] Guo X, Zhu H, Si M, Jiang C, Xue D, Li Q, Cryst. Eng. Comm., **15**, 8306 (2013).

[61] Guo S, Zhang G, Guo Y, Yu J C, Carbon, **60**, 437 (2013).

[62] Gupta A K, Gupta M, Biomaterial, **26**, 3995 (2005).

[63] Haering R R, Wallace P R**,** J. Phys. Chem. Solids Pergamon Press, **3**, 253 (1957).

[64] Hansen M F, Morup S, J. Mag. Mag., Mater., **203**, 214(1999).

[65] Hassan A J, J. Modern Phys., **5**, 2184 (2014).

[66] Hayashi H, Hakuta Y, Materials, **3**, 3794 (2010).

[67] He K, Xu C Y, Zhen L, Shao W Z, Mater. Lett., **62**, 739 (2008).

[68] He Y P, Miao Y M, Li C R, Wang S Q, Cao L, Xie S S, Yang G Z, Zou B S, Burda C, Phys. Rev. B, **71**, 125411 (2005).

[69] Hew G P, General introduction to transmission electron microscopy (TEM), Wiley and Sons, USA, 1(2011).

[70] Host J J, Block J A, Parvin K, Dravid V P, Alpers J L,Sezen T, Duca R L, J. Appl. Phys.,**83**, 793 (1998).

[71] Hou L, Li Q, ZhaO H, Yu L, Gao S, Zhao J, Sens. Actuators B, **107**, 915 (2005).

[72] Hu J, Chen G, Lo I M C, Asce M, J. Environ. Eng., **132**, 709 (2006).

[73] Huang M, Huang X, Fei M, Sun J, Deng Y, Xu C, Cheng J, Int. J. Electrochem. Sci., **12,** 240 (2017).

[74] Hummer B W S, Offeman R E, J. Am, Chem. Soc., **80**, 1339 (1958).

[75] Hyeon T, Seong L S, Park J, Chung Y, Na H B, J. Am. Chem. Soc. **123**, 12798 (2001).

[76] Iglesias, Battle X, Labarta A, J. Nanosci. Nanotechnol., **8**, 2761 (2008).

[77] Ingle J D, Crouch S R, Spectrochemical Analysis, Prentice Hall Int., New Jersey, (1988).

[78] Jahagirdar A A, Dhananjaya N, Monika D L, Kesavulu C R, Nagubhushana H, Sharma S C, Nagubhushana B M, Shivakumara C, Rao J L, Chkradhar K P S, Mol. Biomol. Spectrosc., **104**, 512 (2013).

[79] Jainski J, Pinkerton K E, Kennedy I M, Leppart V J, Sens. Actuators, **109**, 19 (2005).

[80] Jia B, Gao L, Sun J, J. Am. Soc., **90**, 1315 (2007).

[81] Jing Z H, Wu S H, J. Solid State Chem., **177**, 1213 (2004).

[82] Kannan M K, Fundamentals and applications of magnetic materials, Oxford University Press, UK, 1st edition, (2016).

[83] Kayani Z N, Arshad S, Riaz S, Naseem S, IEEE Trans Magnetics, **50**, 8 (2014).

[84] Kittel C, Introduction to solid state physics, Wiley Eastern Limtd., (1996).

[85] Knobel M, Nunes W C, Socolovsky L M, Biasi E D, Vargas J M, Denardin J C, J. Nanosci. Nanotechnol., **8**, 2836 (2008).

[86] Kocijanic S, Sullivan C O, Phys. Educ. **39**, 69 (2004).

[87] Korson L, Drost-Hansen W, Miller F J, J. Phy. Chem., **73**, 34 (1969).

[88] KovziridzeZ, KhoravaP, MitskevichN, J. Cancer Ther., **4**, 1262 (2013).

[89] Kubelka P, J. Opt. Soc. Am., **38**, 448 (1948).

[90] Kubelka P, Munk F,Zh. Tekh. Fiz, **12**, 593 (1931).

[91] Lagashetty A, Vijayanand H, Basavaraja S, Mallikarjuna N N, Venkataraman A, Bull. Mater. Sci., **33**, 1 (2010).

[92] Laidler K, J.Trans. Faraday Soc., **55**, 1725 (1959).

[93] LasernaJ, An introduction to Raman spectroscopy: introduction and basic principles, spectroscopy, now. com, Wiley, (2001).

[94] Lee J B, Kim H J, Luznik J, Jelen A, Pajic D, Wencka M, Jaglicic Z, Meden A, Dolinsek, J. Nanomater., **9**, 902968 (2014).

[95] Li H, Lu Z, Li Q, So M H, Chen C M, Chen R, Chem. Asian J., **6**, 2320 (2011).

[96] Li W, Zho M, Xia Y, Zhang R, Mu Y, J. Mater. Chem., **19**, 9274 (2009).

[97] Li Z, Lai X, Wang H, Mao D, Xing C, Wang D, Nanotechnol., **20**, 1 (2009).

[98] Lian J, Duan X, Ma J, Peng P, Kim T, Zheng W, ACS Nano, **3**, 3749 (2009).

[99] Lian S, Li H, Kang Z, Liu Y, Lee S T, J. Sol. State Chem., **185**, 117 (2012).

[100] Liang H F, Wang Z C, Mater. Lett., **64**, 2410 (2010).

[101] Liou S C, Chen S Y, Liu D M, Biomaterials, **24**, 3981 (2003).

[102] Liu K, Wang H, Wu Q, Zhao J, Sun Z, Xue S, J. Power Sources, **283**, 381 (2015).

[103] Liu Z, Baoling L V, Wu D, Sun Y, Particuology, **101**, 456 (2012).

[104] Lu A H, Salabas E L, Schuth F, Angew. Chem. Int. Ed., **46**, 1222 (2007).

[105] Luna C, Vege V, Prida V M, Resendez R M, J. Nanoscie. Nanotech., **12,** 7571 (2012).

[106] Lyubutin I S, Frolov*a* K V, Anosova*a* O A, Pokatilov V S, Okotru A V, Kudashov A G, Yu V S, Bulusheva L G**,** J. Exp. Theor. Phys., **109**, 254 (2009).

[107] Ma J, Zhang X, Chen K, Li G, Xiaodong H, J. Mater. Chem. A, **1**, 5545 (2013).

[108] Machala L, Tucek J, Zboril R, Chem. Mater., **23**, 3255 (2011).

[109] Marcos J S, Marco M A L, Morillas R M, C´espedes E, Villacorta F J, Men´endez N, Prieto C, J. Phys. Condens. Matter., **23**, 476003 (2011).

[110] Margarethe H A, Brigitte V R, Heinrich H, Nanostruct. Mater. Biomed. Appl., **120**, 1 (2009).

[111] Martinez A I, Lobato M A G, Perry D L, Nova Sci. Publishers Inc., **978**, 184 (2009).

[112] Mathew J, Jothi N S N, Int.J. Appl. Bioeng., **9**, 36 (2015).

[113] Matsui K, Kyotani T, Tumita A, Mol. Cryst. Liq. Cryst., **1**, (387) 2017.

[114] Mihoc G, Ianos R, Pacurariu C, Lazau I, J. Thermal. Annal. Calorim., **1112**, 391 (2013).

[115] Mirzaei A, Janghorban K, Hashemi B, Hosseini S R, Bonyani M, Leonardi S G, Bonavita A, Neri G, Proess. Appl. Ceram., **10**, 209 (2016).

[116] Mitra S, Das S, Mandal K, Chaudhuri S, Nanotechnol., **18**, 275608 (2007).

[117] Mokdad F, Chen D L, Liu Z Y, Xiao B L, Ni D R, Ma Z Y, Carbon, **104**, 64 (2016).

[118] Morales M P, Verdaguer S V, Montero M I, Serna C J. Chem. Mater., **1**, 13058 (1999).

[119] Morin F J, Phy. Rev., **78**, 819 (1950).

[120] Moskowitz B M, Hitchhiker's guide to magnetism, Environmental magnetism work shop, The Institute for Rock Magnetism and the Global Paleorecords Research Training Group, 1 (1991).

[121] Muthukrishnaraj A, Vadivel S, Kamalakannan V P, Balasubramanian N, Mater. Res. Innovations, **19**, 258 (2015).

[122] Nag S, Roychowdhury A, Das D, Mukherjee S, Mater. Res. Bull., **74**, 109 (2016).

[123] Narayana P A, Mehra A, Venkateswarlu P, Can. J. Phys., **46**, 1705 (1968).

[124] Nguyen M T, Seriani N, Piccinin S, Gebauer R, J. Chem. Phys., **140**, 064703 (2014)

[125] Nikolic M V, Slankamenac M P, Nikolic N, Sekulic D L, Aleksic O S, Mitric M, Pavlovic V B, Nikolic P M, Scie. Sinter., **44**, 307 (2012).

[126] Nishi N, Kosugi K, Hino K, Yokoyama T, Okunishi E,Chem. Phy. Lett., **369**, 198 (2003).

[127] Nishi N, Kosugi K, Hino K, Yokoyama T, Eur. Phys. J. D, **24**, 97 (2003).

[128] Nuli Y, Zhang P, Guo Z, Munroe P, Liu H, Electrochim. Acta., **53**, 4213 (2008).

[129] Ohn K, Tanaka M, Takeda J, Kawazoe Y, Nano and micro materials, Springer publication,9 (2008).

[130] Ortege D, Magnetic nanoparticle from fabrication to clinical applications, CRC Press Inc, 3 (2012).

[131] Ovshinsky S R, Patent Apr. 30, **5**, 512 (1996).

[132] Ozdemir O, Dunlop D J, Berquo T S, Geochem. Geophys. Geosy., **9**, 10 (2008).

[133] Pavel K, He J, John V T, Maharjan P, Spinu L, Goloverda G Z, Kolesnichenko V L, Langmuir, **29**, 710 (2013).

[134] Pooja D, Kumar A, Sing M, Adv. Mat. Lett., **3**, 330 (2012).

[135] Prakash A, Chandra S, Bahadur D, Carbon, **5**, 04209 (2012).

[136] Pramanick A, Omar S, Nino J C, Jones J L, J. Appl. Cryst.,**42**, 490 (2009).

[137] Pu Z, Cao M, Huang K, Hu C, Nanotechnol., **17**, 799 (2006).

[138] Raman C V, Krishna K S, Nature, **121**, 501 (1928).

[139] Ramirez S, Chan K, Hernandez R, Recinos E, Hernandez E, Salgado R, Khitun A G, Garay J E, Balandin A A, Mater. Design, **118**, 75 (2017).

[140] Rashid N M A, Haw C, Chiu W, Khanis N H, Rohaizad A, Khiew P, Rahman S A, Crys. Eng. Comm., **18,** 4720 (2016).

[141] Rath C, Sahu K K, Kulkarni S D, Anand S, Date S K, Das R P, Mishra N C, Appl. Phys. Lett., **75**, 26 (1999).

[142] Raza M A, Westwood A, Brown A, Hondow N, Stirling C, Carbon, **49**, 4269 (2011).

[143] Rehman S, Yang W, Liu F, Hong Y, Wang T, Hou Y, Inorg. Chem. Front., **2**, 576 (2015).

[144] Roca A G, Marco J F, Morales M D P, Serna C J, J. Phys. Chem. C, **111**, 18577 (2007).

[145] Roy M, Naskar M K, Phy. Chem. Phys., **18**, 20528 (2016).

[146] Ruderman M A, KittelC, Phy. rev., **96**, 1 (1954).

[147] Saji C, Bushiri M J, Vaidyan V K, J. Phys. D, **39**, 4540 (2006).

[148] Sajjadi S H, Goharshadi E K, J. Environ. Chem. Eng., **5**, 1096 (2017).

[149] Salmani M H, Ehrampoush M H, Jahromi M A, Askarishahi M, J. Environ. Health. Sci. Eng., **11**, 11 (2013).

[150] Santos T R T, Andrade M B, Silva M F, Bergamasco R , Hamoudi S, Environmental. Technol., **10**, 1(2017).

[151] Sarkar S K, Raul K K, Pradhan S S, Basu S, Nayak A, Physica E, **64**, 78 (2014).

[152] Sawyer N C, Carty M P L, Parkin G F, Chemistry for environmental engineering, Mc. Graw Hill International Edition, Singapore, (1994).

[153] Schroder D K, Semiconductor material and device characterization, Wiley Interscience, New York, (1998).

[154] Semat H, Katz R, Magnetic properties of matter, Robert Katz Publications, 185(1958).

[155] Sen T K, Mahajan S P, Khilar K C, Colloid. Surface. A, **211**, 91 (2002).

[156] Seraghni N, Belattar S, Mameri Y, Debbache N, Sehili T, Int. J. Photoenergy, **630425**, 1 (2012).

[157] Shang X, Guo Z, Gan W, Zhou R, Ma C, Hu K, Niu H, Xu J, Ionics, **22**, 435 (2016).

[158] Silva M F, Oliveira L A S, Ciciliati A M, Silva L T, Pereira B S, J. Appl. Phy., **114**, 104311 (2013).

[159] Sobon G, Sotor J, Jagiello J, Kozinski R, Zdrojek M, Holdynski M, Paletko P, Boguslawski J, Lipinska L, Abramski K M, Opt. Express., **20**, 19463 (2012**)**.

[160] Song F, Guan J, Fan X, Yan G, J. Alloy. Compd., **485**, 753 (2009).

[161] Su C, Wang H, Liu X, Cryst. Res. Technol., **46**, 209 (2011).

[162] Suber L, Imperatori P, Mari A, Marchegiani G, Mansilla M V, Fiorani D, Plunkett W R, Rinaldi D, Cannas C, Ennas G, Peddis D, Phys. Chem. Chem. Phys.,**12**, 6984 (2010).

[163] Sun Y, Zhang J, Huang T, Liu Z, Yu A, Int. J. Electrochem. Sci., **8**, 2918 (2013).

[164] Suzuki M, Kasuga A, US. Patent Feb. 21, 4, 075,384 (1978).

[165] Syed F N, Polshettiwar V, Sci. Rep., **5**, 0973 (2015).

[166] Tadic M, Citakovic N, Panjan M, Satnojevic B, Markovic D, Jovanovic D, Spasojevic V, J. Alloy.Compd., **543**, 118 (2012).

[167] Tadic M, Citakovic N, Panjan M, Stojanovic Z, Markovic D, Spasojevic V, J. Alloy. Compd., **509**, 7639 (2011).

[168] Tercero M D, Roder C, Ferenbacher U, Teipel U, Turk M, J. Nanopart. Res., **16**, 2350 (2014).

[169] Thomas M, Katsumi K, Alexander V N, James P O, Francisco R R, Jean R, Kenneth S W S, Pure. Appl. Chem., **87**, 1051 (2015).

[170] Torrent J, Barron V, Diffuse reflectance spectroscopy, University of Cordoba, Spain, (2008).

[171] Tucek J, Zboril R, Petridis D, J. Nanosci. Nanotechnol., **6,** 926 (2006).

[172] Tuinstra F, Koening J L, J. Chem. Phys., **53**, 1126 (1970).

[173] Uhl F M, Yao Q, Nakajima H, Manias E, CharlesA, Wilkie C A, Polym. Degrade. Stab., **89**, 70 (2005).

[174] Umar A, Ahmad R, Hwang S W, Kim S H, Hajry A A, Hahn Y B , Electrochim. Acta, **135**, 396 (2014).

[175] Vallina B, Rodriguez-Blanco J D, Brown A P, Benning L G, Blanco J A, J. Nanopart. Res., **16**, 1 (2014).

[176] Vandenberghe R E, San E V, Grave E D, Costa G M D, J. Phys.,**51**, 663 (2001).

[177] Varma A, Mukasyan A S, RogachevA S, ManukyanK V, Chem. Rev.,**116**, 14493 (2016).

[178] Vujtek M, Zboril R, Kubinek R, Mashlan M, Science,technology and education of microscopy: an overview, Microscopy Book Series 1, (2003).

[179] Wachswan E D, Wepper W, Traversa E, Liu M, Vanysek P, Yamazoe N,Proceedings of the international symposium ionics devices, **32**, 25 (2000).

[180] Wakabayashi K, Pierre C, Dikin D A, Rouff R S, Ramanathan T, Brinson L C, Torkelson J M, Macromolecules, **41**, 1905 (2008).

[181] Walker P L, Cariaso O, Patel R L, Fuel, **47**, 322 (1968).

[182] Wang L, Gao L, Cryst. Eng. Comm., **13**, 2011 (1998).

[183] Wang L, Gao L, J. Am. Ceram. Soc., **91**, 85 (2008).

[184] Wang T, Zhou S, Zhang C, Lian J, Liang Y, Yuan W, New. J. Chem., **38**, 4 (2014).

[185] Wang X, Zhang L, Ni Y, Hong J, Cao X, J. Phys. Chem. C, **113**, 7003 (2009).

[186] Watt M, The principles and practice of electron microscopy, Cambridge University Press, Cambridge, 2nd Edition, (1997).

[187] Wegmann M, Scharr M, Precision Medicine Tools and Quantitative Approaches, Academic Press, 145 (2018).

[188] Weiser H B, Milligan W O, Bates J B, J. Phys. Chem. **46**, 99 (1942).

[189] Weldemariam Y, Tadesse A, Chem. Mater. Res., **7**, 35 (2015).

[190] Wilde R E, Ghosh S N, Marshall B J, Inorg. Chem.**9**, 2512 (1970).

[191] Willard H H, Instrumental methods of analysis, Belmont, 7th edition (1987).

[192] Wu C, Yin P, Zhu X, Yang C O, Xie Y, J. Phys. Chem. B, **110**, 17806 (2006).

[193] Wu W, Wu Z, Yu T, Jiang C, Kim W S, Sci. Technol. Adv. Mater., **16**, 023501 (2015).

[194] Xu C, Yuan L, Liang G, Gu A, J. Mater. Chem. C**, 4**, 3175 **(**2016).

[195] Xu C, Yang S, Zhang G, Sun Y, Gao D, Mater. Lett., **65**, 911 (2011).

[196] Yakimchuk E, Soots R, Kotin I, Antonova I, Curr. Appl. Phys. **17**, 1655 (2017).

[197] Yan S, Zan G, Wu Q, Nano Res., **8**, 3673 (2015).

[198] Yang P, wang D, Zhao J, Bhi F, Mater. Res. Bull., **65**, 36 (2015).

[199] Yang S, Song X, Zhang P, Sun J, Gou L, Small, **10,** 2270 (2014).

[200] Ye J, An Y, Elizabeth M, Campbell P U, Worsley M A, Tran I C, Liu Y, Wood C B, Biener J, Jiang H, Tang M, Wang Y M, J. Mater. Chem. A, **4**, 4032 (2016).

[201] Yu J S, Chaudhari N K, Kim C S, Park J, U S Patent 8,865,116 (2014).

[202] Yuan R, Fu X, Wang X, Liu P, Wu L, Xu Y, Wang X, Wang Z, Chem. Mater.,**18**, 4700 (2006).

[203] Zboril R, Mashlan M, Petridis D, Chem. Mater., **14**, 969 (2002).

[204] Zhang B T, Li H F, Zheng X, Teng Y, Liu Y, Lin J M , J. Chromatogr. A, **1370**, 9 (2014**)**.

[205] Zhang L, Yu X, Hu H, Li Y, Wi M, Wang Z, Li G, Sun Z, Chen C, Sci. Rep.,**5**, 9298 (2015).

[206] Zhang Q, Lu X, Chen L, Shi Y, Xu T, Liu M,Mater. Lett., **106**, 447 (2013).

[207] Zhong L S, Hu J S, Liang H P, Cao A M, Song W G, Wan L J, Adv. Mater., **18**, 2426 (2006).

[208] Zhu L P, Xiao H M, Liu X M, Fu S Y, J. Mater. Chem., **16**, 1794 (2006).

[209] Zhu W, Cui X, Liu X, Zhang L, Huang J Q, Piao X, Zhang Q, Nanoscale Res., Lett., **8**, 1 (2013).